DESIGN OF SYNCHRONOUS RELUCTANCE MACHINES WITH A WIDE SPEED RANGE

A THESIS SUBMITTED TO
THE GRADUATE SCHOOL OF NATURAL AND APPLIED SCIENCES
OF
MIDDLE EAST TECHNICAL UNIVERSITY

BY

YUSUF BASRİ YILMAZ

IN PARTIAL FULFILLMENT OF THE REQUIREMENTS
FOR
THE DEGREE OF MASTER OF SCIENCE
IN
ELECTRICAL AND ELECTRONICS ENGINEERING

SEPTEMBER 2021

Approval of the thesis:

DESIGN OF SYNCHRONOUS RELUCTANCE MACHINES WITH A WIDE SPEED RANGE

submitted by **YUSUF BASRİ YILMAZ** in partial fulfillment of the requirements for the degree of **Master of Science in Electrical and Electronics Engineering Department, Middle East Technical University** by,

Prof. Dr. Halil Kalıpçılar
Dean, Graduate School of **Natural and Applied Sciences** _____

Prof. Dr. İlkay Ulusoy
Head of Department, **Electrical and Electronics Engineering** _____

Assist. Prof. Dr. Emine Bostancı Özkan
Supervisor, **Electrical and Electronics Engineering** _____

Examining Committee Members:

Assoc. Prof. Dr. Ozan Keysan
Electrical and Electronics Engineering, METU _____

Assist. Prof. Dr. Emine Bostancı Özkan
Electrical and Electronics Engineering, METU _____

Prof. Dr. Muammer Ermiş
Electrical and Electronics Engineering, METU _____

Prof. Dr. Hulusi Bülent Ertan
Mechatronics Engineering, Atılım University _____

Assist. Prof. Dr. Taner Göktaş
Electrical and Electronics Engineering, Dokuz Eylül University _____

Date: 10.09.2021

I hereby declare that all information in this document has been obtained and presented in accordance with academic rules and ethical conduct. I also declare that, as required by these rules and conduct, I have fully cited and referenced all material and results that are not original to this work.

Name, Surname: Yusuf Basri Yılmaz

Signature :

ABSTRACT

DESIGN OF SYNCHRONOUS RELUCTANCE MACHINES WITH A WIDE SPEED RANGE

Yılmaz, Yusuf Basri
M.S., Department of Electrical and Electronics Engineering
Supervisor: Assist. Prof. Dr. Emine Bostancı Özkan

September 2021, 127 pages

Synchronous reluctance machines (SynRMs) are a good alternative for traction and industrial applications due to their good power density, low cost and high efficiency. However, they suffer from high torque ripple, low power factor and poor high speed performance due to their singly excited nature. To overcome these challenges, rotor geometries are optimized to get a low torque ripple and ferrite magnets are inserted in the flux barriers to get a higher power factor and a better high speed performance.

This thesis aims to propose a methodology to design synchronous reluctance machine with a wide speed range with high power output by using parametric sweep and optimization methods. It is observed that rotor design has an effect on the high-speed performance of SynRMs. However, even the maximum power of the optimized machine decreases sharply as the field weakening region of the machine is extended. Moreover, when the high speed performance of a SynRM is concerned, mechanical and electromagnetic designs must be performed concurrently. To assure a mechanically robust rotor structure, radial ribs must be added to the flux barriers but these connections cause a decrease in the electromagnetic performance of the machine. So,

the high speed performance of the machine decreases further as the ribs in the flux barriers must get thicker as the maximum speed is increased. Based on these findings, it is concluded that PM assistance is required to reach an acceptable high speed performance. Therefore, the amount of required PM material to reach a satisfactory output power at the maximum speed is determined for selected SynRM designs. These analysis is performed with both ferrite and NdFeB type permanent magnet materials, and ferrite assisted SynRM design is found to be favorable due to its much lower cost. Finally, the design and analysis methods are validated with the measurements taken from a small-scaled prototype SynRM that is designed in this study.

Keywords: Synchronous Reluctance Machines, High-speed Performance, Torque Ripple, Flux Barrier Design, PM Assistance, Parametric Sweep, Optimization

ÖZ

GENİŞ HIZ BÖLGESİ OLAN SENKRON RELÜKTANS MAKİNALARIN TASARLANMASI

Yılmaz, Yusuf Basri
Yüksek Lisans, Elektrik ve Elektronik Mühendisliği Bölümü
Tez Yöneticisi: Dr. Öğr. Üyesi. Emine Bostancı Özkan

Eylül 2021 , 127 sayfa

Senkron relüktans makineleri (SenRM'ler), iyi güç yoğunluğu, düşük maliyeti ve yüksek verimliliği nedeniyle çekiş ve endüstriyel uygulamalar için iyi bir alternatiftir. Ancak, tek ikazlı yapıları nedeniyle yüksek tork dalgalanması, düşük güç faktörü ve düşük yüksek hız performansından muzdariptir. Bu zorlukların üstesinden gelmek için rotor geometrileri, düşük tork dalgalanması elde etmek için optimize edilmiştir ve daha yüksek güç faktörü ve daha iyi yüksek hız performansı elde etmek için akı bariyerlerine ferrit mıknatıslar yerleştirilmiştir.

Bu tez, parametrik tarama ve optimizasyon yöntemini kullanarak geniş hız aralığına ve yüksek güç çıkışına sahip SenRM tasarlamak için bir metodoloji önermeyi amaçlamaktadır. Rotor tasarımının SenRM'lerin yüksek hız performansı üzerinde etkisi olduğu gözlemlenmiştir. Ancak optimize edilmiş makinenin maksimum gücü bile makinenin alan zayıflatma bölgesi genişledikçe keskin bir şekilde düşer. Ayrıca, bir SenRM'nin yüksek hız performansı söz konusu olduğunda, mekanik ve elektromanyetik tasarımların aynı anda gerçekleştirilmesi gerekir. Mekanik olarak sağlam bir rotor yapısı sağlamak için akı bariyerlerine radyal nervürler eklenmelidir ancak bu

bağlantılar makinenin elektromanyetik performansında düşüşe neden olur. Bu nedenle, maksimum hız arttıkça akı bariyerlerindeki nervürlerin kalınlaşması gerektiğinden makinenin yüksek hız performansı daha da düşer. Bu bulgulara dayanarak, kabul edilebilir bir yüksek hız performansına ulaşmak için PM yardımının gerekli olduğu sonucuna varılmıştır. Bu nedenle, seçilen SenRM tasarımları için maksimum hızda tatmin edici bir çıkış gücüne ulaşmak için gereken mıknatıs miktarı belirlenir. Bu analizler hem ferrit hem NdFeB tipi sabit mıknatıslı malzemelerle yapılmakta olup, ferrit destekli SynRM tasarımının maliyetinin çok daha düşük olması nedeniyle uygun olduğu görülmüştür. Son olarak, bu çalışmada tasarlanan küçük ölçekli bir SenRM prototipinden alınan ölçümlerle analiz yöntemleri doğrulanmıştır.

Anahtar Kelimeler: Senkron Relüktans Makinalar, Yüksek-hız Performansı, Moment Salınımı, Akı Bariyeri Tasarımı, SM-desteği, Parametrik Tarama, Optimizasyon

To my lovely family...

ACKNOWLEDGMENTS

Firstly, I would like to express my sincere gratitude to Assist. Prof. Dr. Emine Bostancı Özkan for her continuous motivation, significant guidance, and strong encouragement. This thesis would be impossible without her guidance and support.

I would also like to express my gratitude to dear committee members: Assoc. Prof. Dr. Ozan Keysan , Prof. Dr. Muammer Ermiş, Prof. Dr. Hulusi Bülent Ertan and Assist. Prof. Dr. Taner Göktaş for their kind contribution to this thesis.

I am thankful to TÜBITAK, the Scientific and Technological Research Council of Turkey, for granting me their M.S. studies scholarship.

I wish to show my gratitude to my colleagues in PowerLab Research Group and METU: Furkan Karakaya, Furkan Tokgöz, Göksenin Hande Bayazıt, Gökhan Çakal, Eren Özkara, Enes Ayaz, Hakan Polat, Ogün Altun, Serhat Emir Ogan, Barış Kuseyri, Mohammad Hossein Mokhtare, Hakan Saraç, Nail Tosun, Mehmet Çetinkaya, Şirin Yazar, İlkay Ataol, Görkem Gülletutan, and Özgür Yazıcı for their kind supports.

I am also grateful to AEMOT, for their valuable contributions in prototyping and testing of the designed motor.

Finally and most importantly, I would like to thank my mom, my dad, my brother and my bigger family for their endless supports during my whole life.

TABLE OF CONTENTS

LIST OF TABLES

TABLES

LIST OF FIGURES

FIGURES

LIST OF ABBREVIATIONS

CPU	Central processing unit
DC	Direct current
DTC	Direct torque control
EV	Electrical vehicle
FEA	Finite element analysis
FW	Field weakening
GA	Genetic algorithm
IM	Induction machine
MMF	Magneto motive force
MTPA	Maximum torque per ampere
MTPv	Maximum torque per voltage
NdFeB	Neodymium iron boron
PM	Permanent magnet
PMaSynRM	Permanent magnet assisted synchronous reluctance machine
PMSM	Permanent magnet synchronous machine
PWM	Pulse width modulation
SPWM	Sinusoidal pulse width modulation
SVPWM	Space vector pulse width modulation
SynRM	Synchronous reluctance machine

LIST OF VARIABLES

n_r	Number of rotor slots
n_s	Number of stator slots
β	Arranging angle
$n\alpha_m$	Rotor slot pitch angle
L_{dq}	Cross saturation inductance
L_d	d-axis inductance
L_q	q-axis inductance
w_e	Electrical rotational speed
I_d	d-axis current
I_q	q-axis current
V_s	Phase voltage
V_d	d-axis voltage
V_q	q-axis voltage
V_PM	Voltage due to PM
p	pole pair number
T_{em}	Electromagnetic torque average
R_s	Phase resistance
V_{dc}	Dc-link voltage
ϕ	Magnetic flux
B	Magnetic flux density
A	Area
k	Number of flux barriers
S_n	Thickness of n^{th} iron bridge

W_{n1}	Thickness of n^{th} flux barrier through q-axis
W_{n2}	Thickness of n^{th} flux barrier through d-axis
k_{wq}	Air to iron ratio in q-axis
k_{wd}	Air to iron ratio in d-axis
k_i	Iron distribution constant
k_b	Air distribution constant
α	Bending angle of flux barriers
h_r	Thickness of rotor back iron
R_r	Rotor radius
g	Air gap length
R_{shaft}	Shaft radius
F_c	Centrifugal force
ω	Rotational speed
m	Mass
w_n	Thickness of n^{th} rib
$R_{s,in}$	Inner stator radius
P	Power
τ_s	Slot pitch
h_s	Slot height
h_{s0}	Slot opening height
w_s	Slot width
w_{s0}	Slot opening width
Q	Total slot number
n	Phase number
q	Slot number per pole per phase
k_s	Slot width to slot pitch ratio
A_{slot}	Slot area

J_{rms}	Current density in rms
k_f	Fill factor
ϕ_{bi}	Flux in stator back iron
B_{bi}	Maximum flux density in stator back iron
h_{bi}	Stator back iron thickness
$B_{air,r}$	Flux density in air gap at radius r
ϕ_{air}	Flux density in air gap at radius r
λ_α	Flux linkage in α-axis
λ_β	Flux linkage in β-axis
λ_A	Phase A flux linkage
λ_B	Phase B flux linkage
λ_C	Phase C flux linkage
λ_d	Flux linkage in d-axis
λ_q	Flux linkage in q-axis
I_s	Phase current in peak
θ	Rotor position
α_i^e	Current angle
C_{q1}	q-axis flux linkage constant 1
C_{q2}	q-axis flux linkage constant 2
C_d	d-axis flux linkage constant
C_t	Torque constant
$l_z^{'}$	Resized axial length
$\lambda_d^{'}$	Recalculated d-axis flux linkage
$\lambda_q^{'}$	Recalculated q-axis flux linkage
T_{max}	Maximum average torque
P_{12000}	Output power at 12000 rpm
T_{12000}	Average torque at 12000 rpm

n_{base}	Base speed
T_ν	ν^{th} torque harmonic
$\hat{K_\nu}$	Electrical loading
$k_{w\nu}$	Winding factor of ν^{th} harmonic
D	Inner stator diameter
μ_0	Relative permeability

CHAPTER 1

INTRODUCTION

1.1 Introduction

The use of low efficiency electric drives in the industry and fossil fuels in the traction applications contributes to carbon and greenhouse gases emission. In order to decrease this effect, minimum efficiency standarts for all purpose electric drives that are used in the industry are being updated and electrification of the transport is encouraged by new regulations and insentives.

Induction machines (IMs) are the most commonly used electric machine types in industrial drive systems. However, synchronous reluctance machine (SynRM) drives are being considered as a good alternative for inductance machine (IM) drives in variable speed drive applications. It has been shown that SynRMs can reach an efficiency standard as an IM in a smaller frame size. Losses of SynRMs concentrate in the stator, and there are only iron losses in their rotor. That is an important advantage that simplifies the cooling system. Moreover, SynRMs can be cost optimized alternatives to the commonly used interior permanent magnet synchronous machines (IPMSMs) in the traction applications. However, field weakening speed ranges of SynRMs are limited, and they have a lower power factor compared to IMs and PMSMs. Therefore, PM-assisted SynRMs is proposed to solve these shortcomings for applications with a wide speed range requirement and a limited space such as electric vehicle drives [1]. To sum up, use of SynRMs with or without PMS is expected to increase in the industrial applications and in the transportation.

1.2 Motivation and Problem Definition Based on Literature Review

SynRM is not a new concept, and it is first developed in 1923 by Kostko [2]. However, this machine was not seen as a good alternative to an IM due to its relatively low-efficiency at that time [3]. Kotsko thought that this machine would not be a commonly used machine due to its unexpected behavior. The reason for this idea was the fact that this machine type was difficult to start and control until the microprocessor-controlled power converters were introduced in the 1970's [4]. Moreover, development in power electronic devices and finite element analysis tools ease the design of SynRMs and also their control.

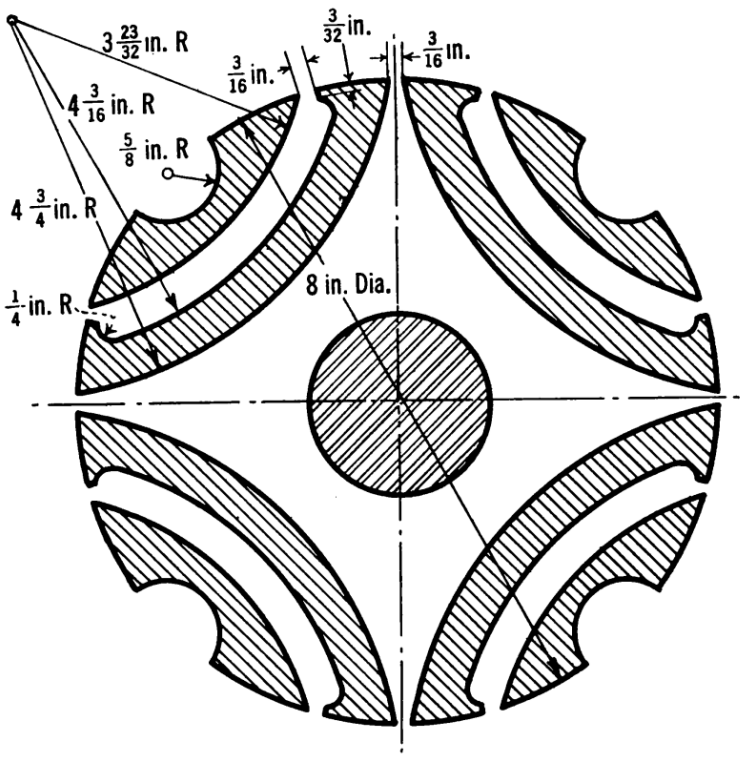

Figure 1.1: First designed SynRM [2]

Nowadays, synchronous machines with high energy density permanent magnets (PM) dominate the electric machine market for application requiring high power density and efficiency. However, due to the increase in the rare earth magnet prices as shown in Fig. 1.2, researchers are in search for alternatives with less PM or without PM. As

another option, machines with low cost ferrite PMs are studied.

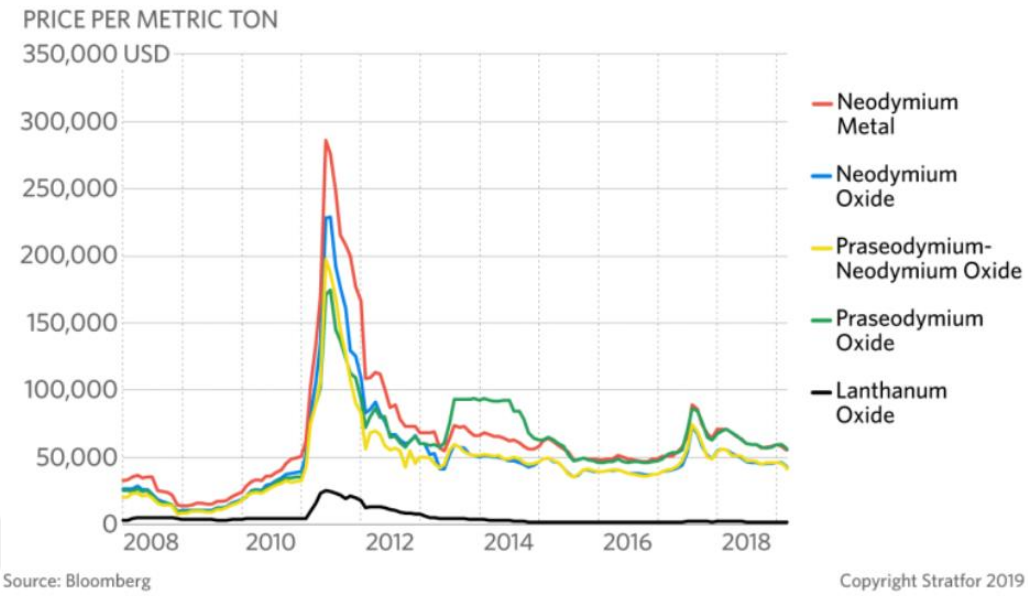

Figure 1.2: Rare-earth magnet materials price over years [5]

Furthermore, synchronous reluctance machines have many other advantages.

- Their torque per ampere is higher than IMs and it does not depend on rotor temperature unlike PMSM. [6]
- Their efficiency is higher than IM due to the lack of rotor losses.
- They are magnet free.
- Their price is low due to the lack of rotor winding, cage or magnets [6].
- They are fault tolerant due to lower braking torque under various winding fault scenarios [7, 8].
- It is easy to manufacture SynRM when it includes a stator identical to that of the induction machine [9].
- Their control strategy is similar to IPMSM but it requires exact position measurement [10].

- Available inverters can be used in the SynRM drive systems.

Beside these advantages, synchronous reluctance machine has some disadvantages on which researchers work. These disadvantages are as follows:

- They have higher fluctuation in output torquecompared to IMs and PMSMs [6].
- They have a lower power factor compared to IMs and PMSMs [11].
- Their high speed performance is poor due to their singly excited nature [11].

Researchers have developed some methods in order to decrease the torque ripple of SynRMs [7, 12–25]. Some researchers focus on rotor design in order to decrease torque ripple [7, 12–17, 21–25]. Moreover, some researchers try to decrease torque ripple by using control methodologies [18–20].
Vagati [12] proposes that there should be n_r equally distanced points around the rotor periphery where, n_r is the total number of rotor slots, and it is determined by the total number of flux barriers. This implies a constant rotor slot pitch. Thus, some high-order harmonics disappear. In some cases, virtual flux barriers are added to the machine to increase n_r. When relevant calculations are performed, Vagati figured out that there is a relationship between rotor slot number n_r and stator slot number n_s. This relationship is given in (1.1). This methodology strictly depends on this relationship, and it decreases the number of options for stator slot number.

$$n_r = n_s \pm 4 \tag{1.1}$$

Moghaddam [13] wants to get rid of the relationship given in (1.1). He defined a new angle β, which is given in Fig. 1.3, and keeps the rest of the rotor slot pitches defined by α_m constant. Thus, the relationship which is given in (1.1) is not necessary in order to get a lower torque ripple. Moreover, there is not a rule between flux barrier number and stator slot number. Torque ripple can be minimized for any flux barrier and stator slot number pair by adjusting β angle.

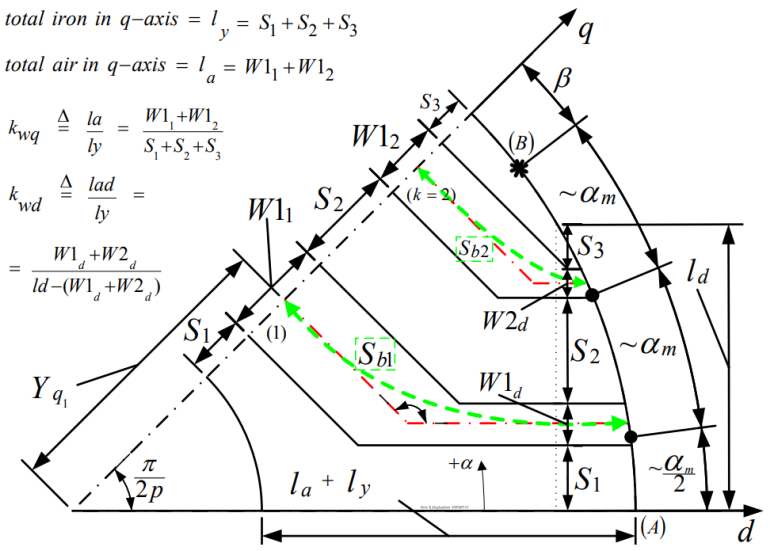

Figure 1.3: Rotor parameters defined in [13]

Rouhani et al. [7] proposes another method in order to decrease torque ripple. It is identified that positions of stator and rotor slots cause a cross-coupling inductance, which is represented as L_{dq}. This inductance causes torque ripple. Proper design of stator and rotor decreases the effect of L_{dq} and torque ripple is decreased as well. Bianchi et al. [14, 22, 23] use torque harmonic calculations so that the average and peak-to-peak value of torque can be calculated. Torque harmonics are calculated by using electrical loading, magnetic stator potential, and rotor magnetic potential. Moreover, they perform simplified calculations by assuming that iron ribs are removed, magnetic saturation in the rotor and stator are ignored, and stator effect is ignored. Maharaj et al. [15] uses Bianchi's equations and tries to optimize them. They optimize positions of flux barriers with respect to slot positions. Chan et al. [16] focus on relative positions of flux barriers with respect to each other. They create a variable with respect to flux barrier positions, outer flux barrier position, and stator slot pitch. By optimizing this parameter, he tries to minimize torque ripple.

In [17], authors make sensitivity analysis in order to determine how much torque ripple is affected by different parameters. The parameters that they examine are the stator inner diameter, slot opening height, slot opening width, air gap, each flux barrier position, rib thickness, and total air in the q-axis. They observe that all variables

affect the torque ripple of the machine, but some of them have a major effect on torque ripple, while others have a minor effect.

In [21], authors calculate the air gap magnetic field. Determining the reluctance in the system by using conformal mapping. Then, he calculates the magnetic field in the air gap is calculated by using the equivalent magnetic circuit approach. AS a result, average torque and torque ripple values are obtained. Yamomoto et al. [24] propose to use asymmetric flux barriers in order to decrease torque ripple by using flux barriers that are not symmetric with respect to the q-axis of the machine. Thus, the number of rotor parameters is doubled. This causes an increase in the computation time of the design process.

In [18], Hamidreze et al. try to decrease torque ripple when direct torque control (DTC) is applied. Huynch et al. [19] also try to decrease torque ripple by eliminating errors in stator flux calculations. As more accurate calculations are done, and torque ripple can be decreased. Li et al. [20] use bi-axes high-frequency signals injection in order to decrease torque ripple. In brief, these three methodologies focus on the control of the machine in order to lessen the fluctuation in output torque of the machine.

There are many studies that focus on SynRM optimization [26–36]. Most of them try to maximize average torque and minimize torque ripple of the machine [27–34, 36]. . Moreover, only few of them focus on the high speed performance of the machine.

The performance of SynRMs at high speed is poor that is the power of the machine decreases with increasing speed after base speed. Researchers study on the performance improvement of high speed synchronous reluctance machines [26, 37–43]. They generally focus on mechanical structure of the machine in the high speed region [37–43]. Pellegrino et al. [26] focus on high-speed performance of the machine by maximizing the average torque of the machine and by minimizing the d-axis flux when the current angle is 90. Thus, the optimized machine has good high-speed performance.

SynRMs are a good alternative for low speed and high torque applications or high speed and low torque applications. The reason for this is that SynRMs are not convenient for high-speed applications without ribs, and ribs decrease the machine performance. Moreover, their inductance values are relatively higher, and they reach flux limit rapidly when speed increases. These both cause poor high-speed performance. Our motivation is to design a SynRM with good high-speed performance. Moreover, many studies have been published on SynRM design, but the high-speed performance

of the machine was studied only in a couple of these studies. So, the high-speed performance of the SynRM is studied in this thesis.

1.3 Outline of Thesis

The outline of the thesis is as follows:

In Chapter 2, structure and operation of SynRMs are presented and analytical expressions for their torque and voltage calculations are given.

Rotor design and parameterization are performed in Chapter 3. Firstly, flux barrier shape is chosen among different flux barrier topologies. Then, the number of flux barriers is determined by observing the torque ripple with the selected stator slot numbers. Then, rotor parameters are defined. Finally, the determination of position and distribution of rotor flux barriers are illustrated. As a post-process work, horizontal and radial ribs are defined and categorized.

In Chapter 4, a 100 kW SynRM with a 12000 rpm maximum speed is designed. Firstly, the rotor radius is determined by observing the required width of the radial ribs that are required to assure the mechanical robustness of the rotor at the maximum speed. Then, stator core and winding designs are performed. By using rotor parameters defined in Chapter 3, candidate designs are created. These designs are evaluated based on their torque ripples and high speed performances with a proposed analysis methodology systematically. Finally, designs are illustrated to form a Pareto front and candidate designs are selected.

In Chapter 5, permanent magnet assisted versions of the selected SynRMs in Chapter 4 are designed. NdFeB and ferrite magnets are used for machines, and their performance and costs are compared.

In Chapter 6, the design process which is presented in Chapter 4 repeated by using a multi-objective optimization. Firstly, sensitivity analysis is performed for rotor parameters. Then, the machine is optimized by using a multi-objective genetic algorithm in which the Objectives are defined as the torque ripple and the maximum power at maximum speed. Then, these results are also used to obtain a the Pareto

front, and a design is selected. Finally, this design is compared with the designs from Chapter 4 to evaluate the performances of both design methods.

Validation of the design methodoly and analysis results are done in Chapter 7. First, design and manufacturing of a small-scaled 10 kW SynRM is presented. Then, the test process is explained, and test results are given. Finally, experimental results are compared with the simulation results.

Finally, the findings and outcomes of the study are summarized and suggested future works are listed in Chapter 8.

CHAPTER 2

CONCEPT OF SYNCHRONOUS RELUCTANCE MACHINES

The synchronous reluctance machines (SyRMs) are the multi phase motors which have reluctance and inductance difference in their rotors and have rotating field. Reluctance difference is obtained by flux barriers in the rotor. These flux barriers are air cavities and decrease magnetic conductivity. In a SynRM, there are high and low reluctance axis as many as pole pair number. High reluctance means low magnetic conductivity and lower inductance. Low reluctance axis is d-axis and high reluctance axis is q- axis as can be seen in Fig. 2.1 [44].

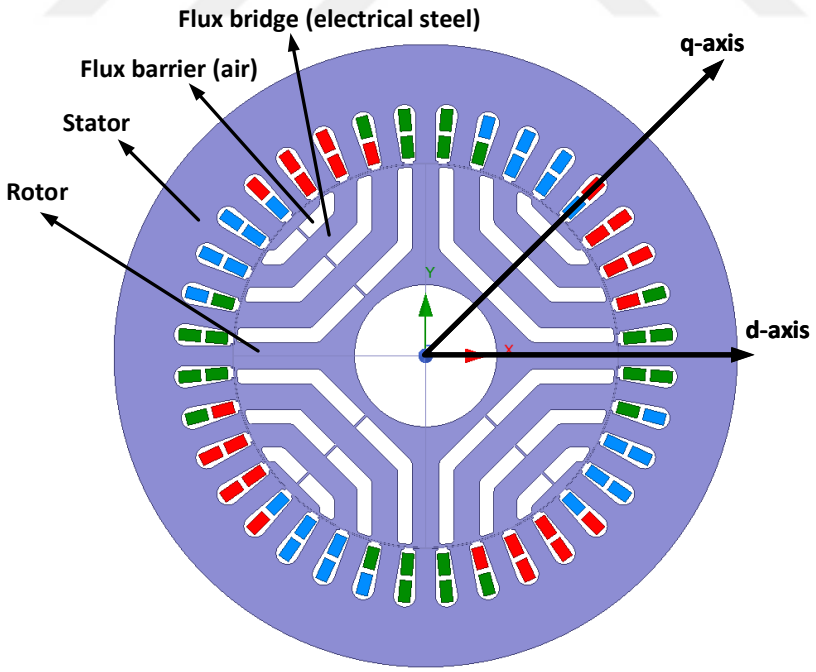

Figure 2.1: Four pole synchronous reluctance machine

When the stator is electrified, a rotating magnetic field is obtained. The rotor of the machine tries to align itself to low reluctance axis, thus electromagnetic torque is created. If the rotor is aligned to one of the lowest or the highest reluctance, machine can not generate torque.
Stator of a SynRM is same as of a conventional induction machine (IM). Thus, conventional IMs can be replaced with SynRMs by replacing only rotor.

2.1 Rotor Geometries

There are three kinds of rotor greometries. The first one is a simple salient pole rotor as can be seen in Fig. 2.2. In the second type of rotor which is axially laminated anisotropic (ALA), the laminations are shaped individually and insulated from each other. Finally, they are connected to each other through pole holders to the central region. In the final rotor type which transversally laminated anisotropic (TLA), laminations are punched with traditional techniques [45].

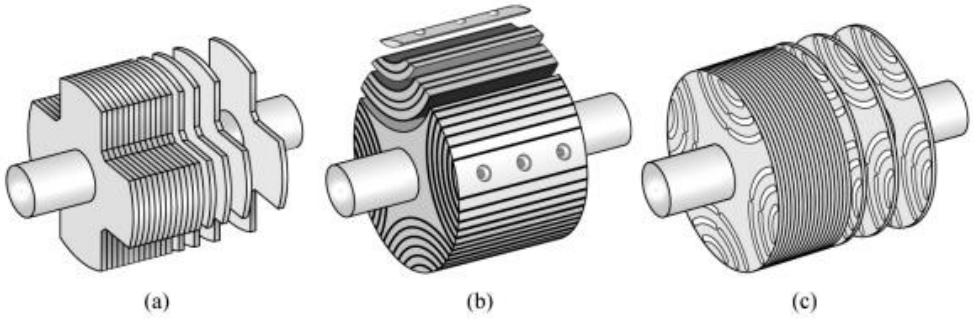

Figure 2.2: Rotor realization techniques a. simple salient pole (SP) rotor, b. axially laminated anisotropic (ALA) rotor and c. transversally laminated anisotropic (TLA) rotor [45]

2.2 PM Assisted Synchronous Reluctance Machine (PMaSynRM)

SynRMs have low power factor and poor high-speed performance as mentioned before. In order to increase power factor and correct high-speed performance, PMs are added to the rotor of the machine. These PMs are inserted into the flux barrier in the rotor as can be seen in Fig. 2.3. Moreover, these PMs can be inserted to the sides of the flux barriers if needed. Furthermore, flux barrier shapes should be proper for PM insertion. In Fig. 2.3, flux barrier has rectangular shape and it is proper to insert PM. Magnetization direction of the PMs are shown in Fig. 2.3 and it is -q direction. This contributes to increase power factor of the machine. Moreover, it decreases q-axis flux linkage and increases the reluctance difference between d and q-axis. Thus, machine performance increases.

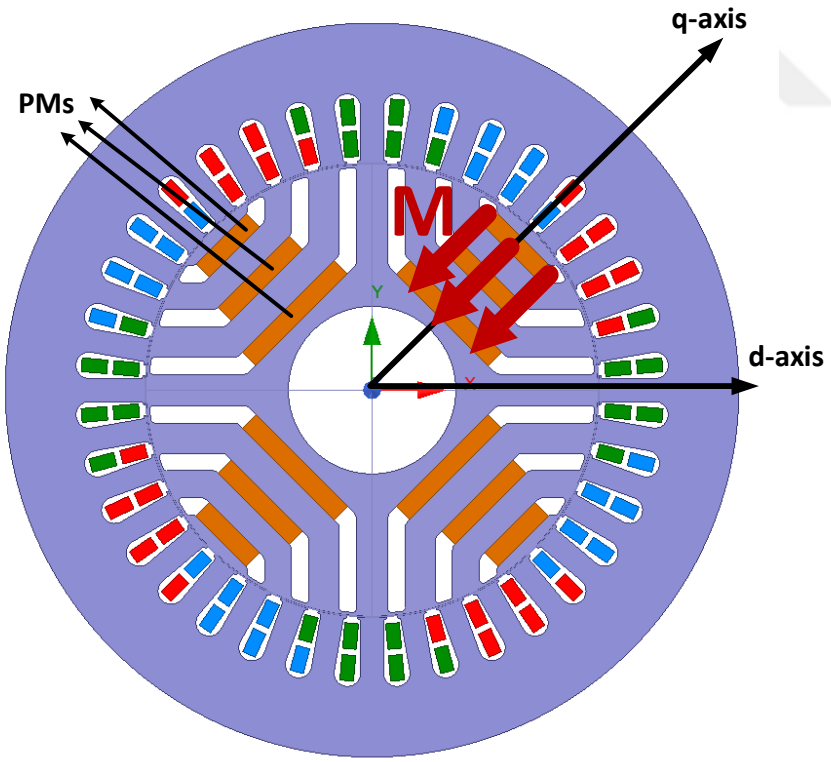

Figure 2.3: Four pole PM assisted synchronous reluctance machine (PMaSynRM)

2.3 Field Results for SynRM and PMaSynRM

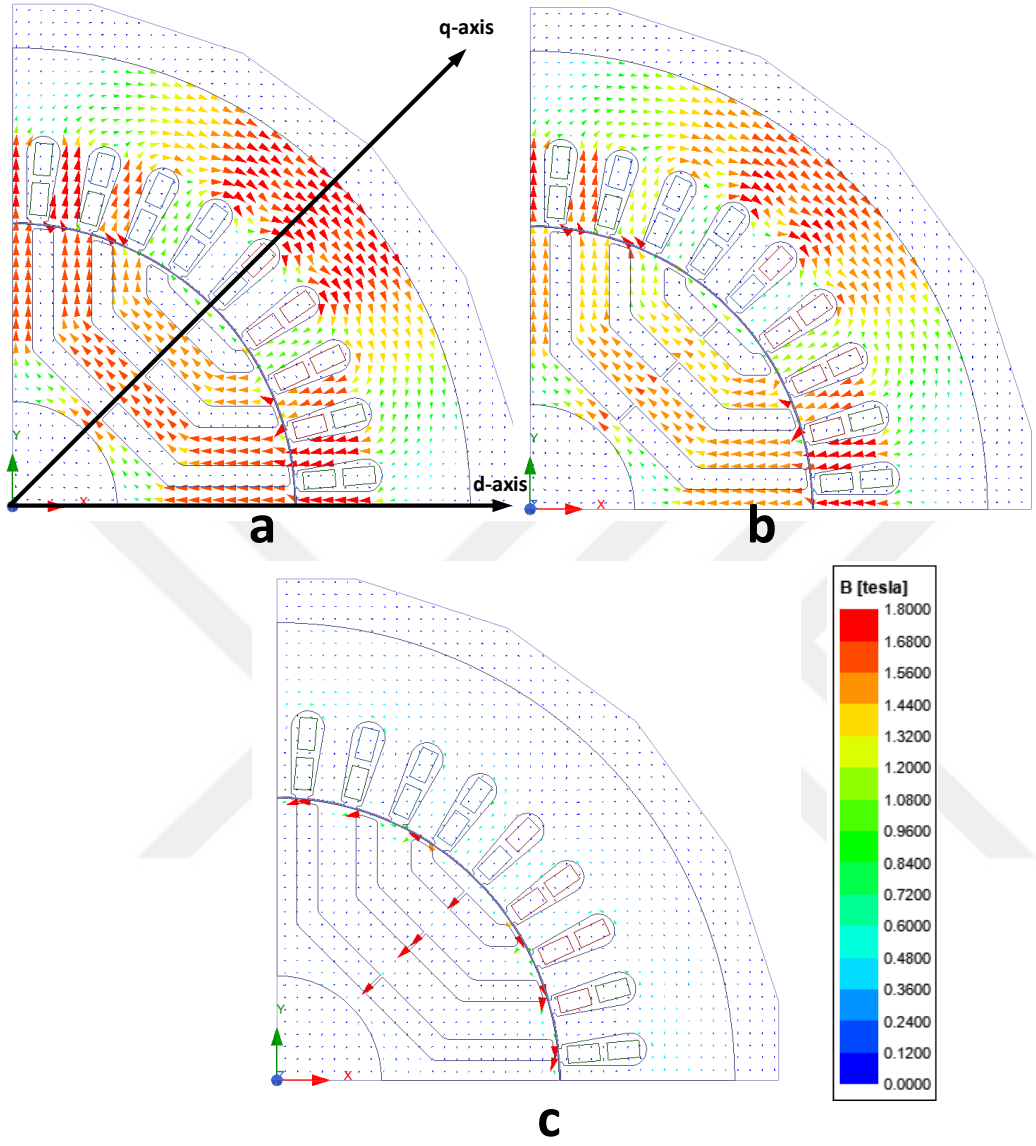

Figure 2.4: Flux lines of SynRM a. for current angle=0 degree, b. for current angle=45 degrees and c. for current angle=90 degrees

In Fig. 2.4 and 2.5, flux density distributions of SynRM and PMaSynRM for different current angles are given. As can be seen in Fig. 2.4, stator flux flows through iron bridges when the current angle is zero and resultant torque is equal to zero in this case since flux flows in the path whose reluctance is minimum. Zero current angle means alignment of d-axis flux. Moreover, when the current angle is 90 degrees, flux flows

perpendicular to flux barriers and reluctance is maximum. As well, resultant torque is zero in this case. When the current angle is 45 degrees, reluctance is neither maximum nor minimum. Thus, the machine tries to align itself to minimum reluctance and it generates torque.

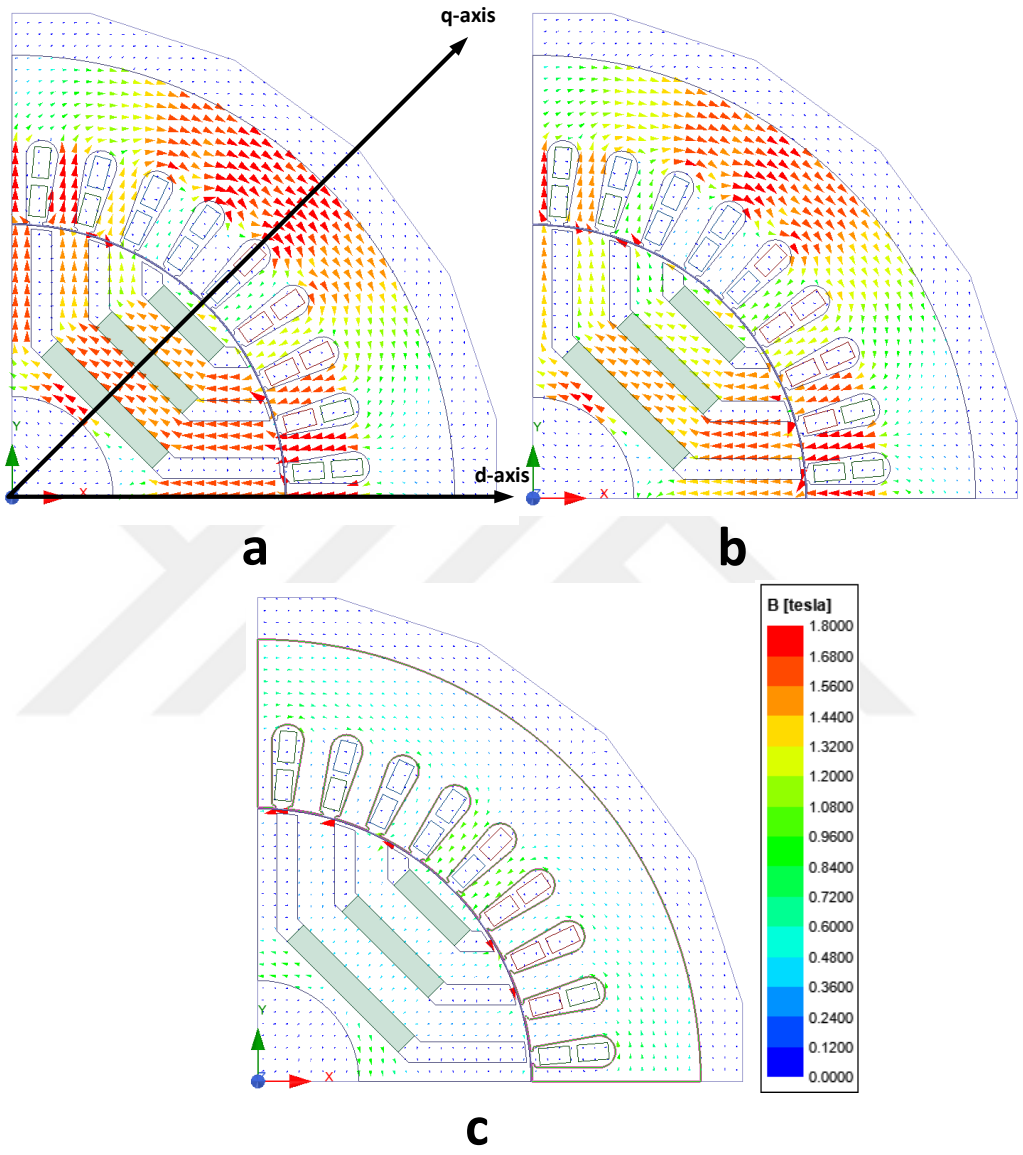

Figure 2.5: Flux lines of PMaSynRM a. for current angle=0 degree, b. for current angle=45 degrees and c. for current angle=90 degrees

In Fig. 2.5, flux lines for PMaSynRM are given. As can be seen, flux which is perpendicular to flux barriers decreases since PM is added in order to decrease this

flux. Thus, machine performance can be increased.

2.4 Vector Diagram of SynRM and PMaSynRM

dq-axes of SynRM is presented in Fig. 2.4. As can be seen, the reluctance of the d-axis is smaller than the q-axis reluctance. It concludes with higher d-axis inductance L_d than q-axis inductance L_q. Moreover, this reluctance difference causes reluctance torque. Moreover, vector diagram is given in Fig. 2.6 for SynRM and in Fig. 2.7 for PMaSynRM. According to Fig. 2.6, voltage equations can be obtained by ignoring the stator resistance. As can be seen in Fig. 2.7, PM should generate a voltage in d-axis in order to decrease the angle between phase current and voltage. Thus, the magnet is added to q-axis and magnetization direction is chosen as -q-direction.

$$V_d = -\omega_e L_q I_q \tag{2.1}$$

$$V_q = \omega_e L_d I_d \tag{2.2}$$

$$V_s = jV_d + V_q \tag{2.3}$$

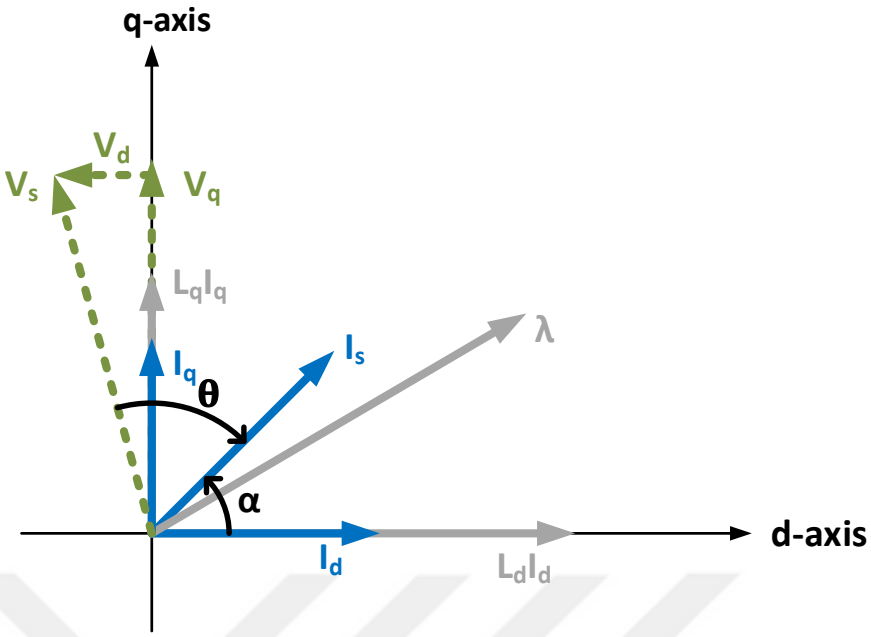

-

Figure 2.6: Vector diagram of SynRM

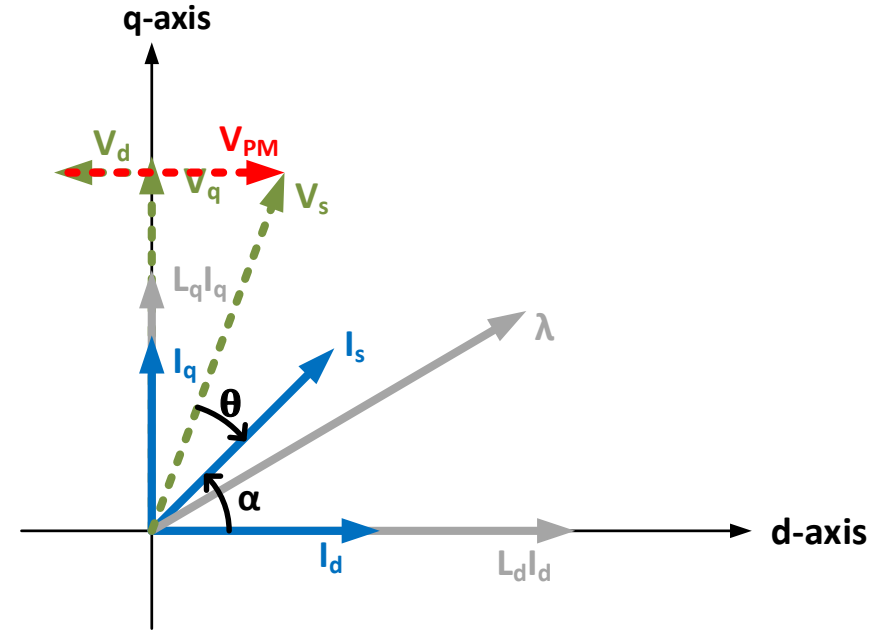

-

Figure 2.7: Vector diagram of PMaSynRM

2.5 Operating Characteristics of SynRMs

Torque equation of a SynRM is given in (2.5), where p is the pole pair number. Accordingly, d-axis current i_d and q-axis current i_q should be equal to get maximum torque per ampere so current angle wrt. d-axis (α) is 45 deg for the unsaturated operation. Once the magnetic core material starts to saturate, d- and q-axis inductances (L_d and L_q) get affected by saturation differently. As can be seen in the Fig. 2.8, d-axis flux linkage λ_d is much larger than q-axis flux linkage λ_q and λ_q gets affected from saturation relatively less. So, L_d is more prone to saturation due to a very low magnetic reluctance on the d-axis flux path compared to q-axis. This means that the machine saliency ratio $\zeta = L_d/L_q$ decreases due to saturation. Therefore, i_d is decreased to keep the L_d close to its unsaturated value and i_q is increased to be able to obtain a higher torque. This leads to an increase in the current angle. Therefore, a higher current angle than 45 deg is applied depending on the saturation level of the core materials even in the base-speed region. This is done to make sure the machine generates maximum torque per ampere. Fig. 2.9 shows the effect of the saturation on the torque characteristics. As stator phase current i_s increases, maximum torque per ampere angle shifts away from 45 deg.

$$\lambda_d = L_d i_d \text{ and } \lambda_q = L_q i_q \tag{2.4}$$

$$T_{em} = \frac{3}{2} p(\lambda_d i_q - \lambda_q i_d) = \frac{3}{2} p(L_d - L_q) i_d i_q \tag{2.5}$$

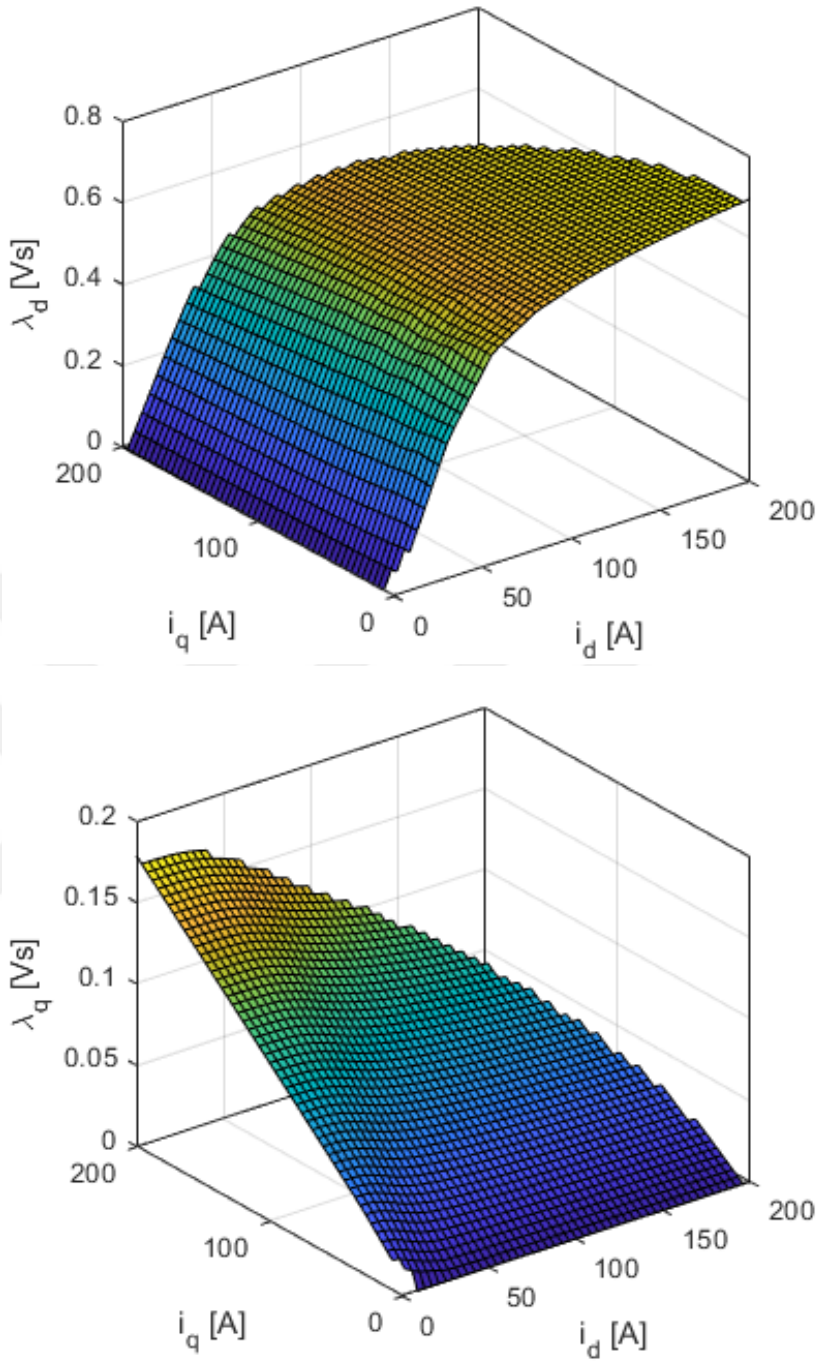

Figure 2.8: Exemplary λ_d and λ_q characteristics as a function of i_d and i_q.

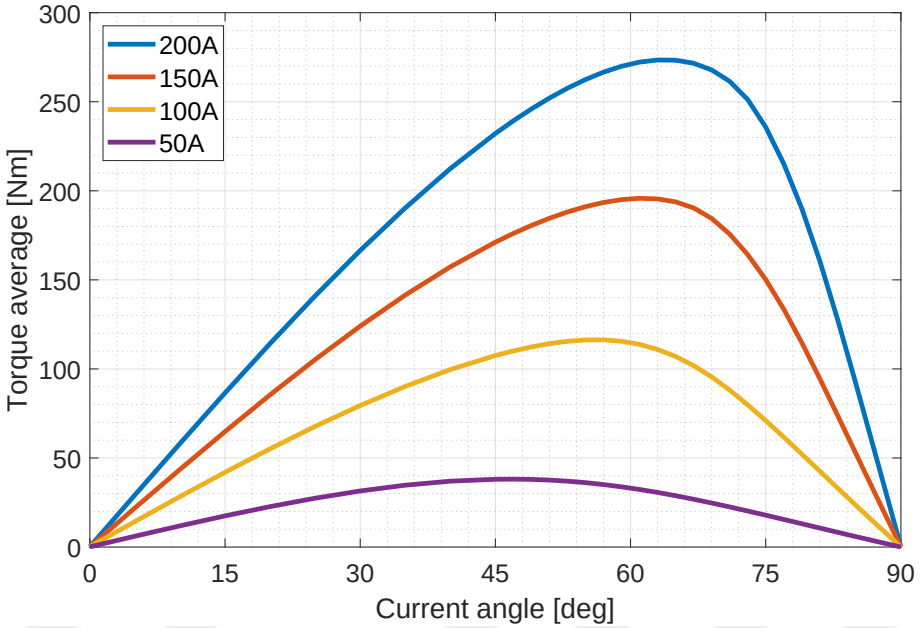

Figure 2.9: Exemplary torque characteristics at various stator currents.

As rotational speed increases, the stator voltage limit that is related to the DC-link voltage and the used modulation technique is reached. In (2.6), voltage limit is given for space vector pulse width modulation, where V_{dc} is the DC-link voltage and ω_e is the electrical frequency. Since $L_d > L_q$, stator terminal voltage v_s can be reduced more rapidly as d-axis current reduces. So, reducing d-axis current is beneficial also in high-speed operation to restrict the phase voltage as it was applied in magnetic saturation to increase torque-per-ampere.

$$v_s = \sqrt{(\omega_e L_d i_d + R_s i_q)^2 + (\omega_e L_q i_q + R_s i_d)^2} \leq \frac{V_{dc}}{\sqrt{3}} \tag{2.6}$$

SynRMs are known to have a limited field weakening range since the current angle that gives the highest torque-per-ampere and the current angle that must be applied to stay within the voltage limit are close to each other only for a short extended speed range. As can be seen in Fig. 2.10, there is a sharp decrease in the torque vs. current angle characteristics around 4500 rpm and the output power cannot be kept constant at higher speeds.

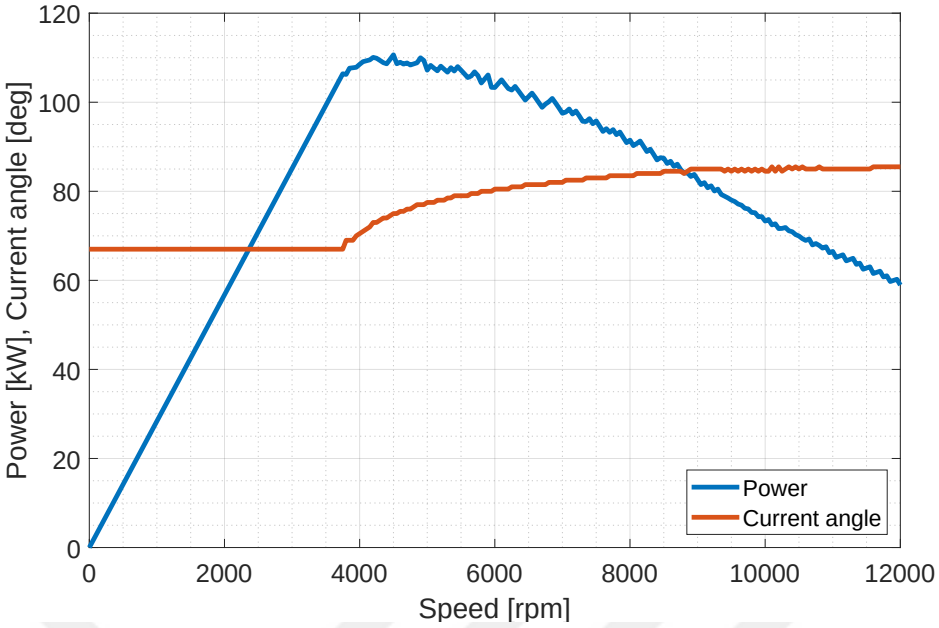

Figure 2.10: Exemplary power and current angle characteristics.

The power factor of a SynRM depends on the saliency ratio ζ and operating conditions. For an operation with a current angle, α equal to 45 deg, a power factor lower than $cos(\pi/4) \approx 0.7$ can be reached with a high saliency ratio. The vector diagram representing this case is shown in Fig. 2.6, where it is clear that d-axis voltage v_d must be ideally zero to get the mentioned power factor value. However, in the case of magnetic saturation and operation at stator voltage limit, the power factor can get values around 0.8 and slightly higher as α >45 deg. The change of the current angle over speed when the machine operates within stator voltage limits can be seen in Fig. 2.10, where it changes between approximately between $60 - 80$ deg.

In Fig. 2.11, torque, power, power factor and efficiency for PMaSynRM and SynRM are given. These characteristics are categorized under maximum torque per Ampere (MTPA), FW region 1 (constant current, constant voltage) and, FW region 2 (decreasing current, constant voltage). As can be seen, there is only FW 1 region for PMaSynRM in the considered speed range and it does not reach the FW region 2 [46]. Moreover, PMaSynRM has better torque, power at maximum speed, power factor, and efficiency than SynRM.

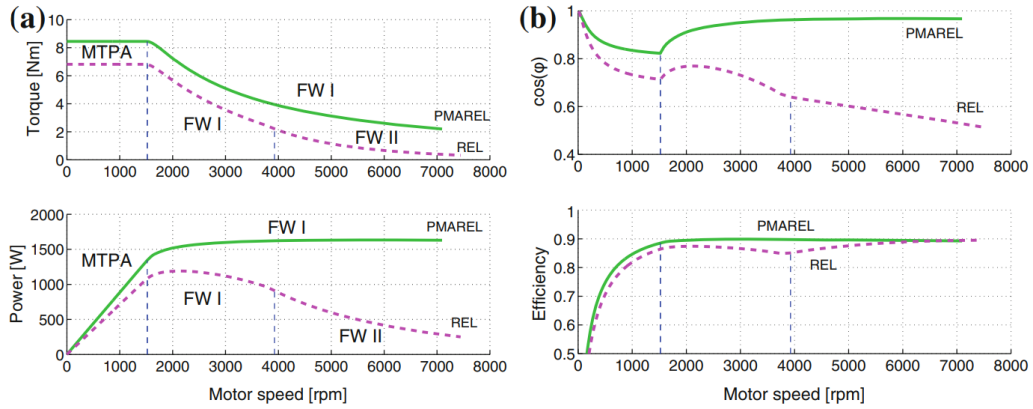

Figure 2.11: Torque, power, power factor and efficiency for PMAREL and REL configurations [46]

In this thesis, the motivation is to increase FW1 region as much as possible without PM and designing only the rotor of the machine. Thus, it can be seen whether this machine can reach up to high speed without PM or not. If this can not be accomplished, PM amount can be decreased by designing the SynRM to get a wide FW1 region.

CHAPTER 3

ROTOR PARAMETERIZATION AND DESIGN FOR SYNRM

The rotor design of SynRM includes both electromagnetic and mechanical design aspects. The electromagnetic design dictates the machine performance such as average torque, torque ripple, and high-speed performance. However, electromagnetic design is restricted by mechanical concerns so that the rotor keep its integrity at high speeds. Therefore, electromagnetic and mechanical design aspects should be considered concurrently.

3.1 Rotor Geometry and Parameterization

As the name also implies, SynRM generates only reluctance torque. To achieve this torque, there should be a reluctance difference between the d and q-axes. Reluctance difference is achieved thanks to the flux barriers. Flux barriers are the air cavities that are introduced through d and q axis as can be seen in Fig. 3.1. There are different kinds of flux barrier shapes. In this study, a rectangular or also called U-shaped flux barrier shape is chosen to ease the parameterization and placement of PMs in PM assisted type SynRMs. Moreover, there are alternative flux barrier shapes such as Zhukovski barrier and C-type barrier [47–51].

This study aims to create a rotor model with reduced number of parameters. Therefore, some assumptions are made. A representative rotor model of a 4-pole 3 flux barriers design is shown in Fig. 3.1. As can be seen in this drawing, the thickness of an the magnetic material between two sequential air barriers is constant through the d and q-axes while thicknesses of flux barriers vary. This property provides a homogenous saturation level along with each iron mass. Almost all magnetic flux

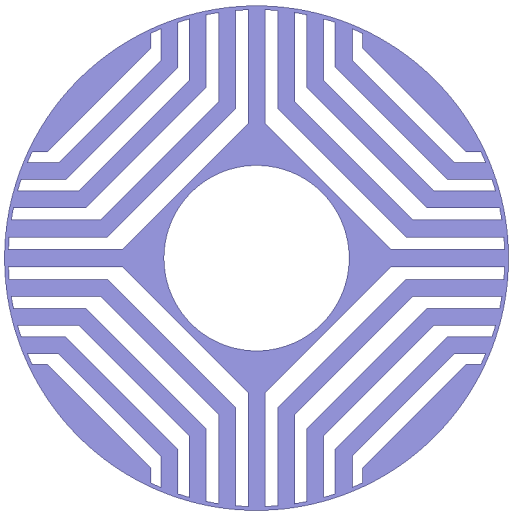

Figure 3.1: Rotor for 4 pole machine with 4 flux barriers

flows through electrical steel, and magnetic material should be kept constant through the flux path. Then, it is observed that flux density on each iron is constant by using (3.1).

$$\phi = BA \tag{3.1}$$

Rotor design includes geometry aspects and parameters. To achieve good rotor geometry, parameters should be chosen and defined well. It makes it easier to create a rotor and gives a chance to control each parameter individually. Thus, the effect of each parameter on the machine performance can be observed. Moreover, rotor geometry optimization can be performed by optimizing these variables. Defining rotor geometry with the fewer variables enables optimization with less computation time as well. In light of this information, rotor parameterization is critical to make the design easier and to fasten the analysis. Rotor parameters can be categorized under two subtopics: flux barrier position parameters and flux barrier distribution parameters.

Flux barrier positions affect the torque ripple, so they should be determined carefully. The parameter for the position is the tangential angle between each flux barrier and all flux barriers should fit in a pole pitch. Some designers determine each flux barriers

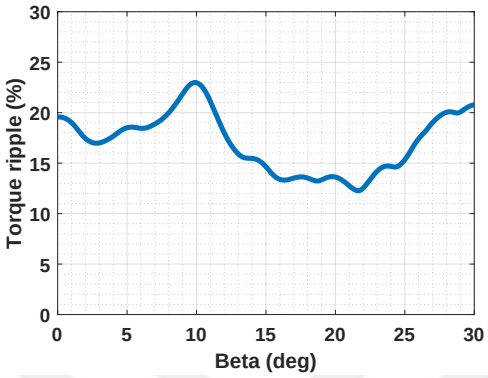

(a) Analytical calculation results for 36 slots, 4 poles and 3 barriers

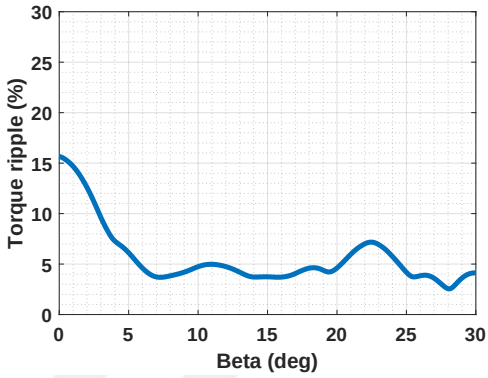

(b) Analytical calculation results for 36 slots, 4 poles and 4 barriers

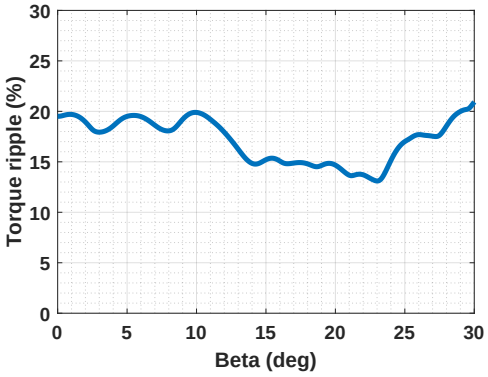

(c) Analytical calculation results for 48 slots, 4 poles and 3 barriers

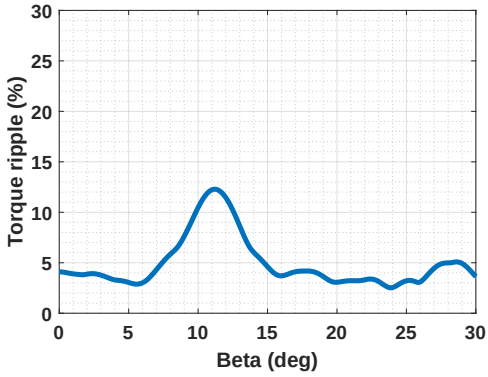

(d) Analytical calculation results for 48 slots, 4 poles and 4 barriers

Figure 3.2: Effects of slot number and flux barriers number on torque ripple

angle individually. This causes that there is an angle parameter as many as flux barriers. However, Vagati [12] proposes a constant rotor slot pitch which concludes that each flux barrier is placed with equal angle intervals which are equal to α_m. However, there should be a relationship between the rotor slot number and stator slot number which is $n_r = n_s \pm 4$ so that torque ripple can be decreased. However, this situation restricts the options to choose flux barrier number and stator slot number. Moghaddam [13] proposes to use another angle β that will be added to the outer most flux barrier to get rid of the dependency of rotor flux barrier number on stator slot number. This method can be applied to any pair of stator slot numbers and flux barrier numbers. As can be seen in Fig. 3.2, torque ripple can be minimized for any flux barrier and stator slot number pair by changing β. Torque ripple is minimized for a machine with 36 slots, 4 poles, and 4 barriers by choosing β value between 5 and 10 degrees. For each combination, there is an interval for the β to minimize torque ripple. By observing these results, the interval of β value to minimize torque ripple can be chosen. This choice can be performed by considering fabrication and resulting flux barriers length. In the case of PM assisted SynRM design, flux barrier lengths should be taken into consideration since it affects the possible amount of PMs. The relationship between α_m and β is given in (3.2) where p is pole number and k is the total number of flux barriers. If β is set to 0, we can ontain Vagati's model and β is illustrated in Fig. 3.3.

$$\alpha_m = \frac{\frac{\pi}{p} - \beta}{k + 0.5} \tag{3.2}$$

On the other hand, flux barrier distribution parameters affect the average torque and high-speed performance of the machine. These parameters determine the amount of air in d and q-axis and its distribution to each flux barrier and iron bridge. As dmentioned before, iron between two sequential air barriers are constant in d and q-axis, and they are represented as S_n for n^{th} barrier. Thus, the total amount of iron in the d and q-axis is the same. However, the thickness of flux barriers is different in the d and q-axis, and they are represented as W_{n1} and W_{n2} for n^{th} barrier where 1 represents q-axis and 2 represents d-axis, respectively. The relationship between W_{n1}

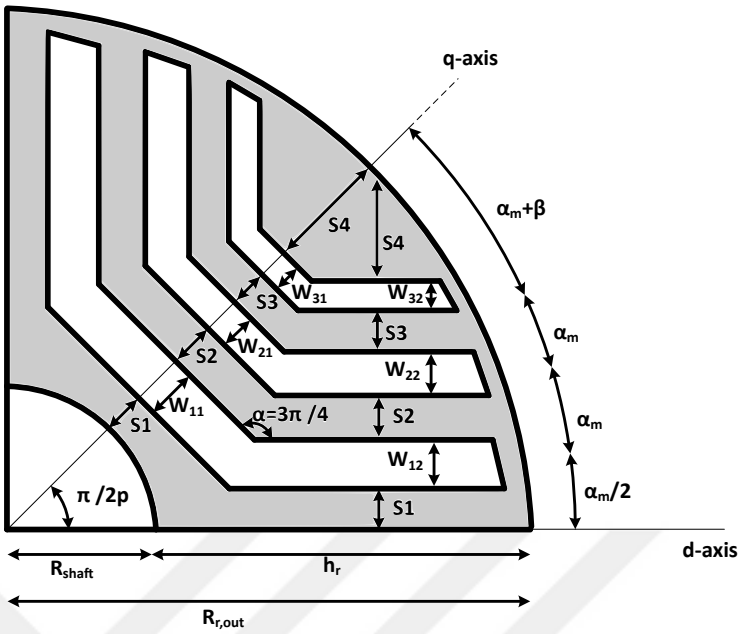

Figure 3.3: Parameters for 4-pole rotor with 3 barriers

and W_{n2} is given in (3.3).

$$\frac{W_{n1}}{W_{n2}} = \frac{W_{k1}}{W_{k2}} \tag{3.3}$$

For each axis, there are different parameters in order to determine the total amount of air. It is defined k_{wq} for q axis and it is given in (3.4) while it is defined as k_{wd} for d axis as given in (3.5).

$$k_{wq} = \frac{\sum_{n=1}^{k} W_{n1}}{\sum_{n=1}^{k} S_n} = \frac{W_{11} + W_{21} + W_{31}.. + W_{k1}}{S_1 + S_2 + S_3..S_k} \tag{3.4}$$

$$k_{wd} = \frac{\sum_{n=1}^{k} W_{n2}}{\sum_{n=1}^{k} S_n} = \frac{W_{12} + W_{22} + W_{32}.. + W_{k2}}{S_1 + S_2 + S_3.. + S_k} \tag{3.5}$$

By combining (3.3), (3.4) and (3.5), the relationship between k_{wq} , k_{wd}, W_{n1} and W_{n2}

is obtained as in (3.6).

$$\frac{W_{n1}}{W_{n2}} = \frac{k_{wq}}{k_{wd}} \tag{3.6}$$

Knowledge of k_{wq} and k_{wd} with an inner and outer radius of the rotor which are represented as R_{shaft} and R_r, respectively, just gives the total amount of iron and air in d and q-axis. However, thicknesses of each flux barrier and iron bridge can not be still found. Thus, there is still a need for extra parameters in order to determine thicknesses. Thus, k_i and k_b are defined, where k_i is the distribution factor for iron bridges and k_b is the distribution factor for flux barriers. Iron distribution is performed for iron bridges when n and k are not equal to 1 in (3.7). When inner iron, which is represented as S_1, is compared to other iron thicknesses, there is a difference. Inner iron is halved since it is doubled on d-axis. The relationship is given in (3.8).

$$\frac{S_n}{S_k} = k_i^{n-k} \tag{3.7}$$

$$\frac{S_n}{S_1} = 2k_i^{n-1} \tag{3.8}$$

In the same manner, flux barrier distribution can be performed as in (3.9).

$$\frac{W_{n1}}{W_{k1}} = k_b^{n-k} \tag{3.9}$$

Flux barrier is perpendicular to d-axis and parallel to q-axis. This makes it easier to arrange the constant thickness of iron masses. It concludes with different angle between flux barrier side crossing α values for rotors with different pole numbers. The relationship between α and pole number p is given in (3.10).

$$\alpha = \pi/2 + \pi/p \tag{3.10}$$

α is illustrated in Fig. 3.3 for 4-pole rotor. It decreases with increasing pole number. For example, it is 135 degree for 4 poles while it is 120 degree for 6 poles. How-

ever, higher pole numbers are not suitable for this barrier shape due to mechanical concerns.

The number of flux barriers is commonly chosen as 3, 4 ,or 5. It depends on h_r which is illustrated in Fig. 3.3. When h_r is small, 3 flux barriers should be chosen. If it is chosen higher with small h_r, thicknesses of flux barriers and irons get smaller. This may not be suitable for fabrication and it can cause mechanical problems in high-speed applications. Moreover, number of barriers affects the torque ripple of the machine as shown in Fig. 3.2 which is calculated analytically and will be given in Chapter 4 in detail. In this figure, torque ripple for different combinations of stator slot number and flux barrier numbers is given, a significant change in the torque ripple between the designs with same stator slot number but different flux barrier number. This illustrates that the choice of the number of flux barrier affects torque ripple results. Thus, designers should decide the number of flux barriers at the beginning of the design process by inspecting the mechanical restrictions and the stator slot number.

3.2 Rotor Geometry Creation

In order to create rotor, thicknesses of all iron bridges and flux barriers should be calculated by using parameters such as k_{wq}, k_{wd}, k_i, k_b and β. As mentioned before, the thickness of an iron bridge through the d and q axis is constant. Thus, there is one thickness parameter for each iron bridge and there are total $n + 1$ parameters for iron bridges where n is the number of flux barriers. Moreover, the relationship between W_{n1} and W_{k1} is given in the previous part. If k_{wq} and k_{wd} are known, then there is one parameter for each flux barrier and for example there are a total of 3 parameters for a flux barrier design. This is concluded that there are 7 independent parameters for thickness and they should be calculated. When it is generalized, there are $2n + 1$ parameters for a rotor with n flux barrier. In order to calculate these thickness parameters, there should be $2n + 1$ independent equations.
When k_{wq} is known for a machine, the total amount of iron through the d and q-axis is known. This gives an equation which is shown in (3.11) for a rotor with 3 flux

barriers.

$$S_1 + S_2 + S_3 + S_4 = h_r \frac{1}{1 + k_{wq}} \tag{3.11}$$

The second equation comes with the knowledge of k_{wd}. When it is known, the total amount of air in the d-axis is known and the equation is given in (3.12) for a rotor with 3 flux barriers.

$$W_{12} + W_{22} + W_{32} = h_r \frac{k_{wd}}{1 + k_{wq}} \tag{3.12}$$

Position parameter β comes with 3 equations for a rotor with 3 flux barriers. These equations are given in (3.13), (3.14) and (3.15), respectively. This makes n additional equations for a rotor with n flux barriers when β is known.

$$S_1 + \frac{W_{12}}{2} = (R_r + g) sin(\frac{\alpha_m}{2}) \tag{3.13}$$

$$S_1 + S_2 + W_{12} + \frac{W_{22}}{2} = (R_r + g) sin(\frac{3\alpha_m}{2}) \tag{3.14}$$

$$S_1 + S_2 + S_3 + W_{12} + W_{22} + \frac{W_{32}}{2} = (R_r + g) sin(\frac{5\alpha_m}{2}) \tag{3.15}$$

Up to now, there are $n + 2$ equations by knowing k_{wq}, k_{wd} and β. Other equations vary with a chosen design methodology and equation number for each parameter can be observed in Table 3.1. There are three kinds of methodology: rotor design with respect to k_b, rotor design with respect to k_i, and rotor design by keeping outer iron thickness constant. These methodologies should be examined individually. If they are investigated at the same time, the number of equations exceeds $2n + 1$ which concludes with no solution case.

Table 3.1: Equation numbers for peach parameter

Design parameter	Number of equations
k_{wq}	1
k_{wd}	1
β	n
k_b	$n-1$
k_i	n

3.2.1 Model 1: Flux barrier distribution with respect to flux barrier distribution

In this methodology, barrier distribution is performed by considering k_b. The thicknesses of iron bridges depend on these results. For a machine with 3 flux barriers, there are 2 equations which are given in (3.16) and (3.17).

$$W_{12} - \frac{1}{k_b} W_{22} = 0 \tag{3.16}$$

$$W_{12} - \frac{1}{k_b^2} W_{32} = 0 \tag{3.17}$$

In general, there are (n-1) equations for a machine with n flux barriers. Thus, there are (2n+1) independent equations when k_{wq}, k_{wd}, β and k_b are known. By using (3.11), (3.12), (3.13), (3.14), (3.15), (3.16) and (3.17), the solution for this methodology can be obtained. These equations can be solved by using (3.18).

$$\begin{bmatrix} S_1 \\ S_2 \\ S_3 \\ S_4 \\ W_{12} \\ W_{22} \\ W_{32} \end{bmatrix} = \begin{bmatrix} 1 & 1 & 1 & 1 & 0 & 0 & 0 \\ 0 & 0 & 0 & 0 & 1 & 1 & 1 \\ 1 & 0 & 0 & 0 & 0.5 & 0 & 0 \\ 1 & 1 & 0 & 0 & 1 & 0.5 & 0 \\ 1 & 1 & 1 & 0 & 1 & 1 & 0.5 \\ 0 & 0 & 0 & 0 & 1 & -\frac{1}{k_b} & 0 \\ 0 & 0 & 0 & 0 & 1 & 0 & -\frac{1}{k_b^2} \end{bmatrix}^{-1} \begin{bmatrix} h_r \frac{1}{1+k_{wq}} \\ h_r \frac{k_{wd}}{1+k_{wq}} \\ (R_r+g)sin(\frac{\alpha_m}{2}) \\ (R_r+g)sin(\frac{3\alpha_m}{2}) \\ (R_r+g)sin(\frac{5\alpha_m}{2}) \\ 0 \\ 0 \end{bmatrix} \tag{3.18}$$

If PMs will be implemented to the machine, it is practical to take k_b as 1. Thus, the thickness of each flux barrier is equal to each other. Implemented PMS also have the same thickness. The manufacturer can order PMs with standard sizes for each flux barrier.

3.2.2 Model 2: Iron mass distribution with respect to iron bridge distribution

The second methodology is based on the distribution of iron by using k_i. Thicknesses of flux barriers are determined by resultant iron thicknesses. For a machine with 3 flux barriers, there are 3 independent equations as given in (3.19), (3.20) and (3.21).

$$S_1 - \frac{1}{2k_i} S_2 = 0 \tag{3.19}$$

$$S_1 - \frac{1}{2k_i^2} S_3 = 0 \tag{3.20}$$

$$S_1 - \frac{1}{2k_i^3} S_4 = 0 \tag{3.21}$$

When k_{wq}, k_{wd} and β are known and iron distribution is performed by using k_b, there are $2n + 2$ equations. This value is larger than parameter number which should be calculated. Thus, it is concluded with no solution. However, there are 2 different way in order to overcome this challenge. First one is that k_{wd} is not determined for a design. This value will be resultant parameter which is calculated by using other

values. So, the equation which is given in (3.12) is not used in this methodology and result is obtained by using (3.11), (3.13), (3.14), (3.15), (3.19), (3.20) and (3.21). These equations are solved by using (3.22).

$$\begin{bmatrix} S_1 \\ S_2 \\ S_3 \\ S_4 \\ W_{12} \\ W_{22} \\ W_{32} \end{bmatrix} = \begin{bmatrix} 1 & 1 & 1 & 1 & 0 & 0 & 0 \\ 1 & 0 & 0 & 0 & 0.5 & 0 & 0 \\ 1 & 1 & 0 & 0 & 1 & 0.5 & 0 \\ 1 & 1 & 1 & 0 & 1 & 1 & 0.5 \\ 1 & \frac{-1}{2k_i} & 0 & 0 & 0 & 0 & 0 \\ 1 & 0 & \frac{-1}{2k_i^2} & 0 & 0 & 0 & 0 \\ 1 & 0 & 0 & \frac{-1}{2k_i^3} & 0 & 0 & 0 \end{bmatrix}^{-1} \begin{bmatrix} h_r \frac{1}{1+k_{wq}} \\ (R_r+g)sin(\frac{\alpha_m}{2}) \\ (R_r+g)sin(\frac{3\alpha_m}{2}) \\ (R_r+g)sin(\frac{5\alpha_m}{2}) \\ 0 \\ 0 \\ 0 \end{bmatrix} \tag{3.22}$$

This methodology is not practical since the effect of k_{wd} can not be observed. Moreover, the change of outer iron's thickness does not give any development for a designer as will be shown later. Thus, an another way is to vanish one of equations is to ignore (3.21). Thus, k_{wd} is still parameter and thickness of last iron is a resultant parameter. By using by using (3.11), (3.11), (3.13), (3.14), (3.15), (3.19) and (3.20), design can be performed. The solution is obtained by using (3.23).

$$\begin{bmatrix} S_1 \\ S_2 \\ S_3 \\ S_4 \\ W_{12} \\ W_{22} \\ W_{32} \end{bmatrix} = \begin{bmatrix} 1 & 1 & 1 & 1 & 0 & 0 & 0 \\ 0 & 0 & 0 & 0 & 1 & 1 & 1 \\ 1 & 1 & 0 & 0 & 1 & 0.5 & 0 \\ 1 & 1 & 1 & 0 & 1 & 1 & 0.5 \\ 1 & \frac{-k_i}{2} & 0 & 0 & 0 & 0 & 0 \\ 1 & 0 & \frac{-k_i^2}{2} & 0 & 0 & 0 & 0 \\ 1 & 0 & 0 & \frac{-k_i^3}{2} & 0 & 0 & 0 \end{bmatrix}^{-1} \begin{bmatrix} h_r \frac{1}{1+k_{wq}} \\ h_r \frac{k_{wd}}{1+k_{wq}} \\ (R_r+g)sin(\frac{\alpha_m}{2}) \\ (R_r+g)sin(\frac{3\alpha_m}{2}) \\ (R_r+g)sin(\frac{5\alpha_m}{2}) \\ 0 \\ 0 \end{bmatrix} \tag{3.23}$$

This methodology is more practical than the previous one since the effect of k_{wd} can be observed. Moreover, the thickness of the outer iron makes sense.

3.2.3 Model 3: Fixed outer irons width

The final methodology is that thickness of the outer iron is determined and kept constant for all designs. This thickness is minimized by considering mechanical and electromagnetic restrictions. When it is larger, stator magnetic flux flows through this iron and it does not contribute to generating torque and power. Moreover, it is restricted by mechanical concerns and it can not be very narrow. By considering these, its thickness is chosen by the designer. As can be seen, the number of parameters that should be calculated decreases by 1 while the number of equations is constant. In order to overcome this situation, the shaft radius of the machine is taken as a variable and determined by parameters such as k_{wq}, k_{wd}, and β. Moreover, distribution is performed by using k_b. When this methodology is compared to first one, there are difference on equations (3.11) and (3.12) and these equations are updated as in (3.24) and (3.25).

$$S_1 + S_2 + S_3 + R_{shaft}\frac{1}{1+k_{wq}} = R_r\frac{1}{1+k_{wq}} - S_4 \tag{3.24}$$

$$W_{12} + W_{22} + W_{32} + R_{shaft}\frac{k_{wd}}{1+k_{wq}} = R_r\frac{k_{wd}}{1+k_{wq}} \tag{3.25}$$

By using (3.24), (3.25), (3.13), (3.14), (3.15), (3.16) and (3.17), the solution for this methodology can be obtained. These equations can be solved by using (3.26).

$$\begin{bmatrix} R_{shaft} \\ S_1 \\ S_2 \\ S_3 \\ W_{12} \\ W_{22} \\ W_{32} \end{bmatrix} = \begin{bmatrix} \frac{1}{1+k_{wq}} & 1 & 1 & 1 & 0 & 0 & 0 \\ \frac{k_{wd}}{1+k_{wq}} & 0 & 0 & 0 & 1 & 1 & 1 \\ 1 & 0 & 0 & 0 & 0.5 & 0 & 0 \\ 1 & 1 & 0 & 0 & 1 & 0.5 & 0 \\ 1 & 1 & 1 & 0 & 1 & 1 & 0.5 \\ 0 & 0 & 0 & 0 & 1 & \frac{-1}{k_b} & 0 \\ 0 & 0 & 0 & 0 & 1 & 0 & \frac{-1}{k_b^2} \end{bmatrix}^{-1} \begin{bmatrix} R_r\frac{1}{1+k_{wq}} - S_4 \\ R_r\frac{k_{wd}}{1+k_{wq}} \\ (R_r+g)sin(\frac{\alpha_m}{2}) \\ (R_r+g)sin(\frac{3\alpha_m}{2}) \\ (R_r+g)sin(\frac{5\alpha_m}{2}) \\ 0 \\ 0 \end{bmatrix} \tag{3.26}$$

This is a more practical methodology since minimizing the thickness of outer iron increases machine performance. Its effects will be considered in further chapters. A

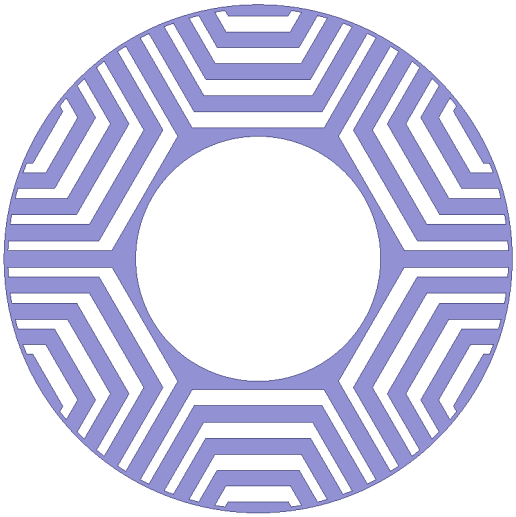

Figure 3.4: Rotor for 6 pole machine with 4 flux barriers

representative 6 pole machine with 4 flux barriers are given in Fig. 3.4.

3.3 Rib Design

Ribs are constructed in order to provide mechanical strength to the rotor. There are two kinds of ribs: tangential and radial ribs. Tangential ribs are placed at the endpoints of flux barriers as can be seen in Fig. 3.5.
Radial ribs are placed in flux barriers. There are two kinds of radial ribs according to their positions in flux barriers. The first one is placed at the center of flux barriers as can be seen in Fig. 3.5. It is commonly used for radial ribs since it is easy to design. When it is designed, all ribs have the same dimensions. However, when PM is placed into flux barriers, it should be moved to the cross point of d and q-axis as illustrated in Fig. 3.6.

Stress analysis is performed by using the simulation toolbox of SOLIDWORKS. During the analysis, the yield strength of the material is critical. Yield strength corresponds to the yield point at which material begins to deform and the maximum stress of the rotor should not exceed this point. When it exceeds the yield strength of the material, this is not a well-designed machine due to mechanical concerns. Stress which occurs on the rotor is proportional to the traditional centrifugal force which is given in

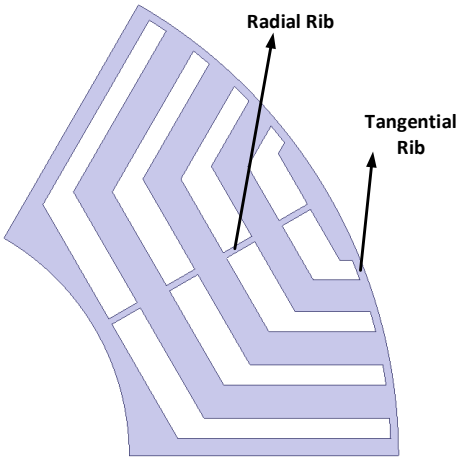

Figure 3.5: Ribs at the middle point of flux barrier

(3.27). Radial magnetic pull is usually much lower than the centrifugal force. Thus, the radius of the rotor should be taken into consideration when ribs are designed.

$$F_c = m\omega^2 r \tag{3.27}$$

The stress on the ribs is not equal since the stress on the inner ribs are higher due to the mass which they carry. Stress results for a machine with 4 poles can be seen in Fig. 3.7.

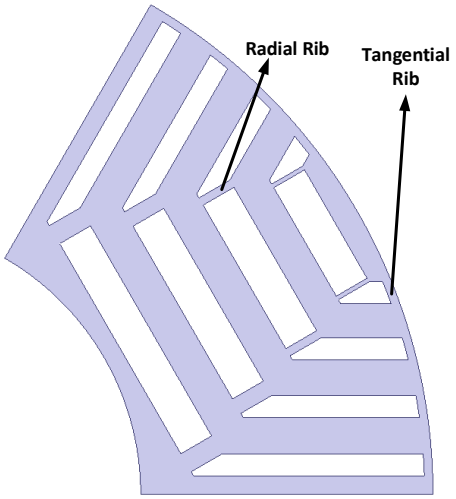

Figure 3.6: Ribs at the cross point of d and q-axis of flux barriers

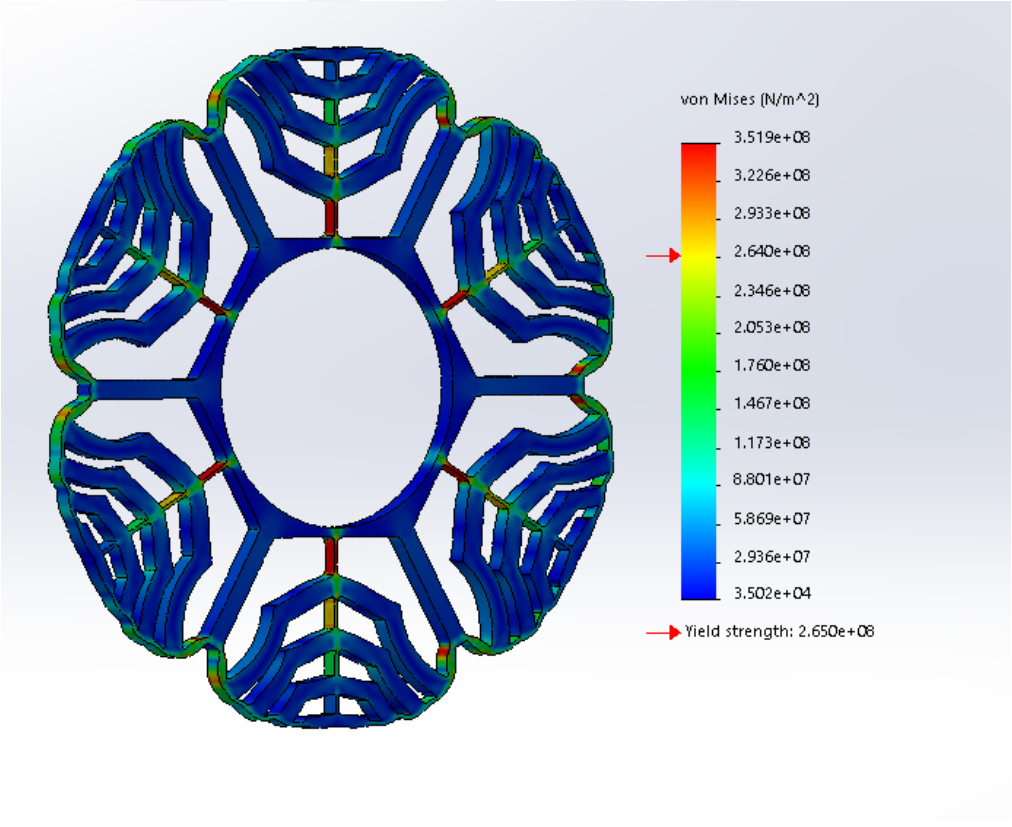

Figure 3.7: Mechanical simulation results for 6 pole machine

As can be seen in Fig. 3.7, the most stress occurs on the radial inner ribs. From inner ribs to outer ribs, stress decreases. Moreover, this is not a mechanically well-designed machine since maximum stress is larger than the yield strength of the material.
Mechanical design is performed iteratively. Firstly, a poor design is analyzed and its results are collected. Then, the rotor's parts, which carry more stress than yield strength, are modified and analysis is repeated. If it is necessary, the radius of the rotor may be updated. Finally, a mechanically well-designed machine can be obtained.

CHAPTER 4

DESIGN OF A 100 KW MACHINE WITH PARAMETRIC SWEEP

4.1 Introduction

In this chapter, a $100\ kW$ machine design process is detailed. Design specifications are given in Table 4.1. The machine's power rating is chosen as $100\ kW$, and the maximum speed is fixed to $12000\ rpm$ and resultant maximum frequency is $600\ Hz$ and it is achievable according to [52]. Moreover, the maximum torque output of the machine is fixed to $250\ Nm$, and it is performed by arranging machine axial length.

Table 4.1: Design specifications

Parameters	Values
Power rating (kW)	100
Maximum speed (rpm)	12000
Maximum torque (Nm)	250
Pole number	6
Maximum frequency (Hz)	600
Flux barrier number	4
Stacking factor	0.95

Pole pair selection is made by considering the machine size and manufacturing. When the pole pair is smaller, the thickness of the back-iron is larger, and the total size of the machine increases. When the pole pair increases, the total size of the machine decreases. However, manufacturing becomes more difficult. Thus, the pole pair is

chosen as 3, and the pole number is 6. Moreover, flux barrier number selection is performed by considering both mechanical and electromagnetic concerns. Choosing flux barrier number high makes manufacturing harder since thicknesses of flux barriers and iron bridges are smaller. Moreover, iron bridges saturate easily. Thus, flux barrier numbers should not be selected higher. Possible candidates for flux barrier number is 3 and 4. On the other hand, selecting this number higher increases machine performance. Thus, it is selected as 4.

4.2 Design Flowchart

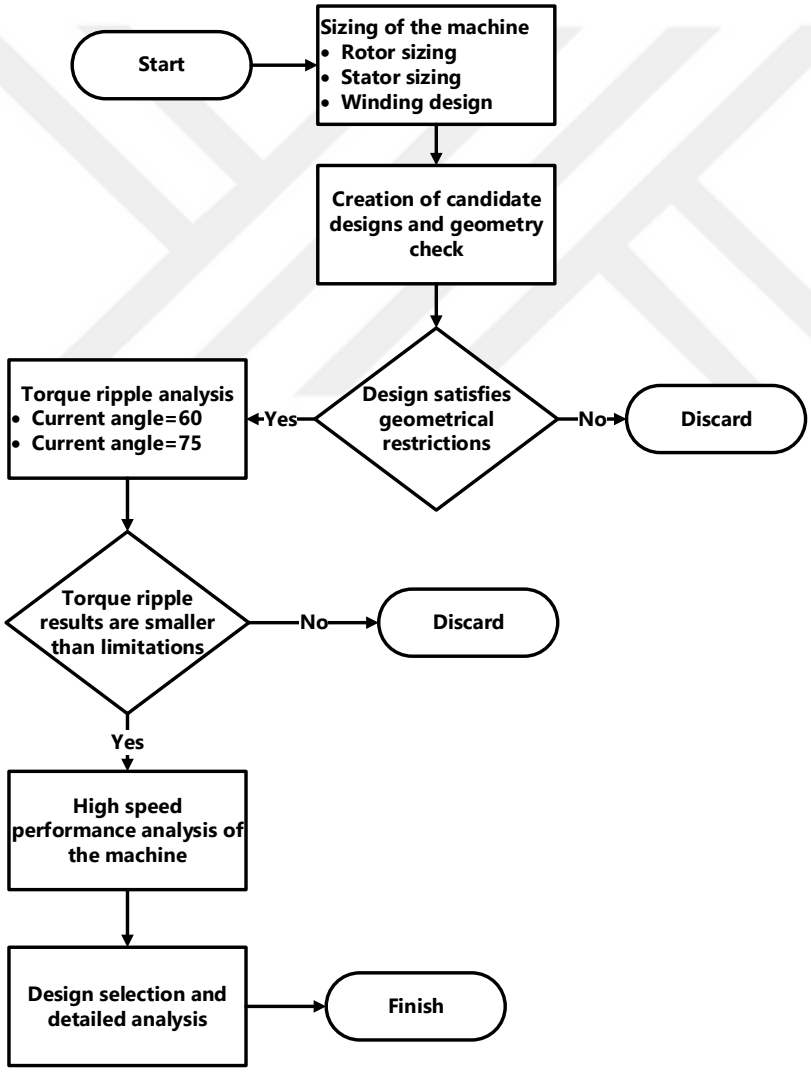

Figure 4.1: Design specifications

The design steps are shown in the flowchart given in Fig. 4.1. In the design process, the first step is machine sizing which includes stator and rotor sizing, and winding design. Then, candidate designs are obtained for the machine after the sizing process. It concludes with so many candidates, so the ones with better performance should be selected. The first elimination is performed according to geometrical restrictions. Then, torque ripples of the remaining designs are examined and second elimination is made according to these results. Finally, the high-speed performance of the designs which pass both eliminations are examined. Moreover, other parameters can be calculated and elimination can be performed by considering these performance parameters such as efficiency, but elimination is not performed by considering the efficiency since efficiency values are close to each other. The efficiency is not calculated, as well. Finally, their high-speed performances are compared and three of them is chosen and analyzed in detail. In this section, the details of these steps are given.

4.3 Machine Sizing

4.3.1 Determination of Rotor Outer Radius

Determination of rotor radius includes iterative mechanical simulations. These simulations begin an initial design which is most probably mechanically not robust, then these results are improved by modifying the rotor radius and rib widths. In the rotor model, ribs are placed at the point where d and q-axes intersect as in Fig.3.6. Thus, there are two identical radial ribs for each flux barrier. Their widths are represented as w_1, w_2, w_3 and w_4 from inner one to outer one for a four flux barrier design, respectively. Each parameter represents each radial ribs in a flux barrier. Tangential ribs width is taken as $1\ mm$ and it is constant for all designs. In order to start mechanical simulations, a starting point should be chosen. For this purpose, some commercial machines are examined and they are compared in Table 4.2 [53].

Lower limit for rotor diameter is chosen as $136\ mm$. As an initial point, the upper limit is chosen as $150\ mm$ and ribs are not added to the first analysis. Then, maximum stress is observed on the rotor when the machine is rotating with $12000\ rpm$. This stress value should be smaller than the yield strength of the material which is 265

MPa. A safety factor around $1.2 - 1.3$ should be also considered.

Table 4.2: Rotor and power values of BMW i3 and Jaguar I-Pace [53]

Model	Machine type	Maximum speed (rpm)	Rotor Diameter (mm)
BMW i3	IPM	11500	178.6
Jaguar I-Pace	IPM	13000	135.2

Table 4.3: Stress values for different rotor geometries

R_r (mm)	w_1 (mm)	w_2 (mm)	w_3 (mm)	w_4 (mm)	Max. stress (kPa)
75	0	0	0	0	1686
75	1	0.75	0.5	0.25	548
72	1	0.75	0.5	0.25	495
72	1.25	1	0.75	0.5	440.3
70	1.25	1	0.75	0.5	407.8
70	1.5	1.25	1	0.75	376.5
68	1.5	1.25	1	0.75	359.6
68	1.75	1.5	1.25	1	317.6
68	2	1.75	1.5	1.25	291.7
68	2.5	2.25	1.75	1.5	254.4

While rotor radius is decreased, radial ribs widths are increased iteratively. As mentioned before, the width of the inner radius is the highest and the uppers are the lowest. As a final decision, the rotor radius is chosen as $68\ mm$. The rib width selection is a trade-off between machine magnetic and mechanical performance. When the radial rib widths are selected as in the last row of Table 4.3, an electrical steel material with around $400\ MPa$ yield strength should be used to stay at safe side when safety factor is chosen as around 1.4. In this design, M470 whose mechanical properties are given in Table 4.4. Moreover, the material whose yield strength is $430\ MPa$ can be used as an alternative such as 35JN210 given in [54] in order to stay in safe side. Finally, mechanical simulation results for the machine which is described by last row of Table 4.3 are given in Fig. 4.2.

Table 4.4: Mechanical properties of rotor material

Mechanical property	Value	Unit
Elastic modulus	201000	N/mm^2
Poisson's ratio	0.3	–
Shear modulus	75000	N/mm^2
Mass density	7700	kg/m^3
Tensile strength	$4.1 * 10^8$	N/m^2
Yield strength	$2.65 * 10^8$	N/m^2

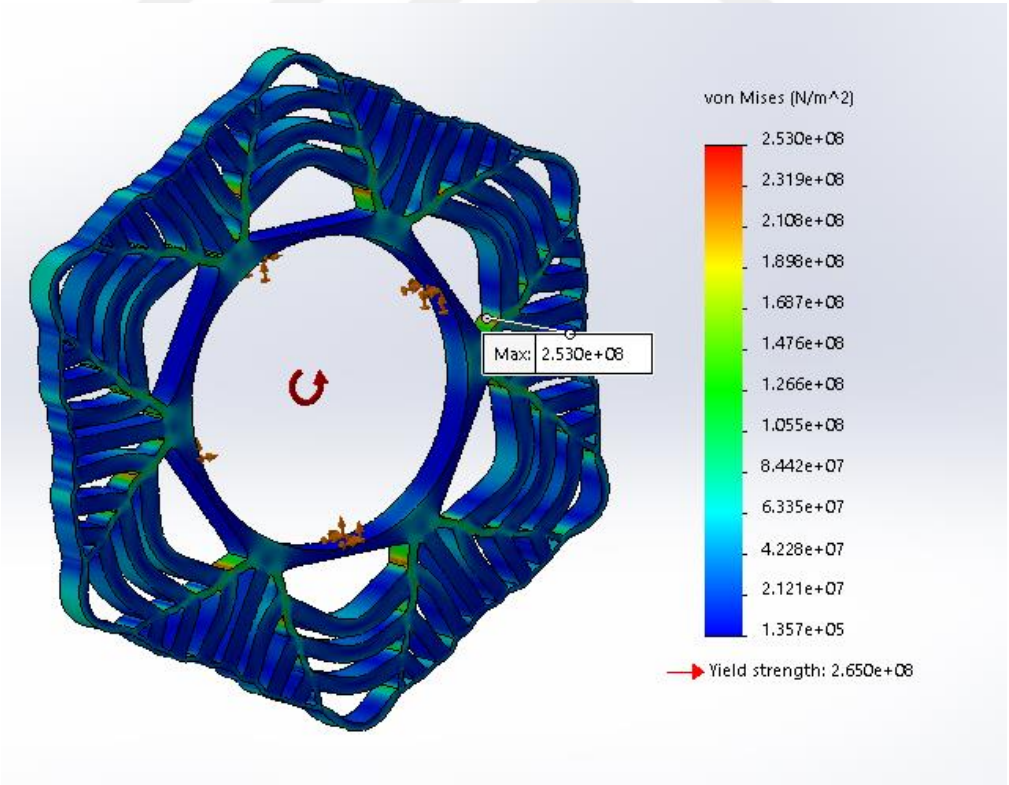

Figure 4.2: Mechanical simulation results for the selected rotor

4.3.2 Stator Design

This section includes the determination of stator parameters such as inner radius and outer radius. Moreover, slot selection and design is performed. Thus, a complete stator is obtained.

The inner radius of the stator can be calculated by using (4.1) where R_r is the outer radius of the rotor and g is the air gap. In the previous section, the rotor radius was calculated and determined to be $68\ mm$. Thus, it is enough to calculate the length of the air gap to obtain the inner radius of the stator.

$$R_{s,in} = R_r + g \tag{4.1}$$

When g is determined, there are two values to take into consideration. The first one is the mechanical limitation which is provided by the manufacturer and is $0.8\ mm$. Another one is the value which is obtained by using (4.2) where P is the power of the machine and p is the pole pair number [55]. The result for a $100\ kW$ machine is calculated as $0.78\ mm$. When both results are combined, the air gap is chosen as 0.8 mm and the inner radius of the stator is equal to $68.8\ mm$ correspondingly.

$$g = \begin{cases} 0.2 + 0.01P^{0.4}, & \text{if } p = 1, \\ 0.18 + 0.006P^{0.4}, & \text{if } p \neq 1. \end{cases} \tag{4.2}$$

Another part of stator design is slot design which includes the determination of slot width to slot pitch ratio and slot height. The first decision to be made when designing the slot is whether the slot or teeth will be rectangular. Rectangular teeth are used in this study to achieve a constant level of saturation throughout the tooth. Thus, the shape of the slots become trapezoidal which is illustrated in Fig. 4.3. Straight slot design must be selected if a hair-pin type winding is going to be used.

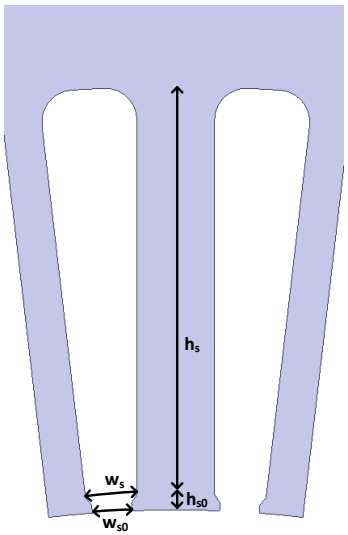

Figure 4.3: Trapezoidal slot and rectangular tooth

There are 4 parameters that need to be defined and calculated. These are slot opening width w_{s0}, slot opening height h_{s0}, slot width w_s and slot height h_s, respectively. Slot opening width is selected $2.5\ mm$ for easier placement of wires and slot opening height is taken as $1\ mm$. In order to calculate slot width, slot width to slot pitch ratio k_s should be determined. Slot pitch can be calculated as in (4.3) where Q is the total number of slots and k_s is calculated by using (4.4).

$$\tau_s = \frac{2\pi(R_r + g + h_{s0})}{Q} \tag{4.3}$$

$$k_s = \frac{w_s}{\tau_s} \tag{4.4}$$

In order to calculate Q, the decision on the selection of integer slot or fractional slot must be made and an integer slot is chosen in this study. Then, slot number per pole per phase q should be selected. Choosing q as high as possible is effective for reducing the effect of slot harmonics. However, it is restricted by mechanical and electromagnetic concerns since choosing q higher causes a decrease in the width of teeth. Thus, q is chosen as 3 and Q is calculated as in (4.5) and found as 54. For

machines with higher pole numbers, it is more common to choose $q = 2$.

$$Q = npq \tag{4.5}$$

In this study, ks will be selected as 0.4 and 0.45. Then, the stators that are obtained by using these two values will be compared and one will be selected. Corresponding w_s values are $3.24\ mm$ and $3.65\ mm$. In order to calculate h_s, MMF analysis of the machine should be performed. For this purpose, a constant and random turn number is chosen and it is 5 for this study. Then, by increasing it by 10 Ampere for each step, currents from 0 to 500 Amperes are applied respectively and maximum torque output of the machine obtained. The results are shown in Fig. 4.4.

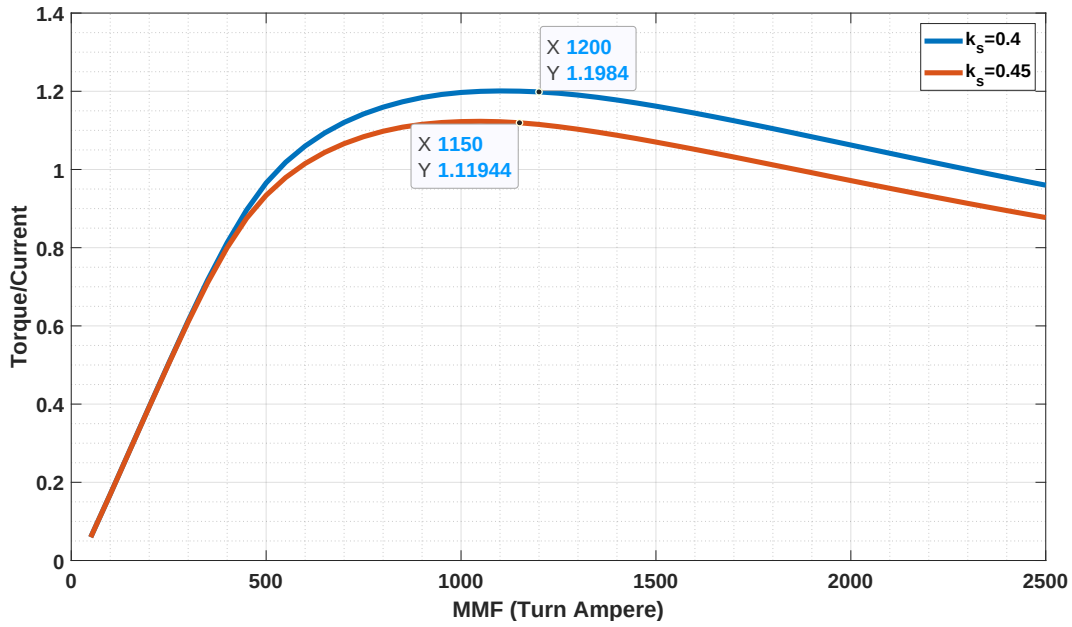

Figure 4.4: Torque/current vs MMF for $k_s = 0.4$ and $k_s = 0.45$

The purpose of doing this is to obtain the nonlinear relationship between torque and current. This relationship is exponential at first but later turns linear and eventually becomes logarithmic. The reason for this is that the machine is saturated. The MMF selection is chosen a little further than the point where saturation begins since the machine is required to be saturated. The operating MMF point is chosen 1150 turn Ampere for k_s 0.4 and 1200 turn Ampere for k_s 0.45. These values are also deter-

mined based on the fact that the torque must be halved if maximum MMF is halved. So far, only MMF value is determined. In order to calculate h_s, the slot area should be determined. For this purpose, fill factor k_f and current density J_{rms} should be determined. Then, the slot area can be calculated by using (4.6).

$$A_{slot} = \frac{MMF}{\sqrt{2} J_{rms} k_f} \tag{4.6}$$

For EV application, current density can be chosen higher than commonly selected values for fan cooloed all purpose machine such as $5\ A/mm^2$ [56]. In this application, it is chosen as $15\ A/mm^2$ and this current density value is desired in critical operation for short time interval. Moreover, water cooling system of EV is used and choice of $15\ A/mm^2$ as current density is not extremely high. Fill factor value is chosen as 0.45. Slot areas are found as $125.71\ mm^2$ and $120.47\ mm^2$ for k_s 0.4 and 0.45, respectively.

After slot area is calculated, h_s can be found. For this, area formula for trapezoid is used. By doing this, an equation is obtaines as in (4.7). After, it is solved, h_s is obtained and it is $26.64\ mm$ and $24.05\ mm$ for k_s 0.4 and 0.45, respectively.

$$h_s^2 sin(\frac{\pi}{Q}) + h_s w_s - A_{slot} = 0 \tag{4.7}$$

In order to get high performance from the machine, the saturation level of the back iron of the stator should be controlled. If it is saturated, machine performance decreases. However, if its saturation level is lower, the machine is over-designed and it could be smaller. For this design, magnetic flux density in the back iron of stator B_{bi} is chosen as $1.5\ T$. Then, the fact that all magnetic flux in the air flows in the back iron of the stator is used in order to calculate h_{bi}. Thus, integration of the magnetic flux density in the air-gap gives all flux flowing through the back iron of the stator and it is given in (4.8) where l_z is the axial length of the machine. Integration of magnetic flux density in the air gap is calculated as in (4.9) where $B_{air,r}$ is the magnetic flux density at the distance r which is the middle point of the air gap.

$$\phi_{bi} = B_{bi} h_{bi} l_z \tag{4.8}$$

$$\phi_{air} = \int_0^{\frac{\pi}{p}} B_{air,r} sin(p\theta) r l_z \, d\theta \tag{4.9}$$

These two equations are equal to each other, the equation which is used in order to calculate h_{bi} is obtained and it is given in (4.10).

$$h_{bi} = \frac{1}{B_{bi}} \int_0^{\frac{\pi}{p}} B_{air,r} sin(p\theta) r \, d\theta \tag{4.10}$$

$B_{air,r}$ is $1.47\ T$ for k_s 0.4 and $1.4\ T$ for k_s 0.45, respectively. Then, h_{bi} is found as $22.33\ mm$ and $21.24\ mm$, respectively. These values are obtained with an over-designed back iron. All stator dimension values are presented in Table 4.5. According to these values, k_s are chosen as 0.4 due to higher torque per volume.

Table 4.5: Stator dimensions for $k_s = 0.4$ and $k_s = 0.45$

k_s	0.4	0.45
Output torque (Nm)	287.62	257.47
Slot width (mm)	3.24	3.65
Slot area (mm^2)	125.71	120.47
Slot height (mm)	26.64	24.05
h_{bi} (mm)	22.33	21.24
Outer stator radius (mm)	118.77	115.09
Total volume $(liter)$	8.86	8.32
Torque/total volume $(Nm/liter)$	32.46	30.95

4.3.3 Winding design

The winding design includes determining the turn number in the slots and whether they are connected to each other in series or parallel. As mentioned in the upper section, the total slot number is 54 and the slot number per phase per pole is equal to 3. Turns in under different poles are connected in series, but they can be connected parallel as well. This choice is not critical for the overall design process since the same winding diagram can be obtained by connected either in series or parallel. However,

when they are connected parallel, there are more options for turn numbers. For example, when they are connected in series, the effective turn numbers are all integer numbers. However, the series connection is enough for this design process.
When determining the number of turns in each slot, the high-speed performance of the machine should be taken into account. For this purpose, other parameters which affect the high-speed performance of the machine such as driver properties and PWM methodology in the driver should be taken into consideration. As a PWM methodology, space vector PWM (SVPWM) is chosen due to the higher phase voltage than sinusoidal PWM (SPWM) with the same DC link voltage.

Table 4.6: Driver parameters

Property	Value
DC voltage (Volt)	600
Modulation index	0.96
Phase voltage (Volt)	220.71
Phase current (Ampere)	283.51
Power factor of the machine	0.75

In order to determine the turn number in each slot, some of the turn numbers are selected. Since this number is discrete, there are not many options. Thus, selected values are 2, 3, 4, 5, and 6. For each turn number, the current limitation due to the driver of MMF limitation should be determined. The current limitation due to the driver is 400 Ampere as can be seen in Table 4.6. MMF limitation is selected as 1200 Ampere.turn in the previous section and corresponding current limitation can be found by dividing MMF limitation by turn number. For these two methods, the corresponding current limitation is the peak of phase current.

After current limitations are determined, high-speed performance can be obtained. High-speed performance analysis will be detailed in the further section, but results for different turn numbers are given in 4.5.

Table 4.7: Current limitations for different turn numbers

Turn number	Current limitation (Ampere)
2	400
3	400
4	300
5	240
6	200

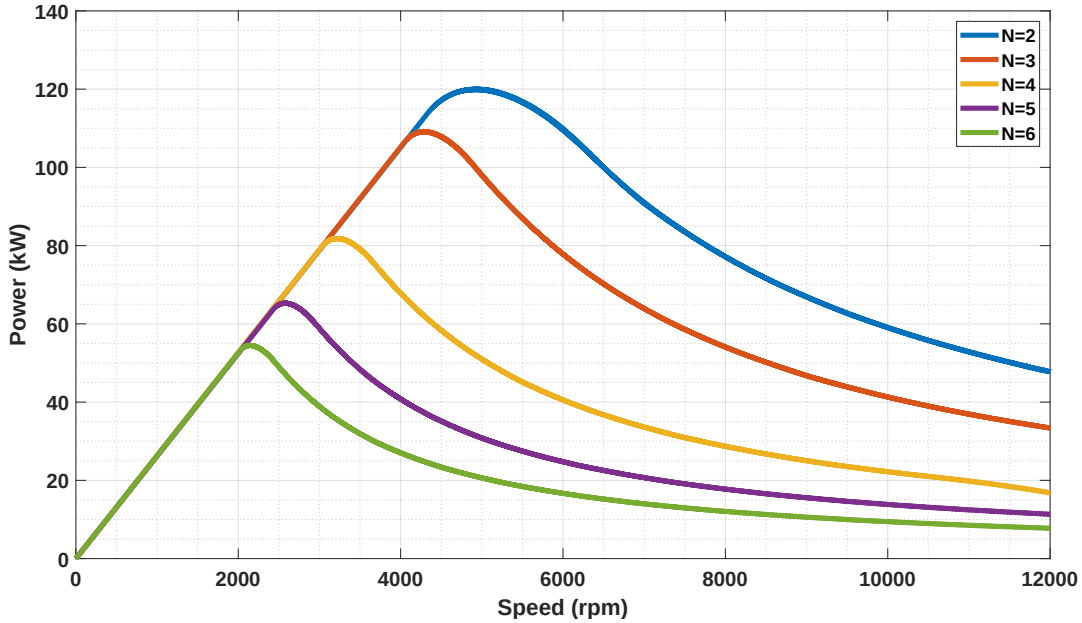

Figure 4.5: Power-speed characteristic for different turn numbers

When the turn number is equal to 4, 5, or 6, the machine can not reach 100 kW since a higher turn number concludes with higher inductance values and the machine reaches the flux limit rapidly. Because of this, their base speed values are smaller. Their output torque value is equal to each other because these values are fixed to 250 Nm by adjusting the axial machine length. This situation can be observed in Fig. 4.5 by examining the slopes of graphs before machines reach base speed and it is observed that they are equal to each other. The reason why 250 Nm is chosen is that the base speed of the machine is fixed around 4000 rpm which is sensible when the maximum

speed of the machine is equal to 12000 rpm.

When the turn number is equal to 2 or 3, the machine can reach 100 kW. Thus, these turn number values can be chosen. However, when the turn number is equal to 2, the maximum power of the machine is around 120 kW. This value is larger than 100 kW, so this concludes with the overdesigned machine. It is important to mention that the compared designs have different axial lengths from which $N = 2$ design has the longest axial length. The closest value to 100 kW is obtained when the turn number is 3.

When turns of sequential coils are connected in series, there is no choice but to choose the turn number 3. However, when it is chosen as 3, the machine is still overdesigned but its degree is acceptable. If a designer wants to decrease its degree, the parallel connection can be a solution. When the maximum power results are examined, the design whose maximum power is 100kW should have a turn number between 3 and 4. These values can be reached by choosing turn number 10 or 11 and connecting poles in parallel. Thus, corresponding turn numbers are equal to 10/3 and 11/3 which are between 3 and 4. However, for this design, the turn number is selected as 3 and connecting in series. In deed the machine was designed for 3 turns per slot as $400x3 = 1200$ turns.Ampere value is reached with 400 A current limit. Design of the machine is an iterative process. Here mostly end results are reported.

4.4 Creation of Candidate Designs

After the machine sizing is completed, candidate designs are created. For this purpose, Method 3 which is rotor design methodology by fixing outer irons width and given in Chapter 3, is used. This is performed by sweeping determined rotor parameters which are k_{wd}, k_{wq}, k_b and β. Firstly, their limits and steps should be determined. Before the limits of these variables are determined, it is observed that there is a relationship between k_{wd} and k_{wq}. Thus, their limits are determined together. For this purpose, the maximum torque outputs of some designs are obtained. k_{wq} values of these machines are kept constant and k_{wd} values are swept. For k_{wq} is equal to 0.8 and 0.9, relationship between k_{wd} and maximum torque is given in Fig. According to Fig. 4.6, lower limit of k_{wd} is chosen as $0.4k_{wq}$ and upper limit is chosen as $0.7k_{wq}$.

The lower limit and upper limit for k_{wq} are chosen as 0.6 and 0.95, respectively.

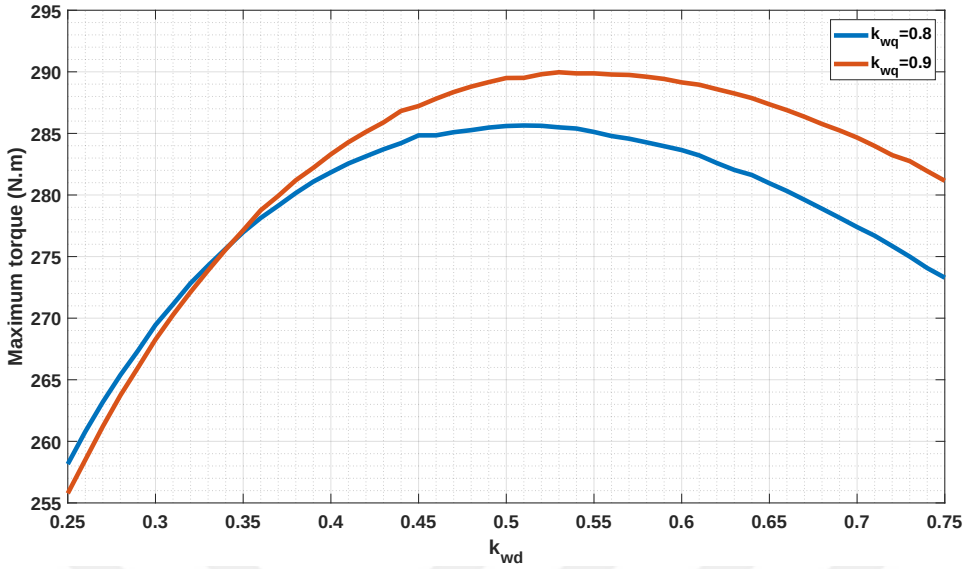

Figure 4.6: Maximum torque vs k_{wd} for $k_{wq} = 0.8$ and $k_{wq} = 0.9$

In order to determine limits of k_b and β, mechanical concerns are taken into consideration. All limitation values are shown in Table 4.8. As a result, 19152 candidate designs are obtained. After that, dimensions of all candidate designs should be obtained by using (3.26). After all, dimensions are obtained, the first elimination is performed by considering the realization of the rotor and its fabrication. Thus, the minimum iron bridge thicknesses is set to $3\ mm$, and the minimum flux barriers thicknesses to $1.5\ mm$. Moreover, shaft radius is restricted between $20\ mm$ and $40\ mm$. Finally, 7887 candidate designs are eliminated and design process is continued with 11265 candidate designs.

Table 4.8: Limitations and steps for variables

Variable	Lower limit	Upper limit	Step
k_{wq}	0.6	0.95	0.05
k_{wd}	$0.4k_{wq}$	$0.7k_{wq}$	0.01
k_b	0.8	1	0.04
β (deg.)	2	10	0.4

4.5 Torque Ripple Analysis

The fundamental problem of SynRMs is higher torque ripple than other conventional machines such as IMs and PMSMs. Because of this fact, their torque ripple values should be calculated carefully. k_{wd}, k_{wq}, k_b and β values affect the torque ripple, but the most effective variable on torque ripple is β. This variable is defined in order to decrease fluctuation of instantaneous torque. Nevertheless, all candidate designs depend on not only β but also k_{wd}, k_{wq} and k_b since high speed performance of these designs will be compared in the next stage.

Another critical value that affects the torque ripple is the current angle. Torque ripple varies with current angle, dramatically. Thus, the current angle on which simulations are performed should be selected carefully and it is not effective to select only one current angle in order to examine torque ripple. Thus, two current angles are selected. This selection is performed by observing the current angles that machine operates. Motor generally requires a current angle between 60-65 degrees. However, in the FW region, it requires up to 80 degrees for a while. By considering these values, torque ripple analysis will be performed at current angles of 60 and 75 degrees. Firstly, analysis at 75 degrees is performed with 60 degrees. Then, an elimination is done and analysis is performed for remained candidates.

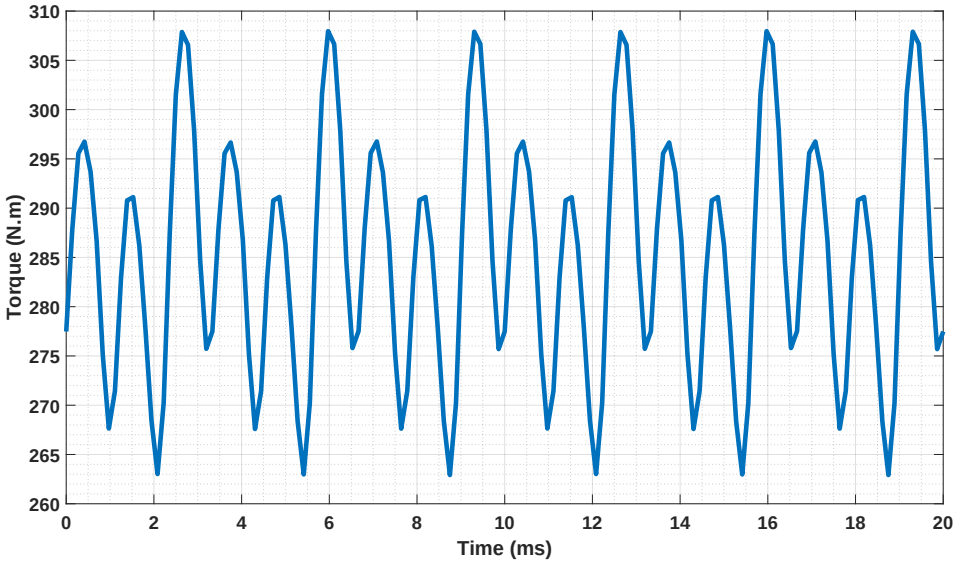

Figure 4.7: Torque for a one electrical period

Torque ripple analysis is performed by using ANSYS MAXWELL 2D software. Since there are so many candidate designs, it is important to determine the time interval for simulation. For this purpose, a machine is simulated for one period and results are illustrated in Fig. 4.7. Torque repeats itself 6 times in one period as can be seen in Fig. 4.7. Thus, it is enough to simulate one-sixth of one electrical period.
Moreover, the ribs are not included in the machine in this analysis since the presence of these ribs increases the analysis time due to the local saturation on these ribs. Moreover, ribs decrease the output torque of the machine. However, in this case, only torque ripple is considered. A decrease in the torque is compensated by adding PMs in further chapters. In order to illustrate the effects of ribs on torque and torque ripple, three arbitrary designs are chosen and their torque results are obtained and presented in Figs. 4.8 and 4.9 with and without radial ribs. The aim of this step is to choose the best design in general. The order of torque ripple of these three arbitrary designs does not change in presence of ribs. Design 3 has the highest torque ripple in two cases while Design 1 has the lowest torque ripple where torque ripple is a percentage and calculated as in (4.11). Thus, the order of torque ripples is the same as desired. Design parameters and torque ripple results are given in Table 4.9.

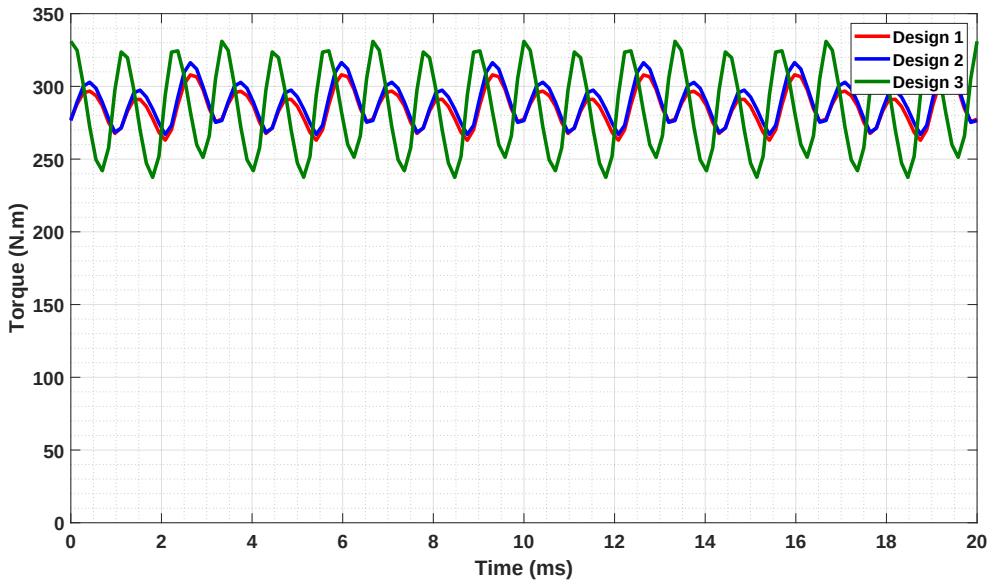

Figure 4.8: Torque for a one electrical period for three designs without ribs

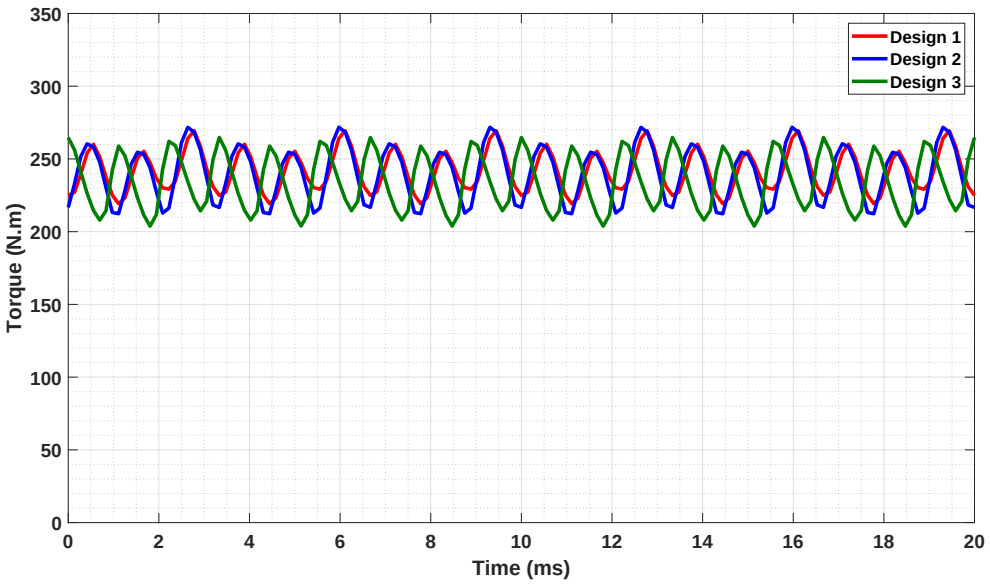

Figure 4.9: Torque for a one electrical period for three designs with radial ribs added

$$Ripple(\%) = \frac{T_{pp}}{T_{avg}} 100 \tag{4.11}$$

Table 4.9: Ripple results of 3 random designs with and without ribs

Design name	(k_{wd},k_{wq},k_b,β)	Ripple without ribs (%)	Ripple with ribs (%)
1	(0.55,0.9,1,6)	16.73	20.76
2	(0.55,0.9,0.9,4)	17.09	24.78
3	(0.55,0.9,0.8,2)	32.83	26.03

Due to the high number of candidate designs, the first analysis is performed for a 60-degree current angle and 11265 simulations are performed. It takes 1.63 days. These results are given in Fig. 4.10. In order to decrease the candidate design number, an elimination is performed with respect to limitations. This limitation can vary according to the results. If it is chosen as 8%, 10%, 12% and 15% remained candidate design numbers are 927, 2110, 3215 and 5172, respectively. Since torque ripple increases after adding ribs, the limitation should be chosen as small as possible. Thus, the limitation is chosen as 10%.

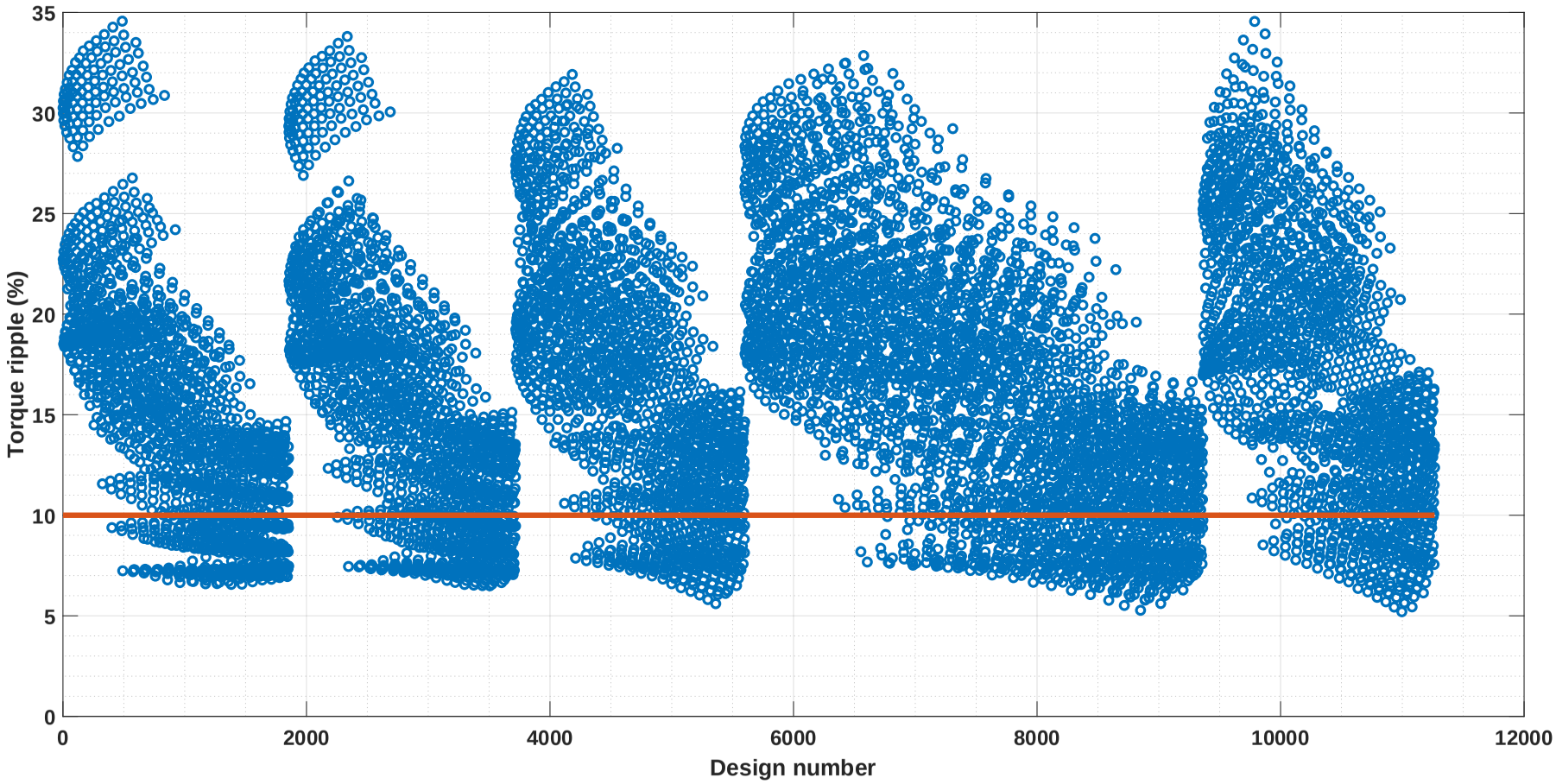

Figure 4.10: Torque ripple results of 11265 candidate designs when current angle is 60 degree

After torque ripple elimination for 60 degree current angle is performed, remained candidate designs are simulated when the current angle is 75 degree. 2110 simulations are performed and it takes 0.31 days. Torque ripple results are given in Fig. 4.11. Torque ripple limitation is chosen as 12% for this case and the number of remained candidate designs is 918.

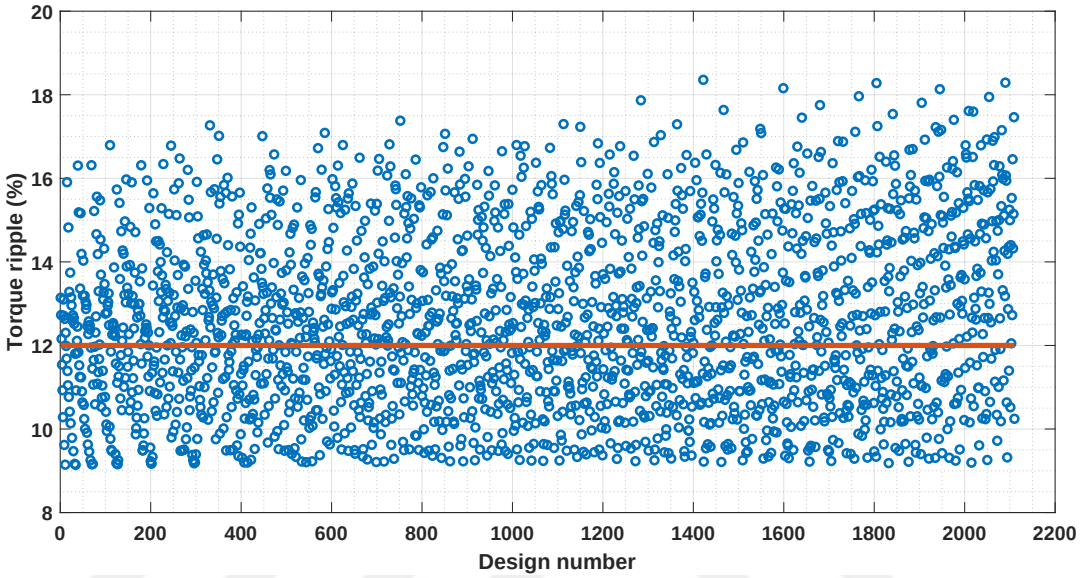

Figure 4.11: Torque ripple results of 2110 candidate designs when current angle is 75 degree

4.6 High Speed Performance Analysis

In Section 2.5, high speed performance of SynRMs is investigated and detailed. In brief, their high-speed performance is poor due to their singly exciting nature. In this section, their torque-speed and power-speed characteristics are obtained by using a proposed method. After they are obtained, the results are compared and a design is chosen. Moreover, the effect of rotor design on high-speed performance is illustrated. Flowchart for high-speed performance analysis is given in Fig. 4.12.

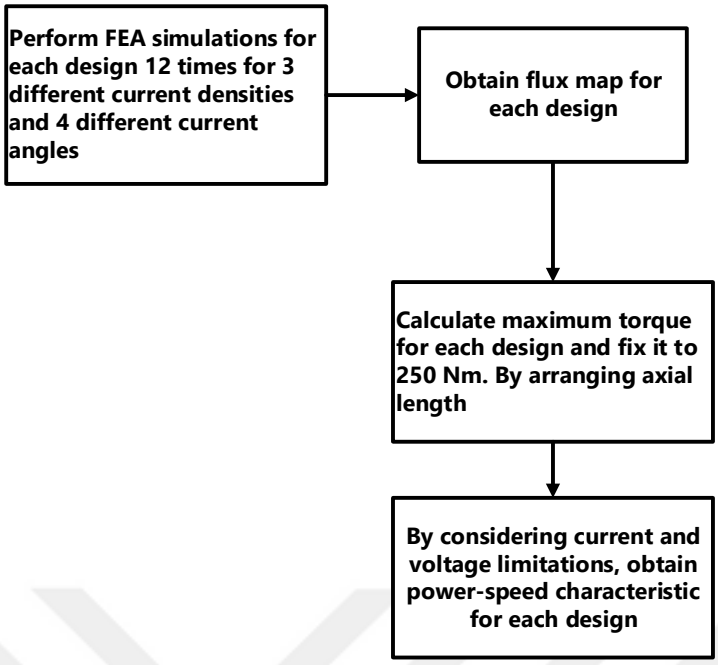

Figure 4.12: Flowchart for high-speed performance analysis

In order to obtain the power-speed characteristic of the machine, dq axes flux linkage λ_d and λ_q values should be known. However, these values are different for each operation point due to the nonlinear nature of the machine and their dependency on current and position. It is a long process to make a simulation for each operation point for each machine. Thus, curve fitting is used in order to calculate these values. For curve fitting, λ_d and λ_q values should be obtained for some points. An operation point can be defined by using two values: current value and current angle. Instead of the current value, the current density is chosen and it is chosen as 11, 13, and 15. Current angle is chosen as 45, 55, 65 and 75. Finally, it concludes with 12 simulations for each candidate. Simulation results are obtained in terms of three-phase components. These components can be converted into d and q-axis components by using Clark and Park equations which are given in (4.12) and (4.13), respectively. Moreover, when these values are calculated, end winding effects are ignored since the stator is same for all machines and end winding have the same effect on each design.

$$\begin{bmatrix} \lambda_\alpha \\ \lambda_\beta \end{bmatrix} = \begin{bmatrix} 1 & \frac{-1}{2} & \frac{-1}{2} \\ 0 & \frac{\sqrt{3}}{2} & \frac{-\sqrt{3}}{2} \end{bmatrix} \begin{bmatrix} \lambda_A \\ \lambda_B \\ \lambda_C \end{bmatrix} \tag{4.12}$$

$$\begin{bmatrix} \lambda_d \\ \lambda_q \end{bmatrix} = \begin{bmatrix} cos(\theta) & -sin(\theta) \\ sin(\theta) & cos(\theta) \end{bmatrix} \begin{bmatrix} \lambda_\alpha \\ \lambda_\beta \end{bmatrix} \tag{4.13}$$

Firstly, flux linkage values should be obtained. For this purpose, ANSYS MAXWELL is used. For each design, 12 simulations are performed. Thus, the total number of simulations is high. So, simulation time should be determined clearly. In Fig. 4.13, flux values for one period is given and it is observed that flux values repeat themselves 6 times in a period. Thus, it is enough to simulate for one-sixth of a period. Moreover, since only average flux linkage values are required, only few simulation steps are enough. Totally, 11016 simulations are performed and it takes 1.6 days. As a result, all simulations which are performed to get torque ripple results and flux linkage values take 3.54 days.

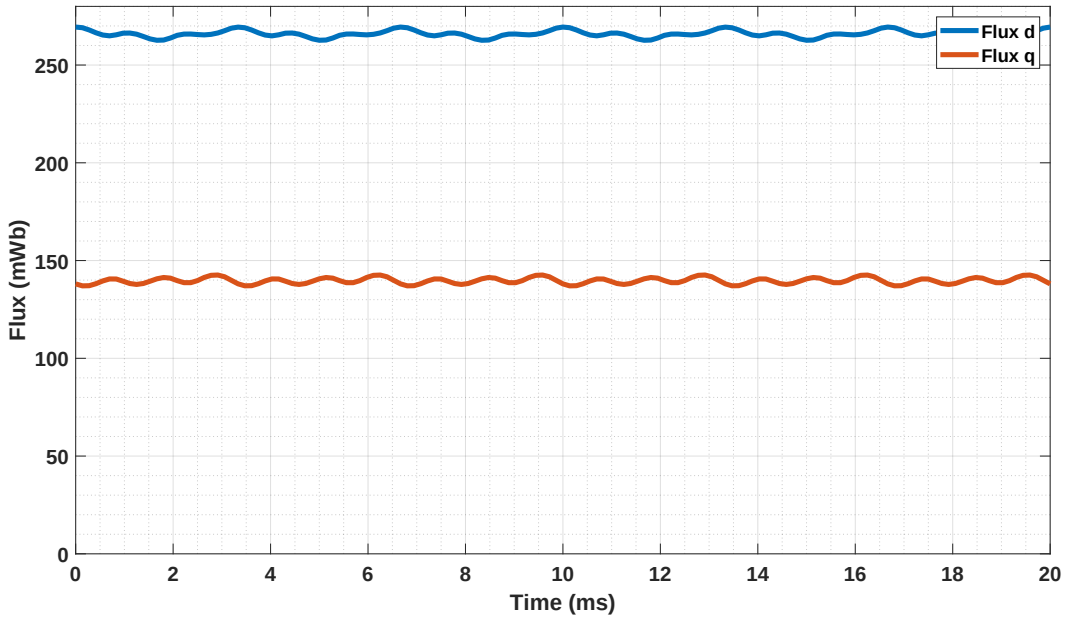

Figure 4.13: λ_d and λ_q results for an exemplary machine for one electrical period

In order to perform curve fitting to flux linkage values, their dependency on current

and current angle should be annihilated. For this purpose, the definition of these flux linkage values is used as can be seen in (4.14) and (4.15), where α_i^e is the current angle.

$$C_{q1} = \frac{\lambda_q}{I_s sin(\alpha_i^e)} \tag{4.14}$$

$$C_d = \frac{\lambda_d}{I_s cos(\alpha_i^e)} \tag{4.15}$$

Due to the behavior of λ_q, its constant can be as in (4.16), alternatively. These two methods gives the same result in the high-speed region, approximately. In this thesis, C_{q1} is chosen and used.

$$C_{q2} = \frac{\lambda_q}{I_s} \tag{4.16}$$

After C_{q1} and C_d are obtained, it is observed that they are approximately linear. Thus, the linear least-squares method which is the least-squares approximation of linear functions to data is applied by using MATLAB fit function. Options of the function are set to default and 'poly22' is chosen as a polynomial model. This is called quadratic surface function and our case is quadratic surface due to the dependency on current angle and current. Then, surface fit can be performed by using (4.17) and (4.18) in terms of current and current angle.

$$C_q(I_s, \alpha_i^e) = p_{00,q} + p_{10,q} I_s + p_{01,q} \alpha_i^e + p_{20,q} I_s^2 + p_{11,q} I_s \alpha_i^e + p_{02,q} \alpha_i^{e2} \tag{4.17}$$

$$C_d(I_s, \alpha_i^e) = p_{00,d} + p_{10,d} I_s + p_{01,d} \alpha_i^e + p_{20,d} I_s^2 + p_{11,d} I_s \alpha_i^e + p_{02,d} \alpha_i^{e2} \tag{4.18}$$

After these values are calculated, flux linkage d and q values can be recalculated easily by using (4.14) and (4.15).

As a result, d and q-axis flux linkage values are gathered for all desired points. The current angle is taken between 45 and 90 degrees and current is chosen to vary be-

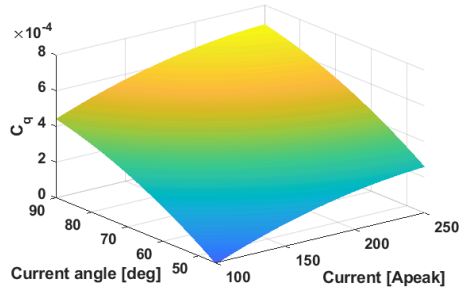

(a) Fitted C_q values

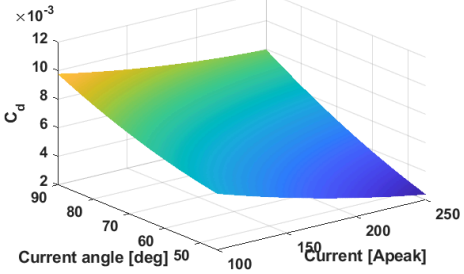

(b) Fitted C_d values

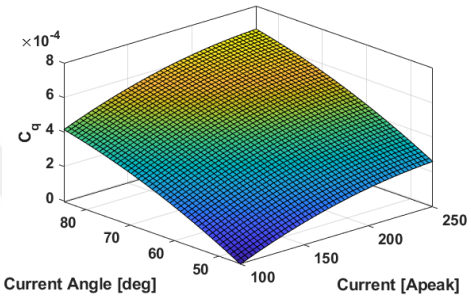

(c) C_q for chosen FEA values

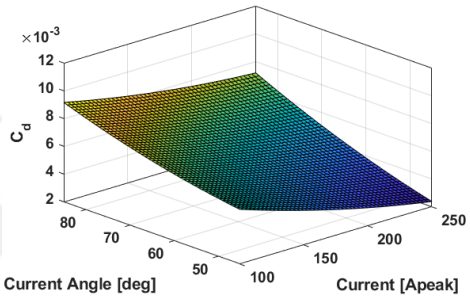

(d) C_q for chosen FEA values

Figure 4.14: Fitted FEA value

tween one-fourth of the current limitation and the current limitation. By using flux values, the speed-power characteristic of the machine should be obtained. For this purpose, flux limit should be considered and it is given in (4.19).

$$v_s = \sqrt{(\omega_e L_d i_d + R_s i_q)^2 + (-\omega_e L_q i_q + R_s i_d)^2} \leq \frac{V_{dc}}{\sqrt{3}} \tag{4.19}$$

Firstly, maximum torque is calculated by using curve fit again. For this purpose, the maximum current value is chosen and torque value is obtained for 3 current angles which are 45, 60, and 75. Then, these values are used for curve fit. The curve fit is performed by using MATLAB fit function, again. In this case, there is one parameter which is the current angle. Thus, 'poly2' is chosen as the polynomial model. Moreover, torque is annihilated from current angle dependency by using (4.20) since dependency of torque on current angle resembles $sin(2\alpha)$. Then, C_t is calculated by using (4.21). Then, torque values for each current angle are calculated by using

(4.20).

$$C_t = \frac{T_{em}}{sin(2\alpha_i^e)} \tag{4.20}$$

$$C_t(\alpha_i^e) = p_{0,t} + p_{1,t}\alpha + p_{2,t}\alpha_i^{e2} \tag{4.21}$$

The result of curve fit operation and FEA are given in Fig. 4.15 for an exemplary machine and it can be seen that there is a only small discrepancy between the results. It is observed that torque results are approximately equal to each other when the current angle is greater than 40 degree. When the current angle is smaller than 40 degree, there is a huge difference between the results. However, the machine never operates in these current angle values.

Then, the machine is resized in order to get $250\ Nm$ as output torque. This is done by changing the axial length of the machine since the output torque and flux linkage change linearly with the axial length of the machine. Resultant axial length can be calculated by using (4.23) and resultant flux linkage values are calculated as in (4.24) and (4.25).

$$T_{em} = \frac{3}{2}p(\lambda_d i_q - \lambda_q i_d) \tag{4.22}$$

$$l_z^{'} = l_z \frac{250}{T_{max}} \tag{4.23}$$

$$\lambda_d^{'} = \lambda_d \frac{250}{T_{max}} \tag{4.24}$$

$$\lambda_q^{'} = \lambda_q \frac{250}{T_{max}} \tag{4.25}$$

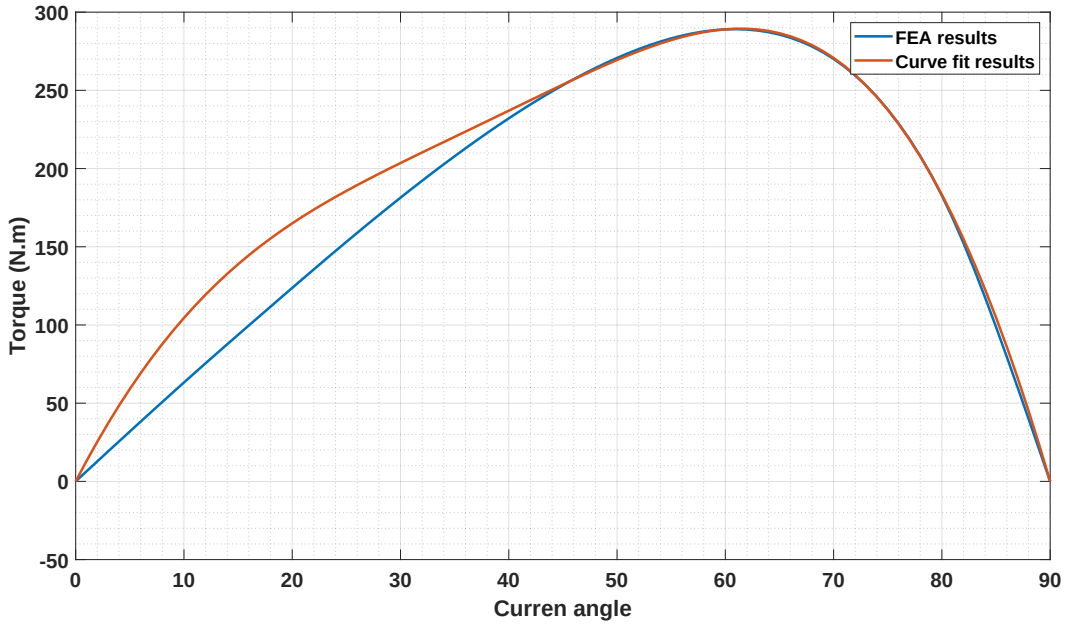

Figure 4.15: Comparison of torque result calculated at each point with FEA and obtained from 3 FEA results with curve fitting

By using flux values, torque for each point is calculated by using (4.22). Thus, for each current and current angle pair, torque values are gathered. After torque values are obtained, these values should be assigned to speed values. For each speed value, a function is called once. This function checks the flux limit by using (4.26) by ignoring R_s for each point. If the flux limit is exceeded, this current and current angle pair is eliminated for this speed. Then the maximum torque among the remained values is chosen. This value is the maximum torque at which the machine can operate at this speed. This process is repeated for each speed value and the power-speed characteristic of the machine is obtained eventually.

$$\sqrt{\lambda_d^{'2} + \lambda_q^{'2}} \leq \frac{V_{dc}}{\sqrt{3}\omega_e} \tag{4.26}$$

For 918 candidate designs, the power speed characteristic is obtained. Thus, their power at maximum speed is obtained. In Fig. 4.16, Pareto front of power at maximum speed and the sum of torque ripples when the current angle is 60 and 75 degrees, is given. Torque ripple values are in a restricted interval due to the eliminations performed before. However, power at maximum speed varies between 22 kW and 36 kW.

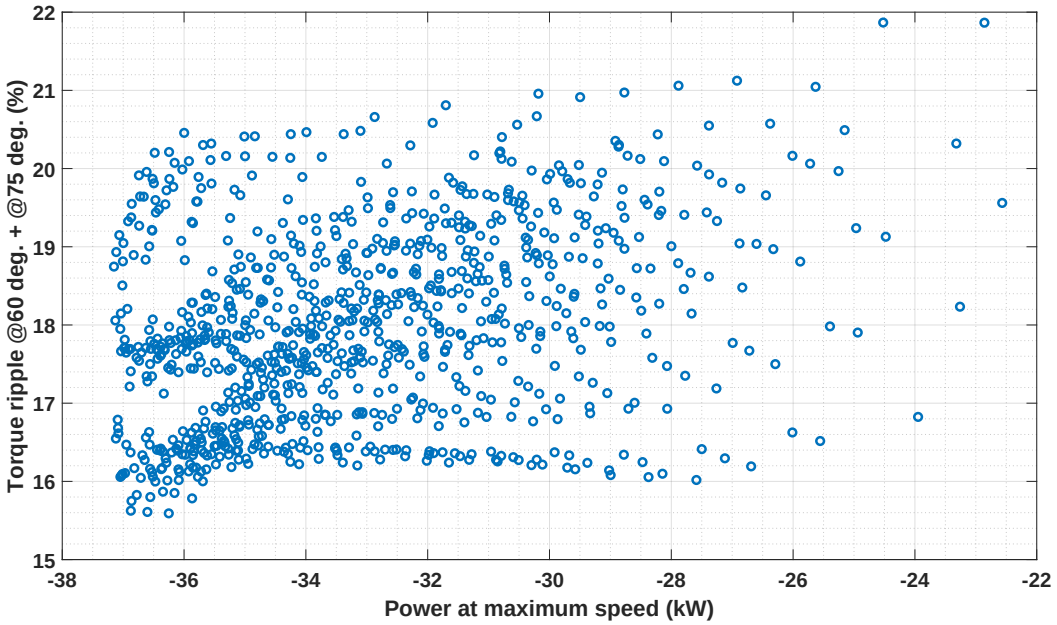

Figure 4.16: Tork ripple vs power at maximum speed

4.7 Final Design Selection and Results

After all, designs are obtained, some of these designs are selected and their detailed results are given. For this purpose, three of these designs are selected. These designs are selected among good, moderate, and bad designs in order to observe the difference of parameters and performance that is their power output at 12000 rpm.

For each design, torque-speed, power-speed, current-speed and current angle-speed characteristics are given in Figs. 4.17, 4.18 and 4.19, respectively. For each design, maximum torque is fixed to $250\ Nm$ as can be seen from the torque-speed characteristic of each machine. However, their base speed values are different. While the good design has the highest base speed value, the bad design has the lowest base speed as can be seen in Table 4.10. Moreover, torque at the maximum speed of each machine is different and it concludes with a difference between power at maximum speed.

As can be seen in Figs. 4.17, 4.18 and 4.19, maximum powers that machines can achieve are different. There is a correlation between maximum power and power at maximum speed. Moreover, the maximum power of the machine is higher if the base

Table 4.10: Parameters and results of good, moderate and bad design

	Good	Moderate	Bad
(k_{wq},k_{wd})	(0.95,0.62)	(0.75,0.44)	(0.6,0.24)
(k_b,β)	(0.84,7.2)	(0.96,7.2)	(0.88,7.2)
ΔT at 60 (%)	6.53	7.51	7.87
ΔT at 75 (%)	9.53	11.13	11.69
P_{12000} (kW)	37.05	31.81	22.57
T_{12000} (Nm)	29.47	25.42	19
n_{base}	4250	4050	3620
Axial length (mm)	173.31	174	188.84
Total mass (kg)	141.30	143.08	47.61
Maximum kW/kg	2.70	2.46	1.99
kW/kg @12 krpm	0.90	0.74	0.47
Max. loss kW	2.89	3.22	3.55
Loss coef. kW/m^2	22.25	24.81	25.29

speed of this machine is higher since the maximum torque of the machines are equal to each other and maximum power is equal to the product of the base speed and the maximum torque of the machine.

Due to the current limit which is given in Section 4.2, machines draw $400\ A$ peak current until they reach the base speed. The current angle is also the same until the base speed is reached since the methodology is performed by considering maximum torque per ampere (MTPA) conditions. After the base speed is reached, the machine goes into the FW region. Then, the current begins to decrease and the current angle starts to increase due to the flux limit. The current of good design decreases to about $130\ A$. This value is about $110\ A$ for moderate design and $90\ A$ for bad design. On the other hand, the current angle for good design rises to about 82 degrees. This value is about 80 degrees for moderate design and 78 degrees for bad design. Also, loss coefficients are presented in Table 4.10 and it is different for three different designs. According to [57], it can reach to $40\ kW/kg$ for water cooling systems. Thus, all design is suitable for water cooling.

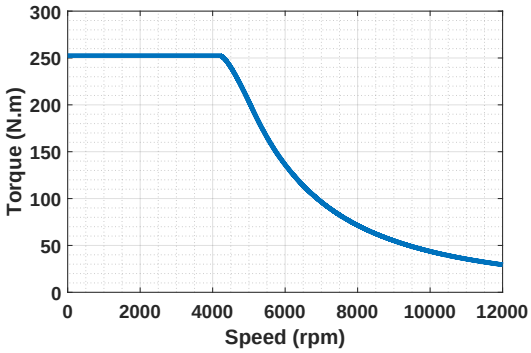

(a) Torque vs speed

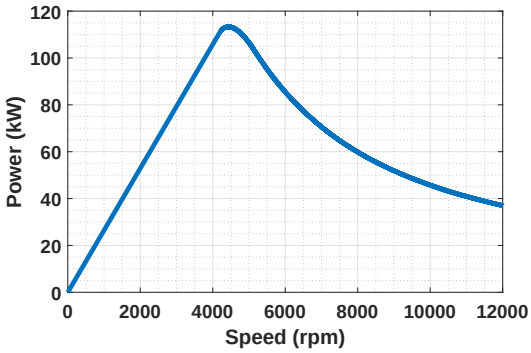

(b) Power vs speed

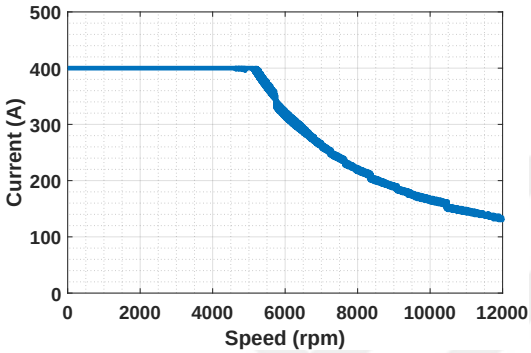

(c) Phase current vs speed

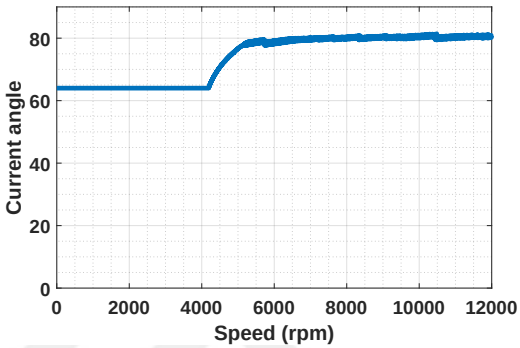

(d) Current angle vs speed

Figure 4.17: Results of the good design

4.8 FEA Validation

Results which are presented above are obtained by using curve fitting applied to few FEA results. Thus, these results should be validated by using Finite Element Analysis (FEA). For this purpose, firstly a model is implemented in ANSYS MAXWELL 2D. Then, field results are obtained and given. Finally, four points are selected and results are obtained by using FEA. For this purpose, current, current angle, and torque values are obtained in the curve fitting process for 1500, 5000, 8000, and 12000 rpm. Then, the machine is simulated in these conditions, and results are compared.

The design which is given in Fig. 4.20 is simulated in ANSYS MAXWELL. One-sixth of the machine is simulated since the machine has six poles and it repeats itself 6 times. Thus, slave/master boundaries are used and results for the full machine are obtained. Moreover, d-axis of the machine and phase A should be aligned.

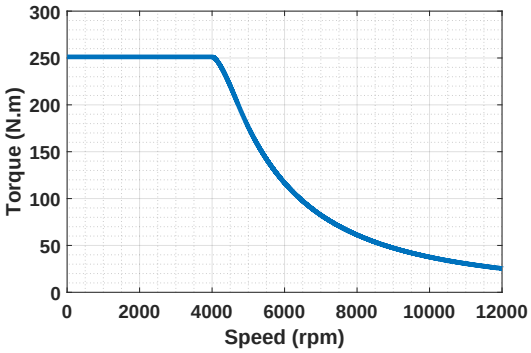

(a) Torque vs speed

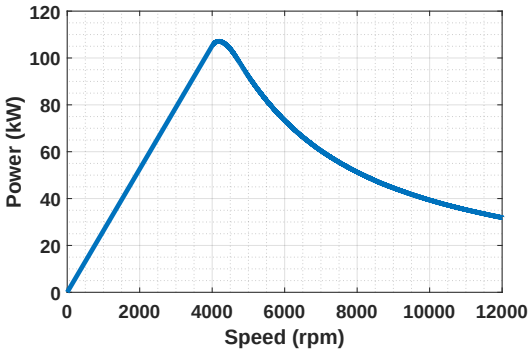

(b) Power vs speed

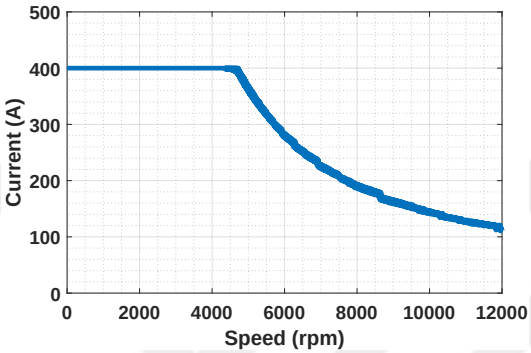

(c) Phase current vs speed

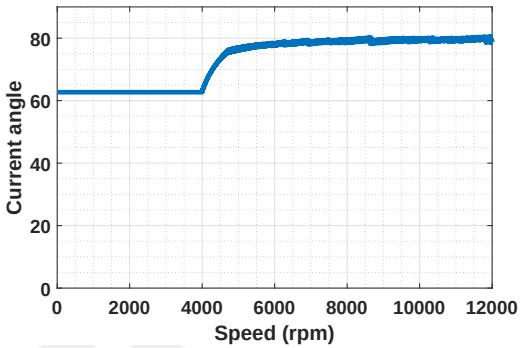

(d) Current angle vs speed

Figure 4.18: Results of the moderate moderate design

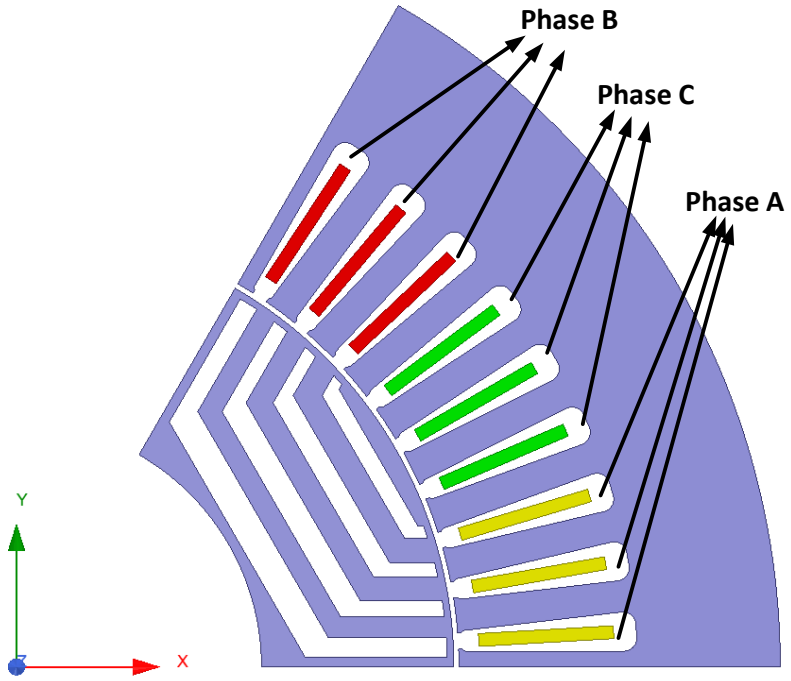

Figure 4.20: FEA simulation model of the good design

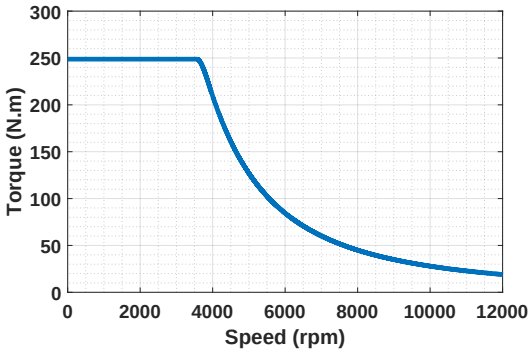

(a) Torque vs speed

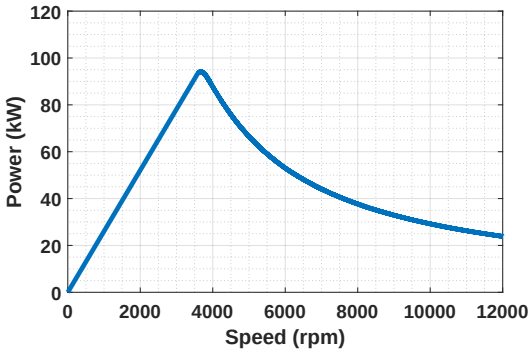

(b) Power vs speed

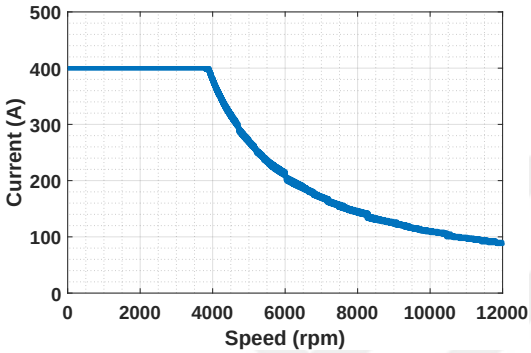

(c) Phase current vs speed

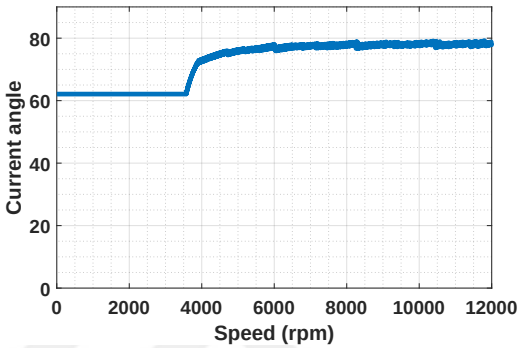

(d) Current angle vs speed

Figure 4.19: Results of the bad design

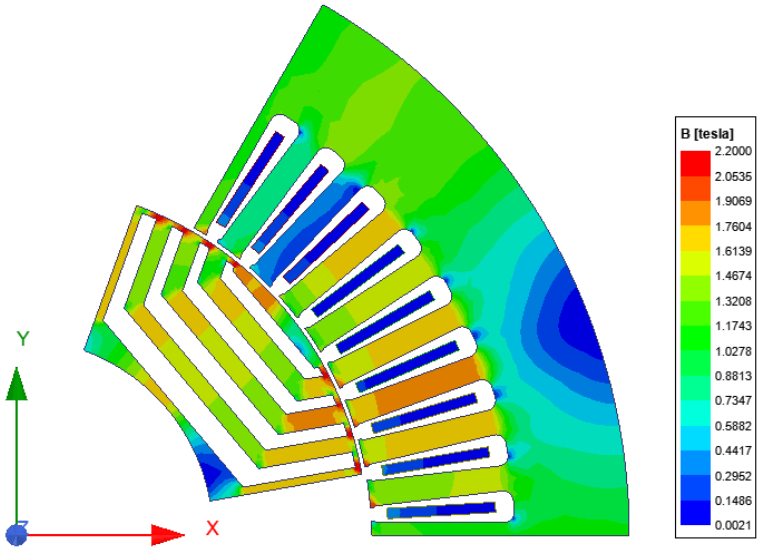

Figure 4.21: Field results of the good design when phase current is 400 A

In Fig. 4.21, field result of the machine is given when time is zero. As expected, magnetic field density is around $1.5\ T$ in stator yoke. Moreover, initial position of the rotor can be observed. Torque, phase current and current angle values from method with curve fitting are presented in Table 4.11 along with FEA results obtained at each particular point. Results are close to each other. Thus, curve fitting results are validated. In Fig. 4.22, torque results for 1500, 5000, 8000, and 12000 rpm.

Table 4.11: Results for good design at 4 different speed values

Speed (rpm)	1500	5000	8000	12000
Average torque (Nm)	252.31	203.73	71.36	29.42
Phase current (A)	400	400	216.67	134.17
Current angle	64	76.6	79.8	80.9
Average torque in FEA (Nm)	249.17	202	66.24	26.66
Torque ripple in FEA ($\%$)	6.22	10.45	16.87	17.59

4.9 Discussion

As discussed before, SynRMs have poor high-speed performance. As can be seen in Figs. 4.17a, 7.12a and 4.19a, torque of the machine decreases suddenly after base speed. However, this is different for each design. Correspondingly, the rotor design affects the speed-power characteristic of the machines. This concludes that rotor geometry affects the high-speed performance of the machine. The important thing is how it affects high-speed performance. When rotor parameters of three designs are examined in Table 4.10, it is observed that k_{wq} values of designs are completely different. It is higher for good design and lowers for bad design. The reason is that the average torque of the machine increases with k_{wq}. Thus, the torque density of the machine increases as well. When the average torque is fixed to $250\ Nm$, the axial length of the machine with higher torque density is smaller. Thus, this machine reaches to flux limit with a higher base speed and its high-speed performance is better. Moreover, when results are examined, the machine with better high-speed performance has higher maximum power. This is also about higher base speed. When torque is fixed to a constant value, the maximum speed of the machine is proportional

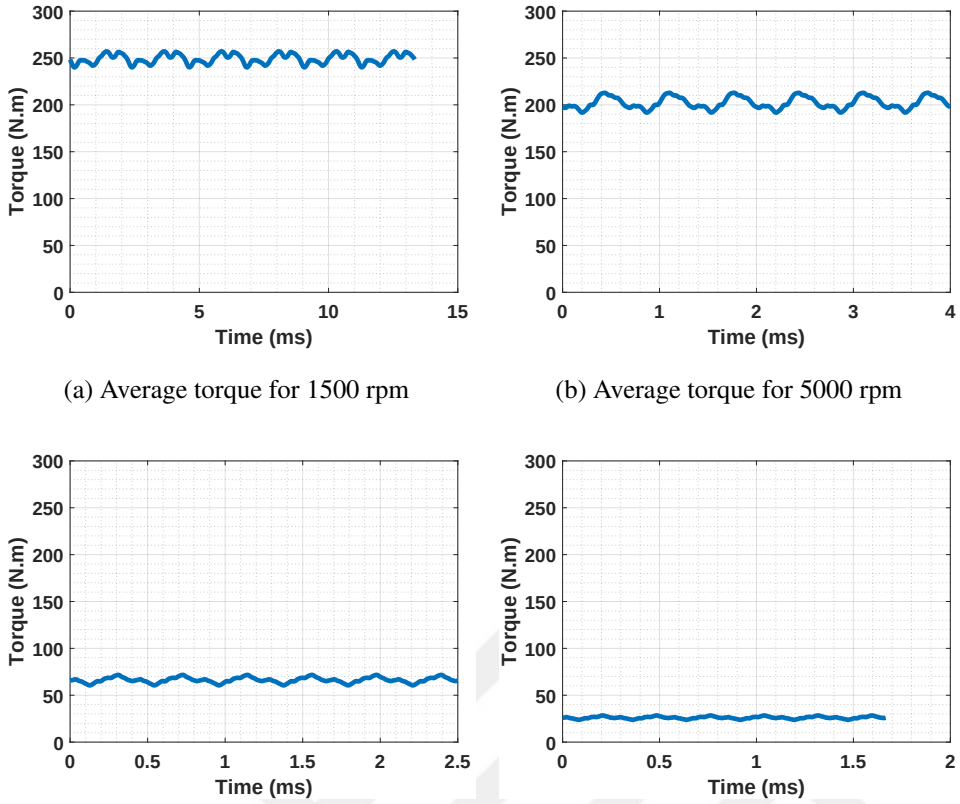

(a) Average torque for 1500 rpm

(b) Average torque for 5000 rpm

(c) Average torque for 8000 rpm

(d) Average torque for 12000 rpm

Figure 4.22: FEA torque results of the good design

to base speed directly. Moreover, k_{wd} values also affect average torque and it affects the machine performance with k_{wq}. However, it is limited by values which are given in Table 4.8. As shown before, it depends on k_{wq}.

When other parameters are examined, there are some valuable results. The candidate designs which are simulated for high-speed performance have β values in a narrow interval. These candidates pass ripple eliminations, so it verifies that β values affect torque ripple results. When the effect of k_b is examined, it is observed that there is not any algorithm. This concludes that k_b value has an impact on designs when other parameters are meaningful. For a good design, it can not be said that k_b value is either low neither high. It can be low or high according to other parameters.

As mentioned before, the maximum torque of the machine is fixed to $250\ Nm$ for each design. However, changing this value affects the results. If it is chosen lower than $250\ Nm$, the axial length of the machine gets smaller and flux values decrease.

Thus, the machine reaches to flux limit with a higher base speed. Since maximum torque decreases and base speed increases, the change of the maximum speed of the machine is very small. On the other hand, power at the maximum speed has improved by decreasing the maximum torque of the machine. In order to improve design, maximum torque can be decreased but the base speed of the machine should be limited. The ideal value for base speed is around 4500-5000 rpm. These values are targetted.

In summary, high-speed performance and torque ripple results can be corrected with a well-designed rotor. However, the high-speed performance of the machine is still poor. It can be corrected fully by adding PM to flux barriers. A well-designed rotor for high-speed performance can decrease the amount of PM. This topic is further examined in the next chapter.

CHAPTER 5

PM ASSISTED SYNCHRONOUS RELUCTANCE MACHINE DESIGN

PMs are insertede into the flux barriers of SynRMs in order to increase machine performance. The aim is to increase the power factor and to correct the high-speed performance of the machine. Especially, it is critical for applications that require a wide extended speed range, such as EV applications.

Until this section, a $100\ kW$ SynRM is designed, and machine performance is tried to be increased in the absence of PMs. It is found that SynRms can not deliver constant power for a wide extended speed range. However, a SynRM with a better power-speed characteristics is a good basis for the PMaSynRM design since the quantity or quality of PM can be decreased. Consequently, the cost of the machine decreases as well.

Influence of adding PMs on the high-speed performance of different SynRMs is presented in this chapter. There are mainly two types of comparisons. Firstly, PM assites versions of the good and moderate designs obtained in Chapter 4 are compared. Secondly, the use of the ferrite and NdFeB types of magnet materials is investigated. Thus, the required PM material and cost with different PM types can be compared.

5.1 PM Material Selection

Rare earth magnets are generally used in high-performance machines due to their remanent flux and high coercivity. However, besides their high costs, they face supply-chain issue so their price is very unstable. As an alternative, ferrite PMs are used. They are cheaper, but they have a lower energy density. In order to compare the designs with rare-earth PM and ferrite PM, one of the PM material is selected as ferrite,

and another one is selected as NdFeB. There is a great variety of PM properties of the selected PMs are presented in Table 5.1.

Table 5.1: Selected PM properties

	Ferrite	NdFeB30
Relative permeability	1.06	1.04
Remenant flux (T)	0.395	1.10

5.2 PMaSynRM Design

The design process of PMaSynRM is performed by determining the quantity, property, and the placement of the PMS. Firstly, PMs are placed in flux barriers through the q-axis. The property of the PMs is determined by the magnezitaiın direction and the PM material. As explained in Chapter 2, its magnetization direction is chosen as the -q direction. Thus, the performance of the machine can be increased. Moreover, two PM materials are used: Feerite and NdFeB. NdFeB has better quality, but its prices are higher. Thus, the optimum choice should be made.

Another parameter is the quantity of PM in the machine. Machine performance increases with the quantity of PM. However, after some point, machine performance is saturated, and adding more PM does not necessarily cause a significant improvement in machine performance. This point is different for designs with NdFeB and ferrite PMs. In order to observe the relationship between the required quantity and type of PM, some results are gathered. To achieve this, four designs, that are presented in Fig. 5.1, are created. The first one includes PMs, whose lengths are a quarter length of the each flux barrier widths in the q-axis. The second one includes twice as many PM as the machine in the first case, and the third one includes twice as many PM as the machine in the second case. In other words, PM material fills half of the flux barriers through the q-axis in the second case, and it fills the whole flux barriers through the q-axis in the third case. The final case is that PM is added to the sides of flux barriers. Moreover, as can be seen in Fig. 5.1, radial ribs are included in simulations. The radial rib widths calculated in Table 4.3 are used. Adding PM increases the average torque of the machine, and adding radial ribs decreases it. They compensate each

other, and new average torque is obtained.

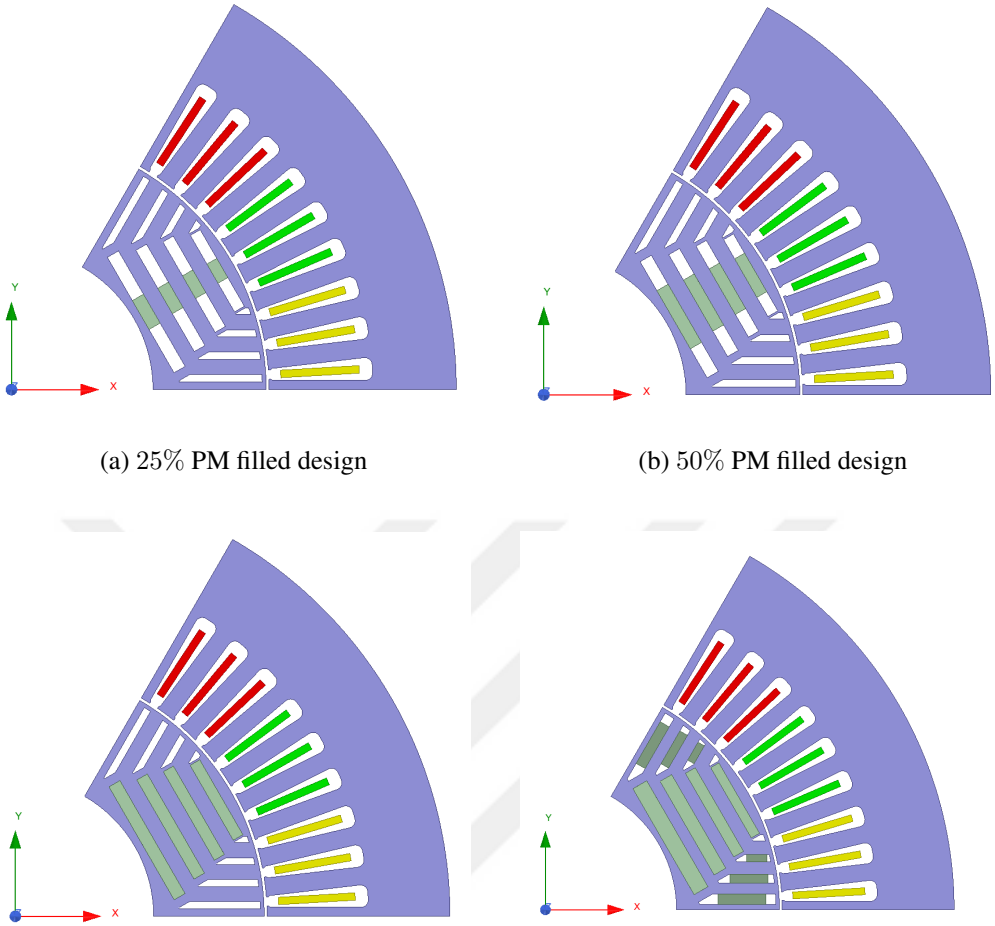

(a) 25% PM filled design

(b) 50% PM filled design

(c) 100% PM filled design

(d) 100% PM filled design with additional PM at sides of flux barriers

Figure 5.1: FEA views of PM assisted Synchronous Reluctance Machine

5.2.1 Design with 25% filled PM

In this section, the first case is examined for good and moderate designs both with ferrite and rare earth PMs. In this case, the maximum torque of the machine is fixed to 250 $N.m$ by adjusting axial length again. Results for good and moderate designs with ferrite PM and NdFeB PM are given in Figs. 5.2 and 5.3, respectively. Also, numerical values are given in Table 5.2.

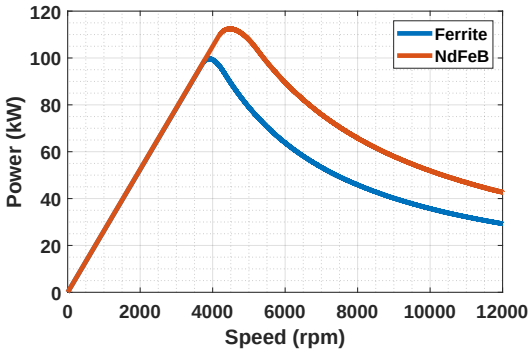

(a) Power vs speed

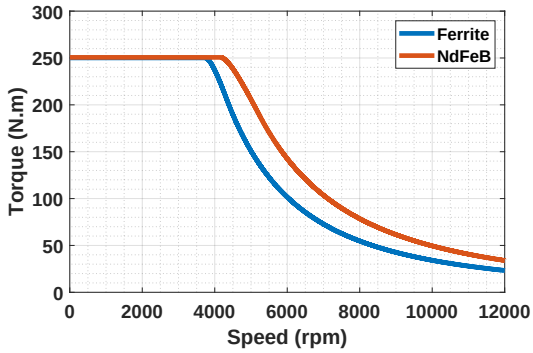

(b) Torque vs speed

Figure 5.2: Results for good design with 25% filled PM

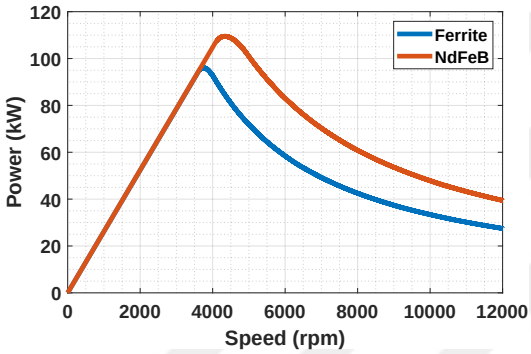

(a) Power vs speed

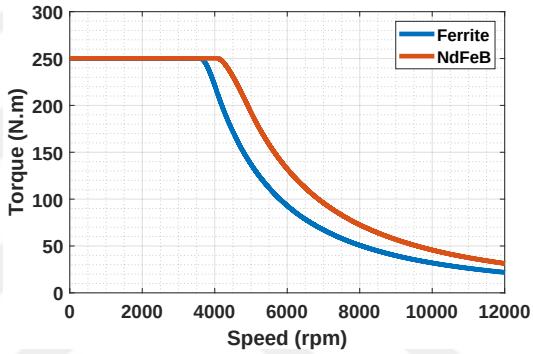

(b) Torque vs speed

Figure 5.3: Results for moderate design with 25% filled PM

As can be seen in Figs. 5.2 and 5.3, performance of the machine is better with NdFeB. In these Tables, maximum torque of the machine is given when axial length is 200 mm. However, it is not still good for high-speed applications. Also, the good design still has better performance than the moderate design. Thus, it can be said that the initial design process without radial ribs and PMs is a valid approach.

Designs with ferrite PM have a worse torque and power than designs without PM and ribs, as can be seen in Table 4.10 and 5.2. The reason for this situation is that ribs decrease the performance of the machine. Since the quality of ferrite magnets is lower, they can not compensate for the decrease with this amount of PM. Power at a maximum speed of good design decreases 20.8%, and it decreases 13.75%. On the other hand, machines with NdFeB can compensate for the decrease on machine

Table 5.2: Results for 25% filled PM machines

	Good/ferrite	Good/NdFeB	Mod./ferrite	Mod./NdFeB
Axial length (mm)	192.79	184.44	189.24	176.55
Max Torque (Nm)	250	250	250	2501
Max. power (kW)	99.55	112.42	96.09	109.44
P_{12000} (kW)	29.32	42.63	27.44	39.42
Base speed (rpm)	3734	4160	3616	4070

performance due to the existence of the ribs. It increases power at maximum speed 15.06% for good design and 27.95% for moderate design.

5.2.2 Design with 50% filled PM

Since machine performance does not reach the desired levels, the widths of magnets are doubled in the machine. Results for good and moderate designs are given in Figs. 5.4 and 5.5, respectively. Important operating points are given in Table 5.3. Although the widths of magnets are doubled, the amount of magnets is not doubled. As can be seen in Tables 5.2 and 5.3, length of the machines decreases. Thus, the volume of PM is less than double of the previous case's volume. Moreover, the base speed of the machines with NdFeB closes to 6000 rpm. As a design choice, it can stay like this, or it can be decreased by changing the maximum torque of the machine. Increasing the maximum torque of the machine decreases the base speed. Since the output torque of NdFeB machines is higher, the results can still be good when the maximum speed is increased.

As can be seen in Table 5.2 and 5.3, power at high speed of good design increases 0.69% with ferrite PM. It can be said that ferrite can compensate for the decrease of power at maximum due to the ribs in this case. Moreover, there is a 125.37% improvement when NdFeB is used for good design. On the other hand, there is a 16.72% improvement with ferrite for moderate design. However, a good design's power is higher than the moderate design's power at high speed. Finally, adding NdFeB improves power at a maximum speed 136.87%.

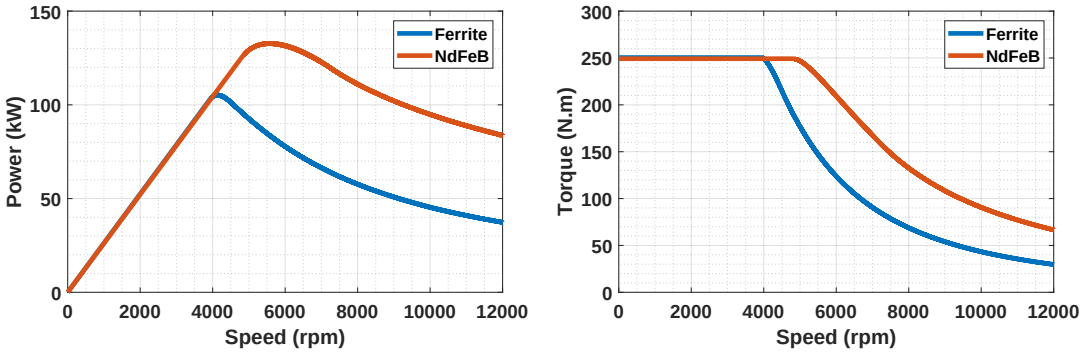

(a) Power vs speed

(b) Torque vs speed

Figure 5.4: Results for good design with 50% filled PM

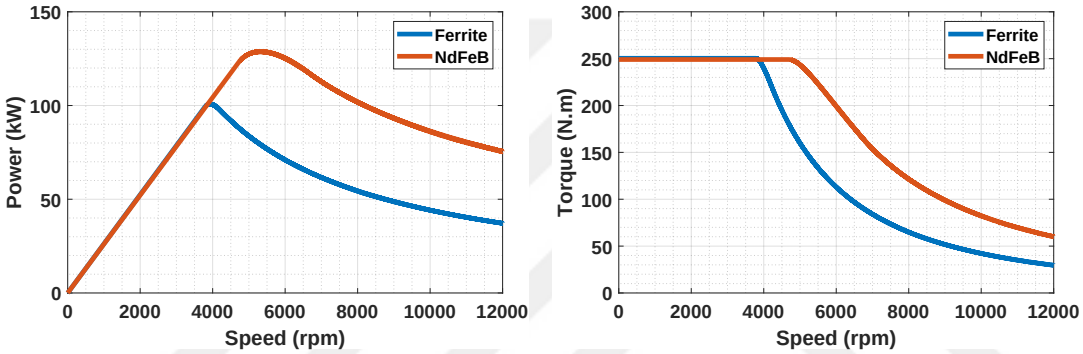

(a) Power vs speed

(b) Torque vs speed

Figure 5.5: Results for moderate design with 50% filled PM

In this case, adding NdFeB gives satisfying results, but it can be improved. However, there are not still satisfying results when ferrite PM is added.

5.2.3 Design with 100% filled PM

In order to improve the machine performance further, the amount of magnets is increased in the machines. As can be seen in Figs. 5.6 and 5.7 and Table 5.4, adding NdFeB PM corrects the machine performance at high speeds. However, it increases the machine performance more than the desired level. Thus, it is an over-designed machine if NdFeB PM is selected, and it is not a good decision to insert PM to all along flux barrier in q-axis. Furthermore, adding ferrite PM to good design increases

Table 5.3: Results for 50% filled PM machines

	Good/ferrite	Good/NdFeB	Mod./ferrite	Mod./NdFeB
Axial length (mm)	185.59	169.14	181.82	161.32
Max. torque (Nm)	250	250	250	250
Max. power (kW)	105.23	132.11	100.70	128.45
P_{12000} (kW)	37.31	83.5	37.13	75.35
Base speed (rpm)	3926	4790	3782	4699

power at high speed 75.68% while it is 90.25% for moderate design.

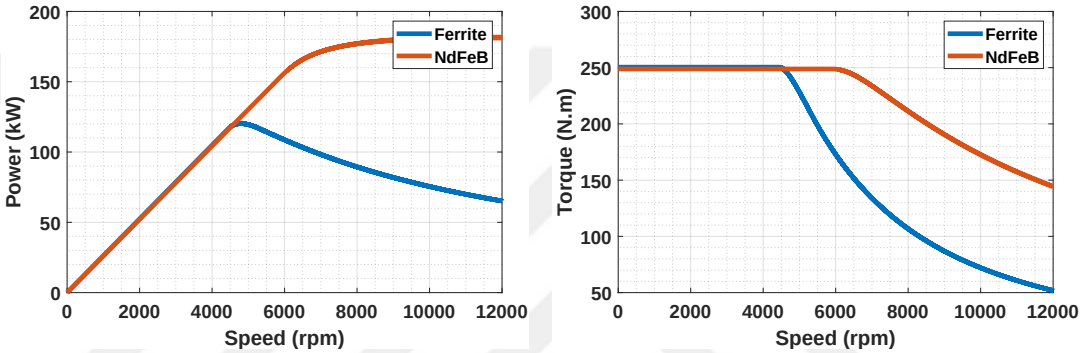

(a) Power vs speed

(b) Torque vs speed

Figure 5.6: Results for good design with 100% filled PM

5.2.4 Design with 100% filled PM and additional PM

This process is only applied to good design with 100% ferrite PM. Moderate design is not considered since its performance is worse than good design with PM. Moreover, designs with NdFeB are not considered for this case since adding more PMs is not required.

In this design, the flux barrier is filled with PM all along the q-axis. Then, extra PMs are inserted into the sides of the flux barriers. These magnets' magnetization direction is in the -q-axis. Then, results for good design are given in Figs. 5.8 and Table 5.5. As presented in Table 5.5, power at high speed of the machine is 88 kW. This value is obtained with 50% filled NdFeB machine. Moreover, the base speed

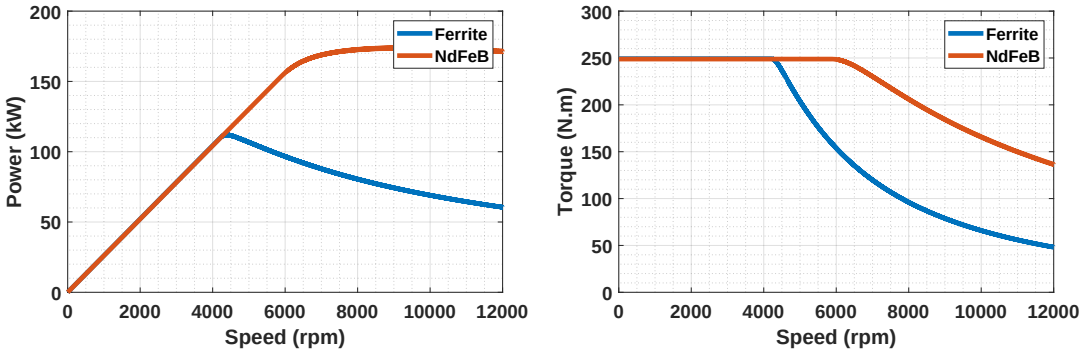

(a) Power vs speed

(b) Torque vs speed

Figure 5.7: Results for moderate design with 100% filled PM

Table 5.4: Results for 100% filled PM machines

	Good/ferrite	Good/NdFeB	Mod./ferrite	Mod./NdFeB
Axial length (mm)	164.12	128.5	162.91	125.24
Max. torque (Nm)	250	250	250	250
Max. power (kW)	120.25	181.77	110.22	173.7
P_{12000} (kW)	65.09	181.77	60.52	171.14
Base speed (rpm)	4455	5919	4217	5874

of the machine is 4523 rpm, which is plausible for the application. Furthermore, the machine's maximum power is lower when it is compared with the results of machines with NdFeB.

In order to increase power at maximum speed, the maximum torque of the machine can be decreased. For this purpose, the upper limit for base speed should be determined. Then, the base speed of the machine can be fixed to the upper limit by iterating the maximum power of the machine.

5.3 Design Selection and Comparison

Design selection is a critical issue since machine performance and cost should be considered together. For this purpose, two designs are selected. One of them is

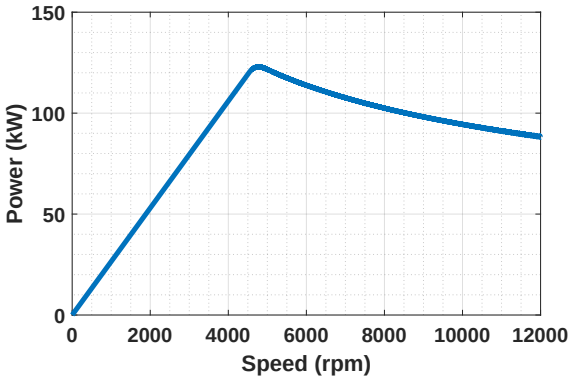

(a) Power vs speed

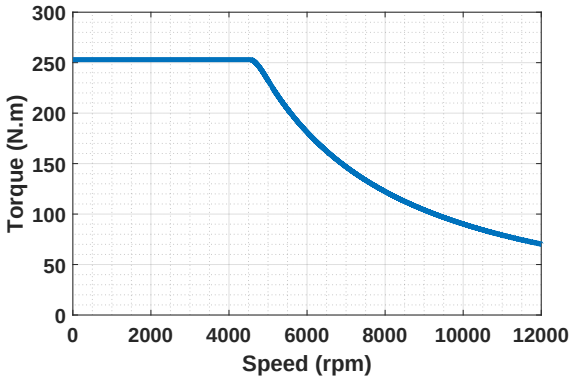

(b) Torque vs speed

Figure 5.8: Results for good design with 100% filled PM with additial PM in d-axis

Table 5.5: Results for full filled PM machines with additional PM in the sides of U-shaped flux barriers

	Value
Axial length (mm)	156.39
Max. torque (Nm)	250
Max. power (kW)	122.92
Max. power at max speed (kW)	88.00
Base speed (rpm)	4523

with ferrite PM, and another one is with NdFeB PM. When results with ferrite PM are examined, the design with 100% filled PM in flux barrier through q-axis and additional PMs is chosen. Another one is with NdFeB PM with 50% filled PM to flux barriers through the q-axis.

Performance results of these machines are given in Table 5.6. Results are close to each other, but the results of the machine with ferrite PM are slightly better. Another comparison is performed according to the amount and cost of PM. These results are given in Table 5.7. Cost of ferrite and NdFeB is taken in [58].

As expected, the machine needs more ferrite PM in volume for approximate performances. However, the mass density of NdFeB is higher, and total required ferrite

Table 5.6: Results for 100% ferrite PM machine with additional PM and 50% NdFeB PM

	100% + additional Ferrite	50% NdFeB
Axial length (mm)	156.39	169.14
Max. torque (Nm)	250	250
Max. power (kW)	122.92	132.11
P_{12000} (kW)	88.00	83.5
Base speed (rpm)	4523	4790
Total mass (kg)	40.08	41.99
Maximum kW/kg	3.07	3.15
kW/kg @12 krpm	2.20	1.99

Table 5.7: Magnet properties for selected designs

	100% + additional Ferrite	50% NdFeB
Volume (cm^3)	95.66	37.631
Density$(\frac{kg}{m^3})$	4900	7500
Mass(kg)	2.81	1.69
Cost per mass $(\frac{\$}{kg})$	11.5	168
Total PM cost ($)	32.32	283.92

magnet mass is 1.66 times the NdFeB mass. Moreover, the cost per mass of NdFeB is much higher than ferrites. Thus, the total cost of NdFeB is much higher than the total cost of ferrite, and it is approximately ten times of ferrite cost. Moreover, when power factor results are examined, it is observed that result is corrected when ferrite PM is added as can be seen in Fig. 5.9. Actually, this value is still not good, but it can be chosen. As a future work, power factor of this machine is corrected. Thus, the final selection is a machine with ferrite PM assisted, and ferrite is filled in flux barrier through q- axis and more PMs are added to sides of the flux barriers.

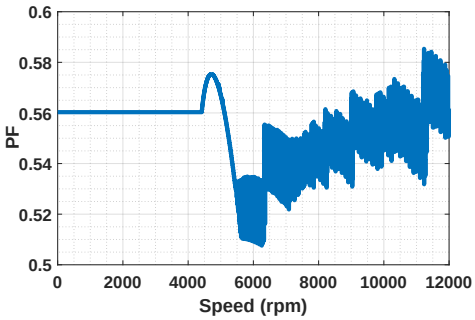

(a) Without magnet

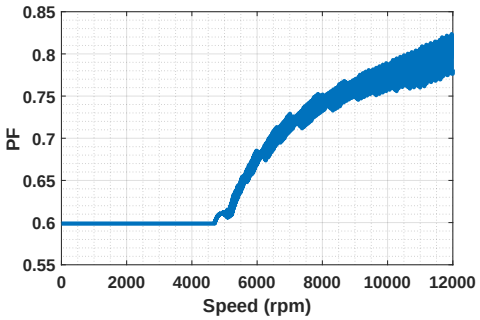

(b) With ferrite PM

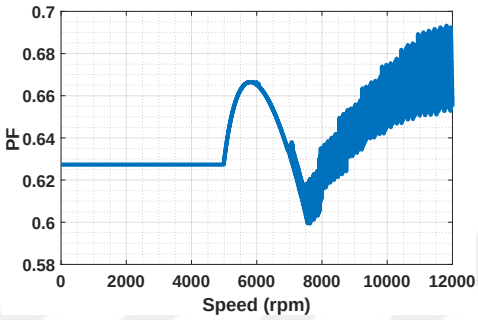

(c) Witf NdFeB PM

Figure 5.9: Power factor results

5.4 Discussion

The high-speed performance of SynRM is weak without PM assistance. It can be increased by designing the rotor of the machine, as presented in this thesis. However, this improvement is not enough. Thus, PM should be introduced to flux barriers. This PM may be ferrite or NdFeB. NdFeB is very expensive. Ferrite is common and cheaper.

The amount of PM affects the machine performance. When ferrite PM is added to the quarter of the each flux barrier through the q-axis, machine performance does not increase dramatically. However, for the same case, NdFeB assisted machine's performance increases noticeably. For both cases, the increases in the machine's high-speed performance are not satisfactory. Then, the amount of PMs is increased. Their widths are doubled, and the machine with NdFeB PM reached satisfying high-speed performance while the machine with ferrite PM does not. In order to get better high-speed

performance with ferrite PM assisted machine, flux barrier is filled fully with PM through q-axis, and more PM is added to the side of flux barriers. Then, resultant designs with ferrite and NdFeB PMs that have satisfying high-speed performances are compared, it is pointed out that the cost of the machine with ferrite PM is lower. Another comment is about rotor design. When the good design and moderate-designed machines are compared, it is observed that the SynRM with a better performance can reach higher power levels with the same amount of PM material. As a result, rotor design affects the required amount of the PM to realize a high power outputs at high speeds.

CHAPTER 6

OPTIMIZATION OF THE ROTOR OF THE 100 KW SYNRM

The stator designed in Chapter 4 will be assumed in this chapter and only the rotor is optimized. If required,stator parameters can be included in the optimization process as in [59]. Due to nonlinear nature of SynRMs, the optimization process includes numerical calculations since the numerical calculations take a long time, it is important to shorten computation time. Generally, studies try to optimize all geometric parameters that are the dimensions and positions of rotor flux barriers individually [29–31]. In this study, it is aimed to reduce the number of rotor geometrical parameters, but still get good designs. In Chapter 3, rotor parameterization is performed, and the rotor is defined with four parameters for all flux barrier numbers. Defining the rotor with fewer parameters shortens the computation time.

Studies generally focused on optimizing torque ripple and average torque of the machine [29–31]. As pointed out before, SynRM has weak high-speed performance but power output of SynRMs at high speeds is not usually taken into account for optimization. Cupertino [26] tries to optimize the high-speed performance of the machine by observing the q-axis flux of the machine. In this chapter, the rotor optimization to obtain a low torque ripple and a high power output in the FW region. For each machine, power speed characteristics are obtained. Thus, any value on power speed characteristic if the machine, such as maximum power and power at maximum speed can be optimized

6.1 Sensitivity Analysis

Before optimization is performed, sensitivity analysis is done. Four parameters define the rotor, and these parameters are optimized to have a good high-speed performance with a low torque ripple. Thus, sensitivity analysis is performed by these parameters which are k_{wq}, k_{wd}, k_b and β.

6.1.1 Sensitivity Analysis for k_{wq} and k_{wd}

Sensitivity analysis for the iron and air ratios in d and q axis that are k_{wq} and k_{wd} should be performed together since they are a related to each other, as pointed out in Chapter 4. k_{wq} and k_{wd} affect the average torque and high-speed performance of the machine. Thus, the average torque of the machine is examined firstly, and then the maximum power at maximum speed is discussed. Those results are presented in Figs. 6.1 and 6.2, respectively. Then it is observed that results are the same for the same k_{wd} values with different k_{wq}. Thus, it is decided that selection of k_{wq} can be made without optimizing it, and k_{wd} can be optimized. When k_{wq} is selected, average torque and power at maximum speed are considered, and it is observed that these values increase with k_{wq}. Thus, k_{wq} should be selected as high possible high. It can be chosen as 0.9 or 0.95. In this case, it is chosen as 0.9. Thus, the number of parameters for optimization is decreased by one, and there are in total three parameters for optimization.

For k_{wd} the lower and upper boundaries, a relationship which is obtained in Chapter 4. is used. This relationship is between k_{wd} and k_{wq} and it states that lower limit for k_{wd} value is $0.4k_{wq}$ and upper limit is $0.7k_{wq}$

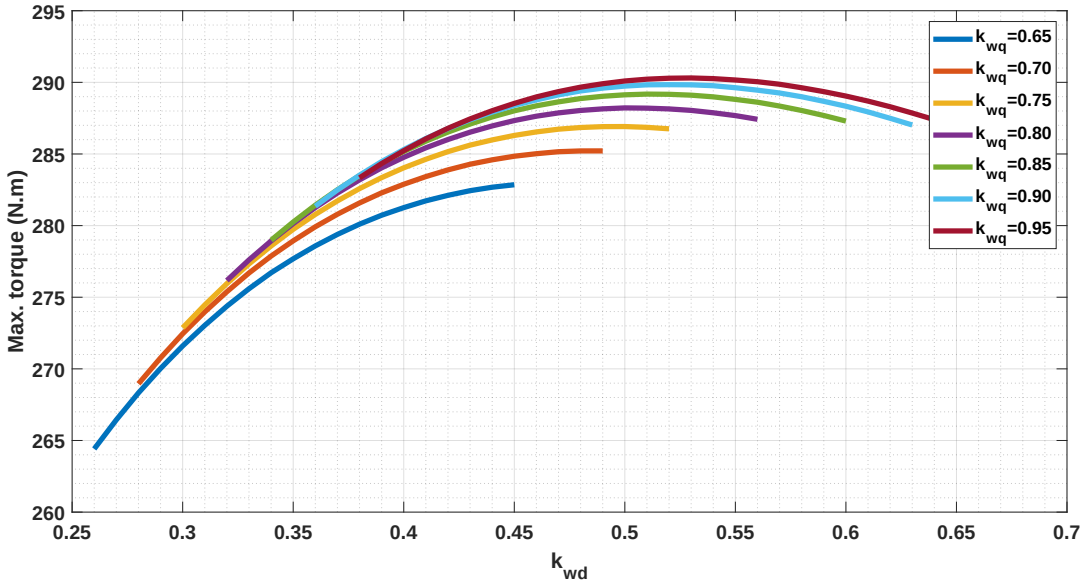

Figure 6.1: Maximum torque vs k_{wd} for different k_{wq} values

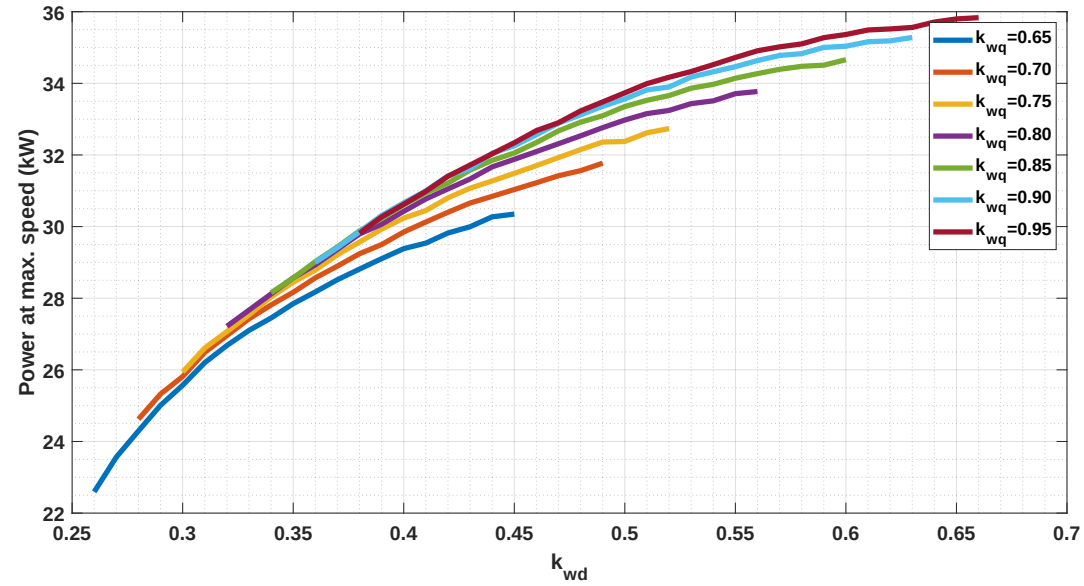

Figure 6.2: Power at maximum speed vs k_{wd} for different k_{wq} values

6.1.2 Sensitivity Analysis for β

Additional opening angle added to the flux barrier that is closest to the air-gapβ affects the torque ripple of the machine, whereas its effect on average torque is negligible.

Thus, sensitivity analysis is performed by observing torque ripple. Bianchi examines the relationship between barrier positions and torque ripple analytically [22, 23]. In this thesis, these studies are followed. Bianchi [22] calculates torque oscillations for independent positions of flux barriers. This equation is converted into to our case which is constant rotor slot pitch in (6.1), (6.2) and (6.3).

$$T_\nu = k_\tau^* \Delta U_r \frac{\hat{K_\nu}}{\nu} sin(\nu \frac{\pi}{2})[sin(\nu(\alpha_m + \beta)) + sin(\nu(\alpha_m + 2\beta))...] \tag{6.1}$$

$$k_\tau^* = \frac{-\mu_0 D^2 l_z}{g} \tag{6.2}$$

$$\hat{K_\nu} = \frac{3\hat{I} k_{w_\nu} N}{\pi D} \tag{6.3}$$

In these equations, ΔU_r is taken as constant. It means that magnetic potential drop on each flux barrier is taken equally. Moreover, the order of torque harmonics is multiples of 6 and $h = 6n$, where n is an integer. Torque harmonics can be calculated by using (6.4) where ν_1 is equal to $1 - 6n$ and ν_2 is equal to $1 + 6n$.

$$T_h = \sqrt{T_{\nu_1}^2 + T_{\nu_2}^2 + 2T_{\nu_1} T_{\nu_2} cos(2\alpha_i^e)} \tag{6.4}$$

When these equations are obtained, some assumptions are made. The first one is that iron ribs are replaced by air. The second one is that width of iron bridges is equal to each other. The third one is that the magnetic saturation occurring in stator and rotor is neglected. This is actually an assumption that is important to mention since saturation occurs in stator and rotor. Thus, the results deviate and do not give the exact ripple value of the machine. However, it gives the β angle interval, which has minimum torque ripple. Thus, it is used to determine β angle interval. Torque ripple values are calculated by using (6.4) when the current angle is 60 and 75 degrees. These results are given in Figs 6.3 and 6.4, repectively. According to these results, lower and upper bounds of β are chosen as 4 and 8 degrees, respectively.

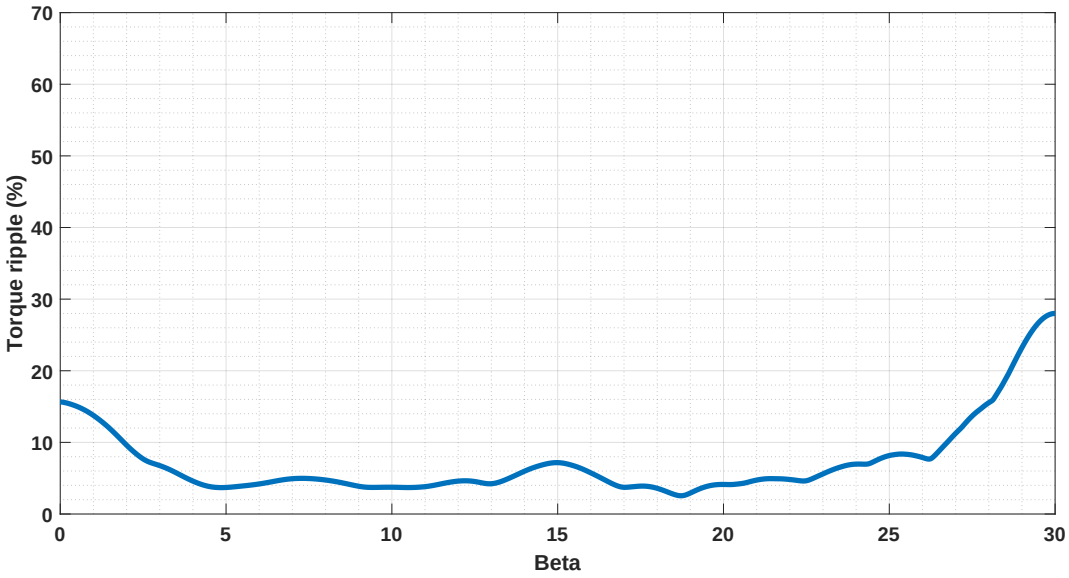

Figure 6.3: Torque ripple vs β when current angle α is 60 deg.

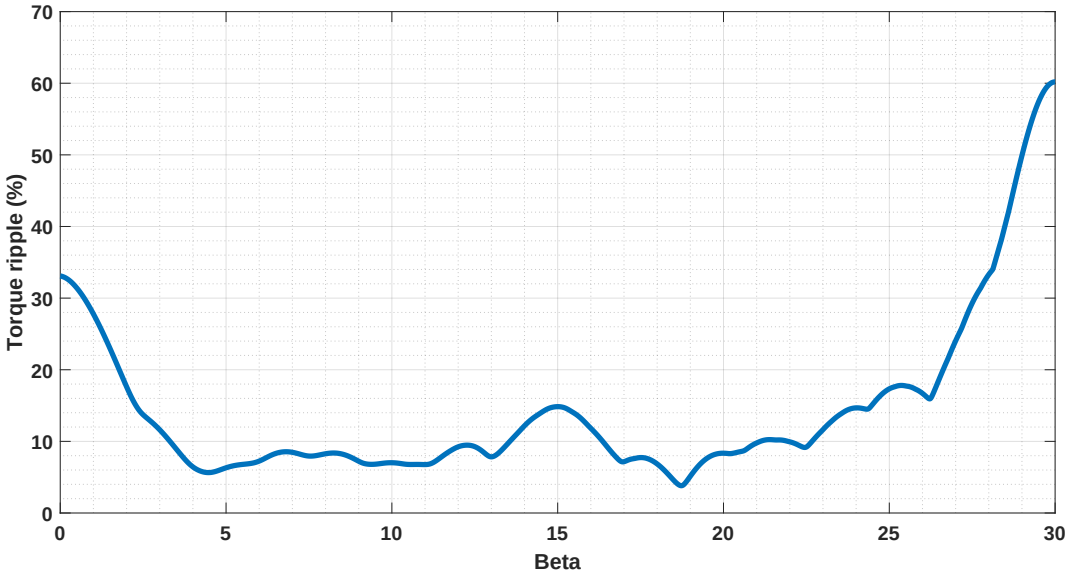

Figure 6.4: Torque ripple vs β when current angle α is 75 deg.

6.1.3 Sensitivity Analysis for k_b

Flux barrier distribution constant k_b does not have an effect on average torque and torque ripple individually. However, it determines the geometrical dimensions of the

machine. It affects the width distribution of flux barriers. Thus, sensitivity analysis is performed by observing geometrical restrictions. This is performed by observing the outer flux barrier's width through d-axis, which is represented by W_{42} for this case, and it is calculated as in (6.5).

$$W_{42} = \frac{k_b^3(R_r - R_{shaft})}{1 + k_b + k_b^2 + k_b^3} \frac{k_{wq}}{1 + k_{wq}} \frac{k_{wd}}{k_{wq}} \tag{6.5}$$

For this purpose, other parameters are chosen as their usual values that is k_{wq} is taken as 0.9 since it is chosen as in previous section, k_{wd} is chosen as $0.6k_{wq}$ which is 0.54, and $R_r - R_{shaft}$ is taken as $30\ mm$.

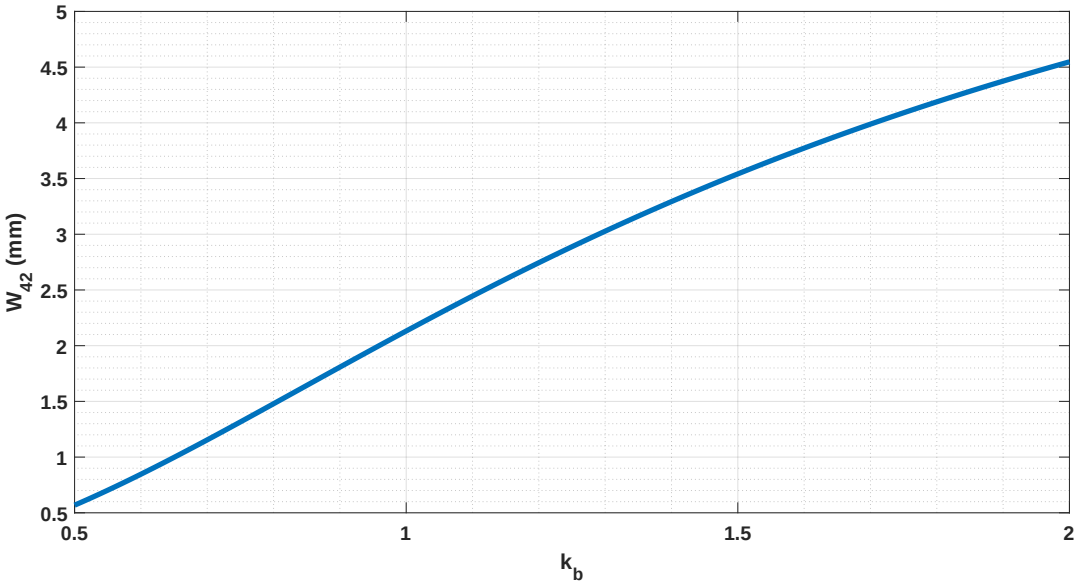

Figure 6.5: Change of outer flux barrier thickness with k_b

Based on the results given in Fig. 6.5, the lower limit for k_b is chosen as 0.8 to make sure that the outer flux barrier is thicker than $1.5\ mm$, and the upper limit is chosen as 1 since it is not desired that the outer flux barrier to be thicker than inner flux barriers due to the mechanical robustness constraint.

6.2 Optimization Methodology

Genetic algorithm is selected as an optimization methodology, and GA toolbox of MATLAB is used. Due to the multiple numbers of the objective function, 'gamultobj' function in MATLAB is used.
. Only crossing-over ratio and mutation ratio are changed and default values for rest of the options are used. Optimization is performed two times: one is without mutation, and one is with mutation as crossing-over ratio and mutation ratio are given in Table 6.1.

	Crossing-over ratio	Mutation ratio
1^{st} trial	0.7	0
2^{nd} trial	0.7	0.03

Table 6.1: Optimization parameters

On the other hand, population and generation numbers are important optimization parameters. The population number is chosen as 100 and the generation number as 16. Thus, the function is called 1600 times. This is enough in order to get good results. As indicated before, 12 simulations should be performed for each design, and it concludes with 19200 simulations in total. For an initial generation, each simulation takes 2 minutes and the total simulation time for the optimization process is 26.66 days. However, 12-core CPU is used, and 12 simulations can be performed parallel. Thus, the total simulation time for a whole optimization process is about 2.22 days. However, after the first generation is completed, simulation time increases gradually, and the whole optimization process takes about 7 days. This problem can be solved by deleting each simulation result after a generation is completed. By doing this, the total time can be fixed around 2.22 days. This is 3.63 days for parametric sweep.

The performance indices to be optimized are the maximum power at maximum speed that is 12000 rpm and the sum of torque ripples when the current angle α is 60 deg. and 75 deg. Other potential objectives to be optimized can be mass, total cost, and efficiency of the machine. Optimized parameters are k_{wq}, k_{wd} and k_b. Their limits are calculated in the sensitivity analysis section.

All results are given in Pareto-front in Fig. 6.6 for the case without mutation and in Fig. 6.7 for the case with mutation. The x-axis of the Pareto-front is taken as the negative maximum power output at maximum speed since power at maximum speed is tried to be maximized, and minimizing negative power at maximum speed is the same.

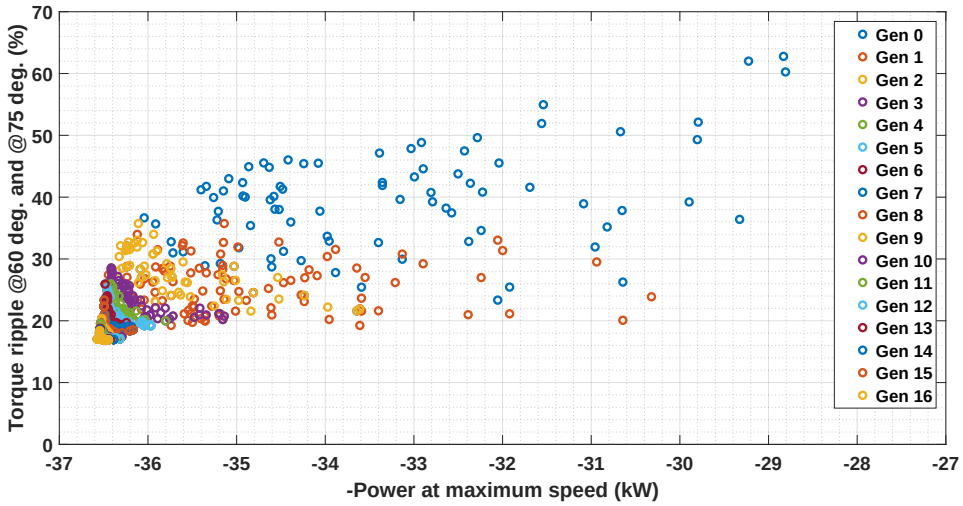

Figure 6.6: Optimization results without mutation: Total of 60 deg. and 75 deg. torque ripple vs negative of the power at 12000 rpm

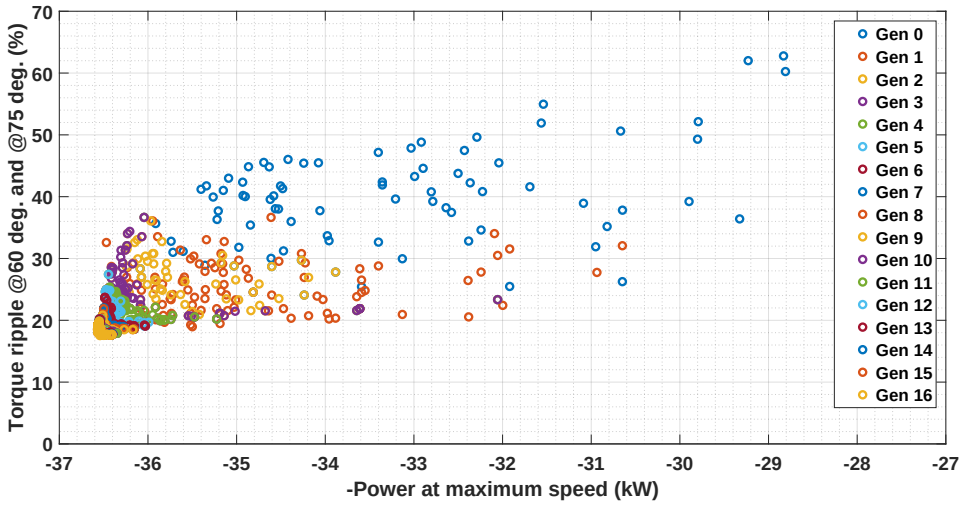

Figure 6.7: Optimization results with mutation: Total of 60 deg. and 75 deg. torque ripple vs negative of the power at 12000 rpm

When the results from Chapter 4 and optimization are compared, optimization results are slightly worse. The reason is that k_{wq} is chosen as 0.9. In parametric sweep, this value is obtained as 0.95 after eliminations. Power at the maximum speed of good design, which is obtained in parametric sweep, is $37.05\ kW$ while this value is around $36.54\ kW$ for GA optimization result. The difference is around $500\ W$. This can be solved by changing k_{wq} value for the optimization process. After k_{wq} value is arranged, optimization results can get or at least closer parametric sweep results.

6.2.1 Design Selection

After the Pareto front is obtained, one can select a design by comparing different objectives and how much one objective is penalized when the other is improved. So, the human decision comes after the optimization process [26]. The design with the highest power and lower total ripple is elected from the Pareto front. Selected design is presented in Fig. 6.8. Parameters of this design are given in Table 6.2. Power at maximum speed is $36.57\ kW$, and total torque ripple is 17.96%.

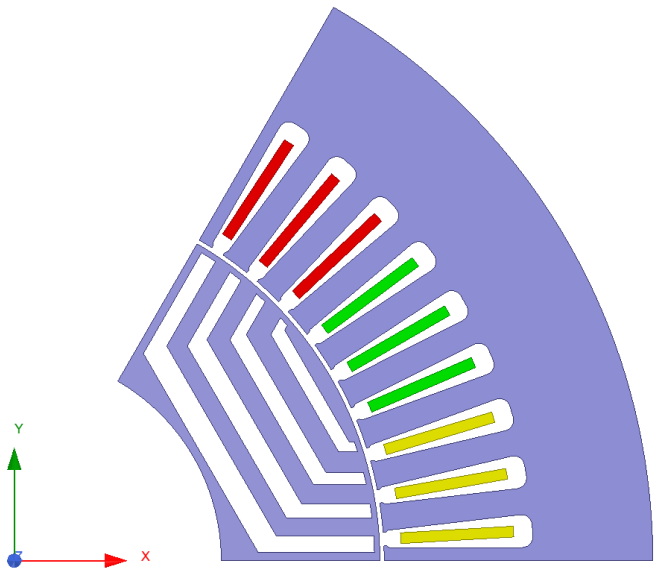

Figure 6.8: FEA view of the selected design

Torque-speed characteristic, power-speed characteristic, current-speed characteristic,

Parameter	Value
k_{wd}	0.6193
k_b	0.8396
β	6.9023
Power at max. speed (kW)	36.57
Total torque ripple ($\%$)	17.96

Table 6.2: Parameters and results of the selected design

and current angle-speed characteristic of the selected design are given in Fig. 6.9. These results are obtained by fixing the maximum torque of the selected design to $250\ N.m$. Maximum torque of the machine is $300.86\ N.m$ when its axial length is $200\ mm$, sot its axial length is set to $166.2\ mm$ and maximum torque is reduced to $250\ N.m$. According to these results, the base speed of the machine is 4186 rpm. Moreover, the maximum power for the machine is $113.91\ kW$, phase current decreases around $140\ A$ peak at 12000 rpm, and the current angle increases around 82 degree at 12000 rpm.

6.2.2 PM Addition to Selected Design

In order to improve machine performance, PMs are added into the flux barriers. In this case, ferrite PM is added to flux barriers through q-axis fully and additional PMs to flux barriers sides as in 6.10. Again results are obtained by fixing the maximum torque of the machine to $250\ N.m$, and they are given in Fig. 6.11. Maximum torque of the machine is $319.56\ N.m$ and when it is fixed to $250\ N.m$, its axial length is $156.46\ mm$. In Table 6.3, mass and cost result of the machine is given. Power at the maximum speed of the machine is $87.64\ kW$. This value is approximately equal to the power at the machine's maximum speed, which is obtained in parametric sweep and called good design with PM assistance. When two designs are compared, the total mass of the optimized machine is less since its k_{wq} value is smaller and the cross sectional area for PM is smaller. Thus, the cost of the optimized machine is smaller as well. On the other hand, it is better to optimize k_{wq} value. This may cause an increase in the computation time, but results could be improved.

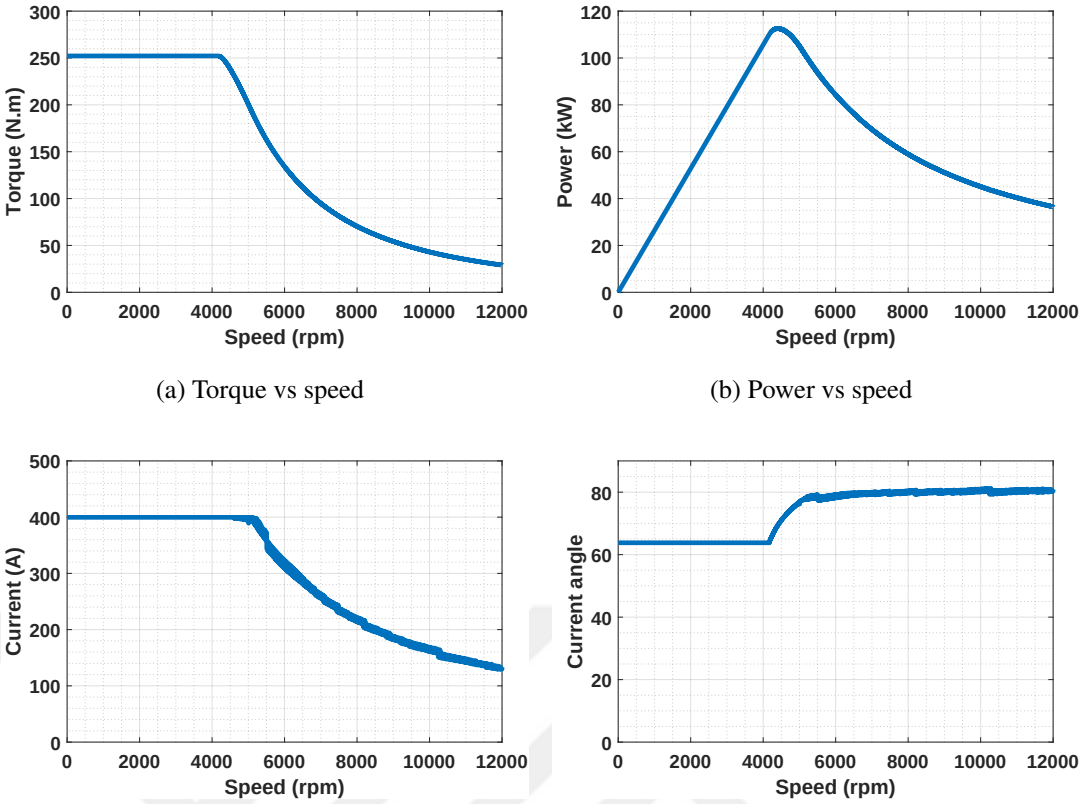

(a) Torque vs speed

(b) Power vs speed

(c) Current vs speed

(d) Current angle vs speed

Figure 6.9: Results for optimized design

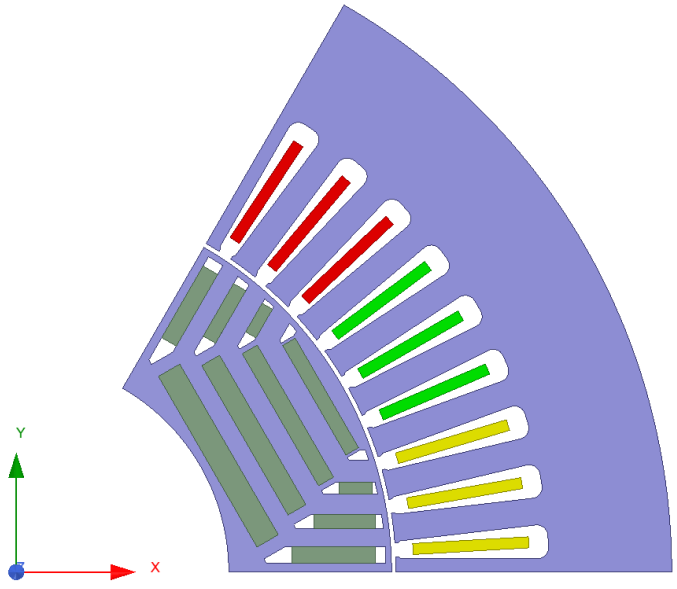

Figure 6.10: FEA view of the selected design with PM assited

On the other hand, if k_{wq} is chosen as 0.95, machine performance can be increased. When it is done, power at maximum speed increases without ribs. Actually, it contributes to an increase in machine performance but magnet mass too.

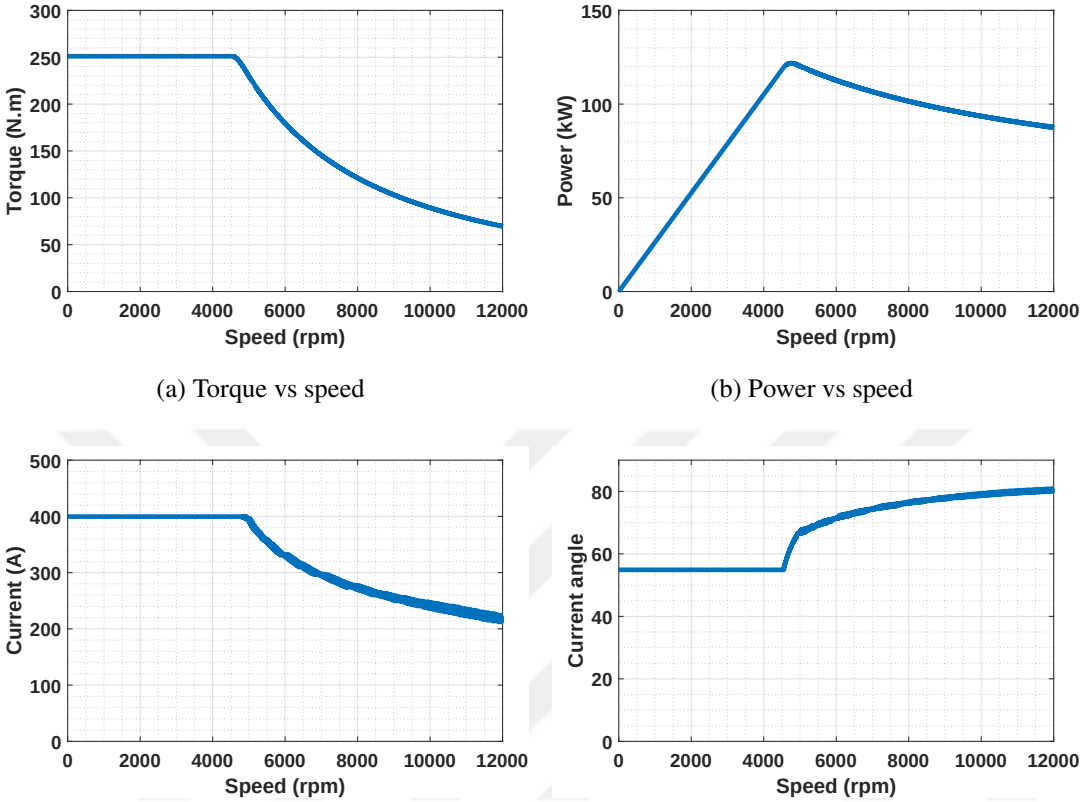

(a) Torque vs speed

(b) Power vs speed

(c) Current vs speed

(d) Current angle vs speed

Figure 6.11: Results for optimized design with ferrite PM assistance

6.3 Discussion

In this chapter, firstly, sensitivity analysis for rotor parameters is performed. Then, lower and upper limits are determined for each parameter. These results show that it is not necessary to optimize k_{wq}. However, after optimization results are gathered, it is observed that k_{wq} should be optimized. It affects power at maximum speed and the amount of PM which is added to flux barriers.

As an optimization algorithm, the genetic algorithm is chosen, and the optimization

Parameter	Value
P_{12000} (kW)	87.64
Base speed (rpm)	4560
Magnet volume (cm^3)	93.513
Magnet mass (kg)	2.75
Magnet cost ($)	31.625

Table 6.3: Properties of optimized machine with ferrite PM assisted

problem includes two objective functions. The first one is to minimize torque ripple when the current angle α is 60 and 75 degrees. The second one is to maximize power output at $12000\ rpm$. Thus, a multi-objective genetic algorithm is used. Moreover, by the curve fitting method, a machine's power-speed, torque-speed, current-speed, and current angle-speed characteristics can be obtained. Thus, possible objectives of the optimization are power factor, efficiency, maximum torque, and total volume of the machine. Optimization is performed two times. Firstly, optimization is run without mutation. Secondly, it is run with mutation. Then, it is observed that result of optimization without mutation is better. The optimization without mutation converged more rapidly to better designs. This situation illustrates that the optimization problem does not have any local minima or local maxima.

When results of parametric sweep and optimization are compared, it is observed that the results of parametric sweep are a little better. The reason for the difference is that k_{wq} values are different. In grid search, it is found as 0.95, while it is fixed to 0.90 for optimization. Results of the optimization can be improved by fixing k_{wq} to 0.95 or also defining it as a variable.

CHAPTER 7

EXPERIMENTAL RESULTS FOR A PROTOTYPE MACHINE

7.1 Introduction

A synchronous reluctance machine is designed by parametric sweep and optimization. The design process includes curve fitting of FEA results at some points. Then, obtained results are validated by using FEA. Moreover, it should be validated experimentally. Power rating of the selected designs is around $100\ kW$ and current density is $15\ A/mm^2$. Therefore, it is hard to realize and measure this machine. Thus, $10\ kW$ prototype machine is designed for experimental validation. This machine is not optimized, and it is designed by only using the parametric sweep method. Moreover, the stator of the prototype is not designed, and an IM's stator is used. Properties of this machine are given in Table 7.1.

Table 7.1: Properties of prototype machine

Parameter	Value
Pole number	4
Slot number	36
Barrier number	3
Frequency (Hz)	50
Speed (rpm)	1500
Air gap (mm)	0.35
Rotor radius (mm)	64.65

7.2 Design of the Prototype Machine

The rotor of the prototype machine is designed by using Model 1: flux barrier distribution with respect to barrier distribution constant. Flux barrier distribution constant is chosen as 1 for ease of manufacturing. This machine is designed in 1500 rpm as rated speed and 6000 rpm as maximum speed.

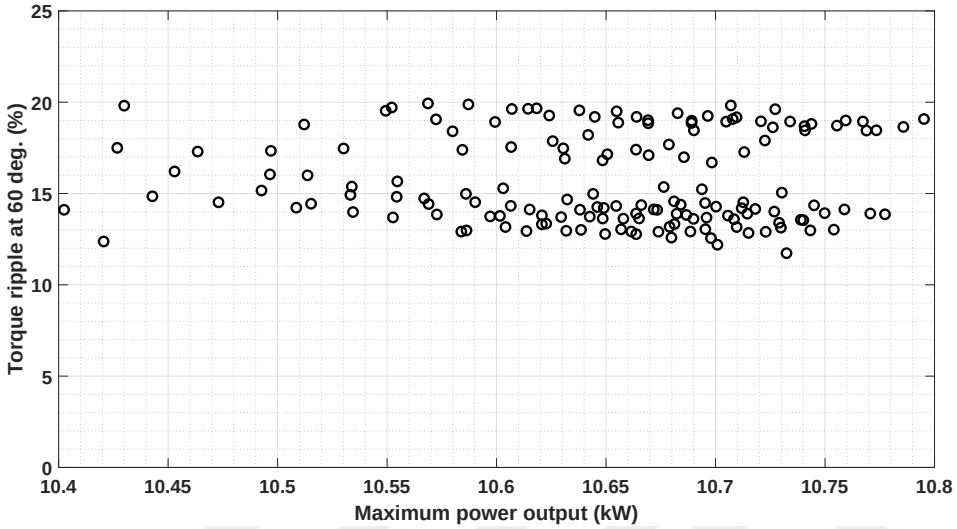

Figure 7.1: FEA view of the prototype machine

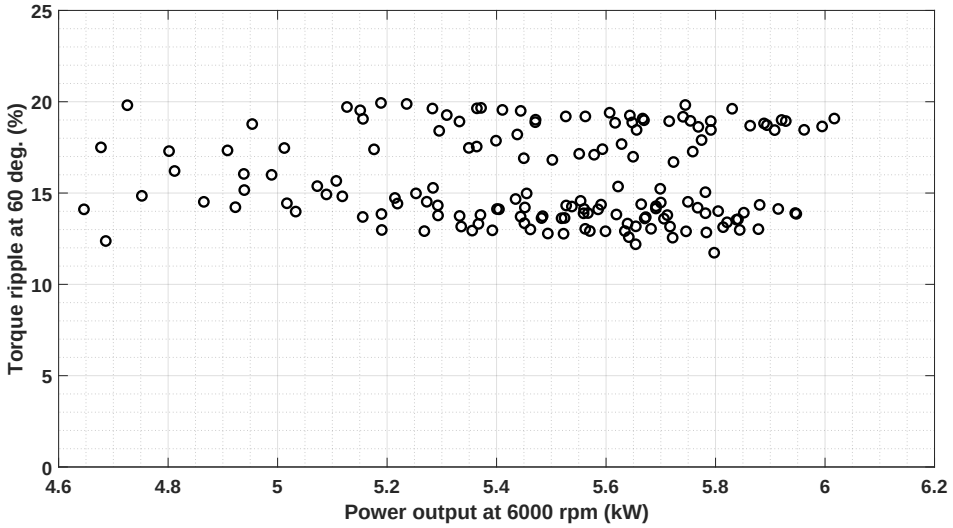

Figure 7.2: FEA view of the prototype machine

Results for this machine is given in Figs. 7.1, 7.2 and 7.3, respectively. the ripple of the machine varies between 12 and 20%. Moreover maksimum power of the ma-

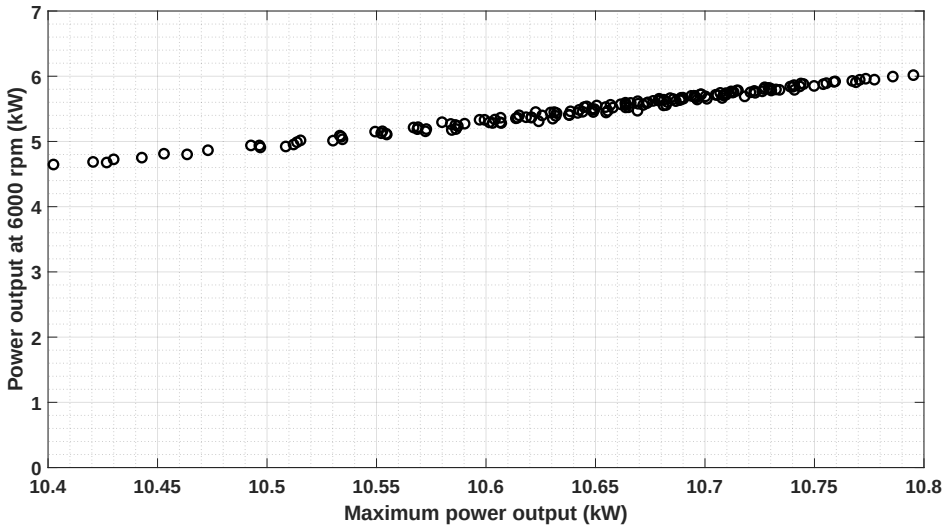

Figure 7.3: FEA view of the prototype machine

chine is approximately for each machine since maximum torque of the machine is fixed to $57.5\ N.m$ by arranging axial length of the machine. Furthermore, the power of the machine at maximum speed varies between 4.6 and $6\ kW$. This machine is given in Figs. 7.4 and 7.5, and resultant properties are given in Table 7.2. In this machine, ribs are placed through q-axis since PMs are not planned to be added to this machine. Moreover, the thickness of ribs is equal to each other, and 0.7 mm since it is driven at $6000\ rpm$ as a high speed. Mechanical stress results are given in Fig. 7.6 when machine is rotating with 6000 rpm. As can be seen in this Figure, machine is mechanically well-designed.

Table 7.2: Resultant properties of the prototype machine

Parameter	Value
k_{wq}	0.66
k_{wd}	0.6
$k\beta$	2
Torqu ripple @ 60 deg. (%)	13.04
Max. power output (kW)	10.07
Power output @6000 rpm (kW)	5.69

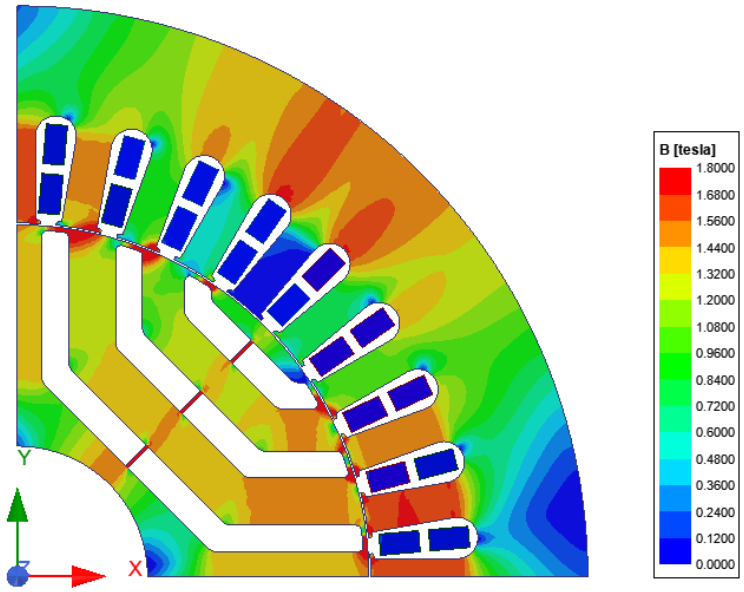

Figure 7.4: FEA view of the prototype machine at 1500 rpm

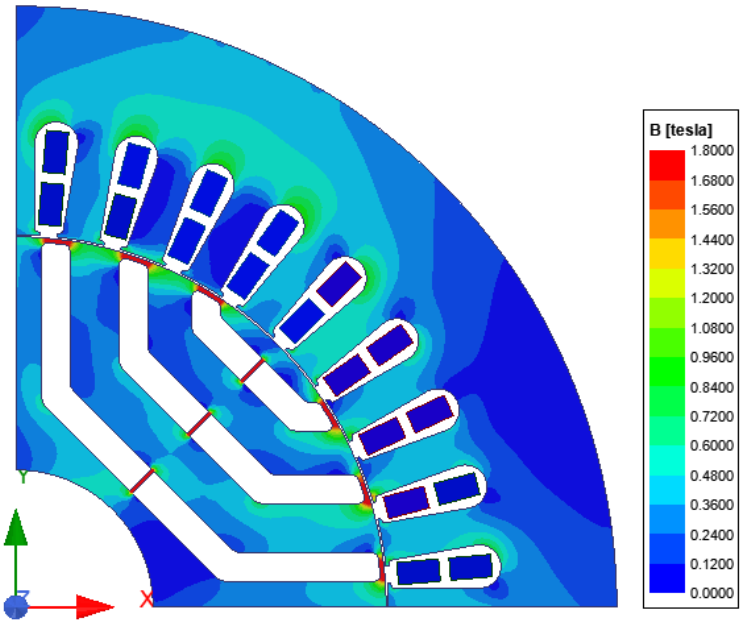

Figure 7.5: FEA view of the prototype machine at 6000 rpm

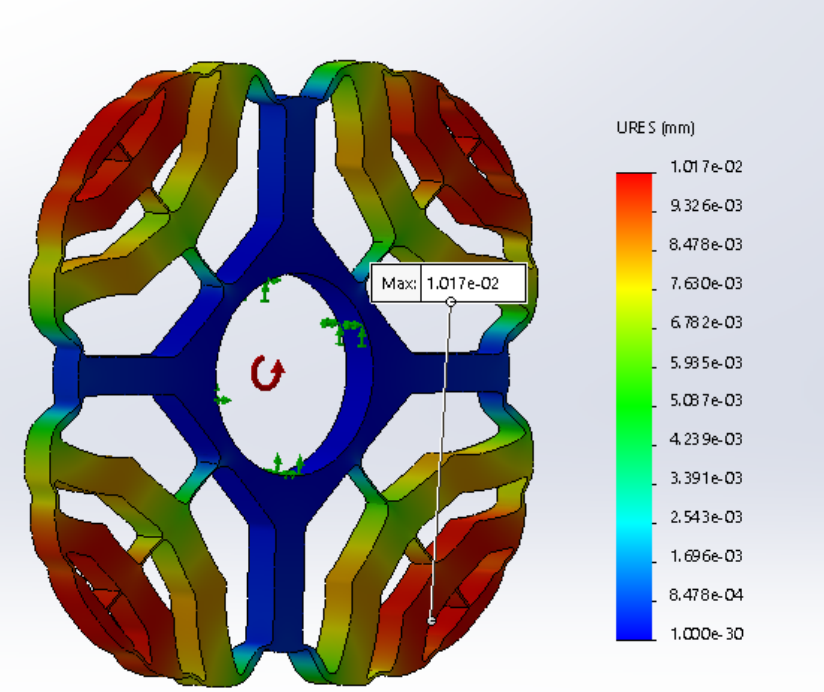

6000 rpm displacement

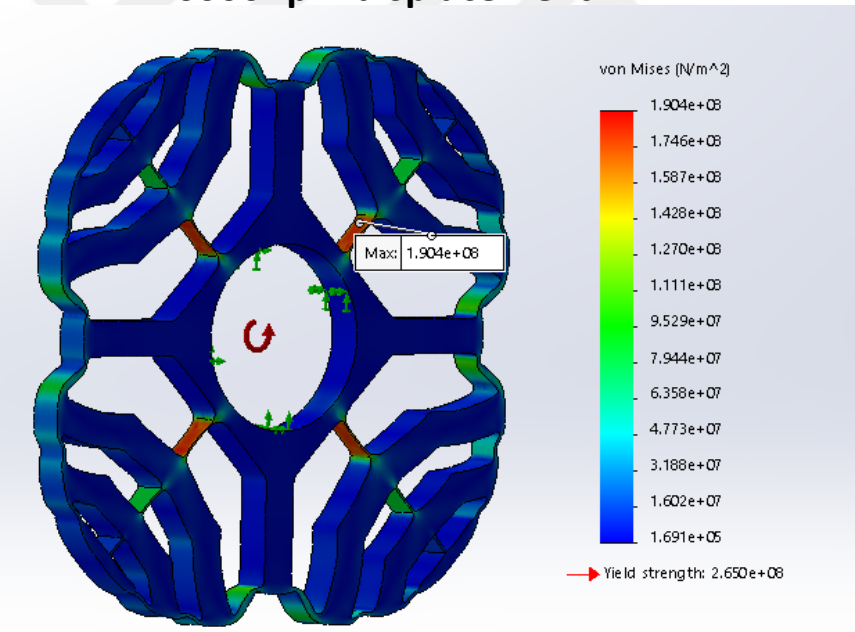

6000 rpm stress

Figure 7.6: Mechanical stress results for the prototype machine at 6000 rpm

7.3 Manufacturing of the Prototype Machine

A prototype machine, whose overall parameters are given in Table 7.1, is manufactured for the experimental verification. The manufacturing process starts with the manufacturing of the stator. As mentioned above, the selected stator is used in mass produced IM manufacturing. Thus, producing company uses a press printing machine for the mass production of the stator. Manufactured stator is shown in Fig. 7.7. Moreover, the winding of the machine is also produced using traditional manufacturing methods.

(a) (b)

Figure 7.7: Manufactured stator

The rotor is manufactured by using laser cut if it has to be mass-produced, press printing machine can be used. In Fig. 7.8, the tolerance values, which are obtained after the manufacturing, are shown. As can be seen, tolerance values are minimal. Tangential bridges are cut thicker than the values that are obtained in the design process. This difference is corrected after the turning process.

A manufactured rotor lamination can be seen in Fig. 7.9. These motor laminations are placed with a 10-degree continuous skew from one end to the other end in order to decrease the torque ripple of the machine. It also decreases the average torque of the machine. Then, these laminations are compressed with aluminum sheets from two

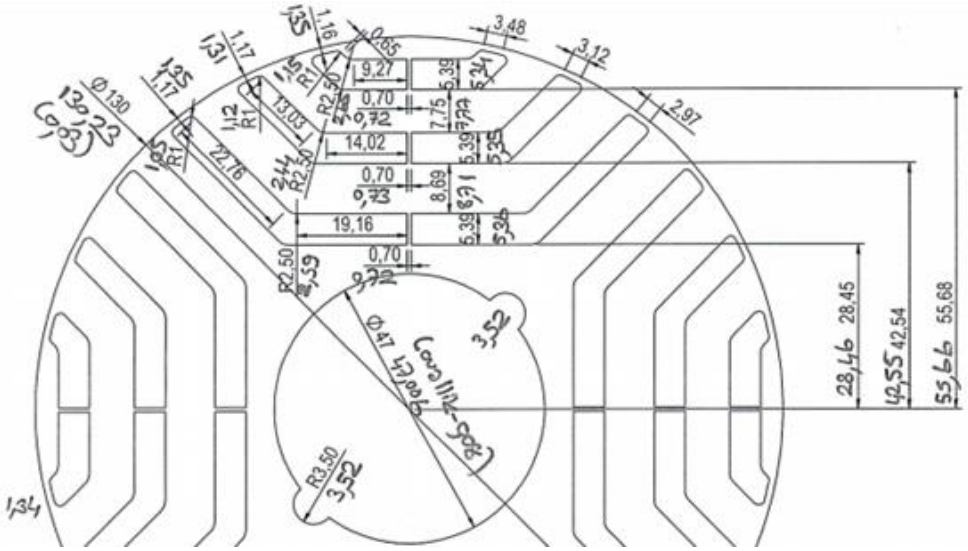

Figure 7.8: Rotor production tolerances

ends. The final version of the rotor is given in Fig. 7.10.

Figure 7.9: A manufactured rotor lamination

Figure 7.10: A manufactured rotor lamination

Finally, all parts of the machine are shown in Fig. 7.10.

Figure 7.11: All parts of the machine

7.4 Comparison of Experimental and FEA Results

Experimental results of the machine are obtained when mechanical speed is 1500 rpm. In the experiment setup, the sensorless driver is used. The driver gets output power

knowledge of the machine, and it arranges current and current angle values. Then, it gives the efficiency, power factor, and current values as an output. Experiment is performed for three output power values which are 7.5, 8.5 and 10 kW and results are given in Table 7.3. Moreover, torque-speed characteristic, power-speed characteristic, current-speed characteristic, current angle-speed characteristic and power factor-speed characteristic are given in Figs. 7.12 and 7.13

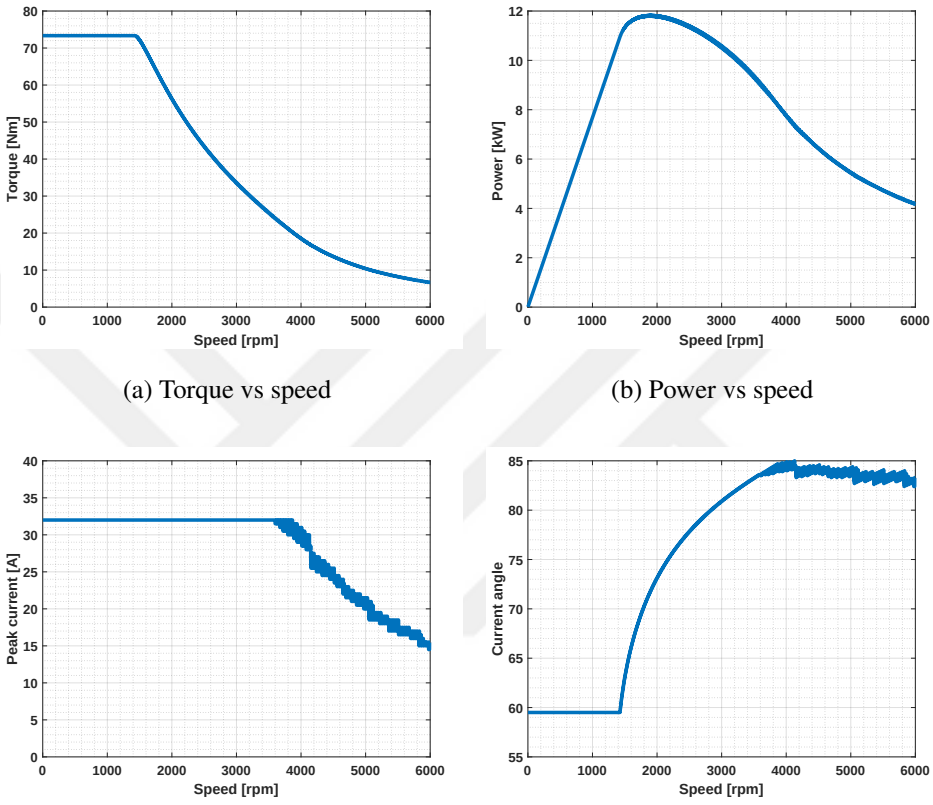

(a) Torque vs speed

(b) Power vs speed

(c) Phase current vs speed

(d) Current angle vs speed

Figure 7.12: Results of manufactured machine (Current limit is 32 A)

Then, the machine is operated for 3 hours. At the beginning of the operation, the temperature in stator and winding region of the machine is measured as 16.5 degrees. After that, experimental measurements are made again, and results are given in Table 7.4. The final temperature of machines is not high, and these values are reasonable.

The design procedure is updated to get results for a specific output power by using curve fitting with 12 FEA results. Moreover, the rated speed of the machine is set to 1500 rpm. Thus, speed and power rating are taken as input and phase current,

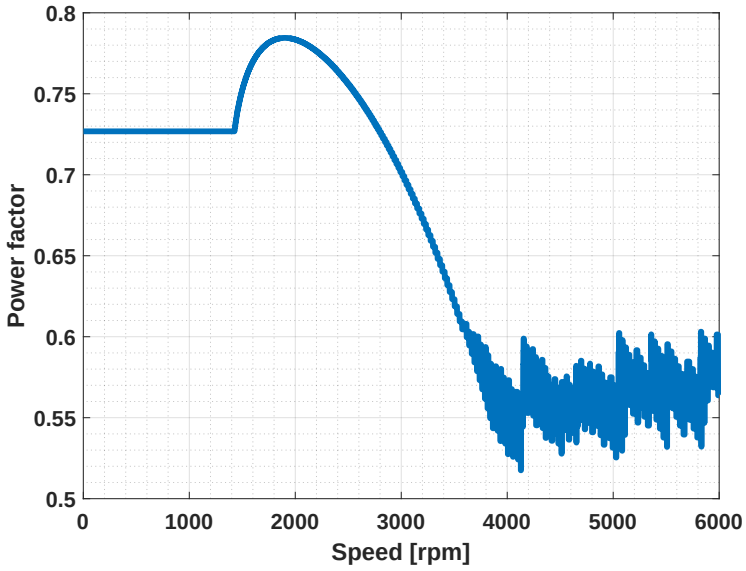

Figure 7.13: Power factor results for manufactured machine

Table 7.3: Experimental results for 10 kW prototype machine with cold rotor

Output power (W)	7587	8561	10116
Input power (W)	8022	9111	10736
Efficiency ($\%$)	94.57	93.96	94.22
Average current (A_{rms})	17.86	19.7	22.49
Power factor	0.67	0.66	0.69

current angle, power factor, and efficiency are taken as output. Results are given in Table 7.5. The output power of the machine is found close to experimental results for three cases. However, input power has a difference. The reason may be caused by the nonlinear nature of losses. In the curve fitting process, the iron loss is determined. Copper loss is calculated by using the measured resistance value. The reason for the difference in output results is the difference in calculated losses. The difference is small, and its reason can be an error in resistance measurement. Moreover, another reason can be the difference between material properties in FEA and experiment. The same reasons may cause a difference in other values, such as power factor and average current. Moreover, torque ripple is not measured experimentally. However, any noise and compulsion did not occur during the tests.

Table 7.4: Experimental results for 10 kW prototype machine after machine is operated for 3 hours

Output power (W)	7524	8545	10116
Input power (W)	8004	9114	10850
Efficiency ($\%$)	94	93.76	93.23
Average current (A_{rms})	17.79	19.58	22.52
Power factor	0.65	0.67	0.69
Final temperature (C°)	26.6	26.7	29

Table 7.5: Results obtained with curve fitting applied to FEA results

Output power (W)	7599	8560	10113
Input power (W)	8116	9138	10793
Efficiency ($\%$)	93.62	93.67	93.69
Average current (A_{rms})	17.50	19.26	22.03
Power factor	0.653	0.643	0.664

Efficiency map of the machine is gathered by using FEA, and presented in Fig. 7.14. According to this Figure, machine efficiency is around 0.94 for high-speed performance.

In Fig. 7.15, IEC efficiency classes are given. IEC efficiency class is a function of the machine's rated power and speed. When the machine output power is $7500\ Watt$, and rated speed is 1500 rpm, the lower limit for IE4 is 92.6%. Moreover, this value is 93.3% when the machine's output power is $11000\ Watt$. Thus, prototype machine is IE4 for 7500, 8500 and $10000\ Watts$. Even the machine is close to being IE5 standard which is not given in Fig. 7.15.

7.5 Comparison of 7.5 kW SynRM and IM

SynRMs have advantages over IM in many ways, such as efficiency and cost. Since there is not copper loss in SynRM rotor, its efficiency is better than IMs. In this sec-

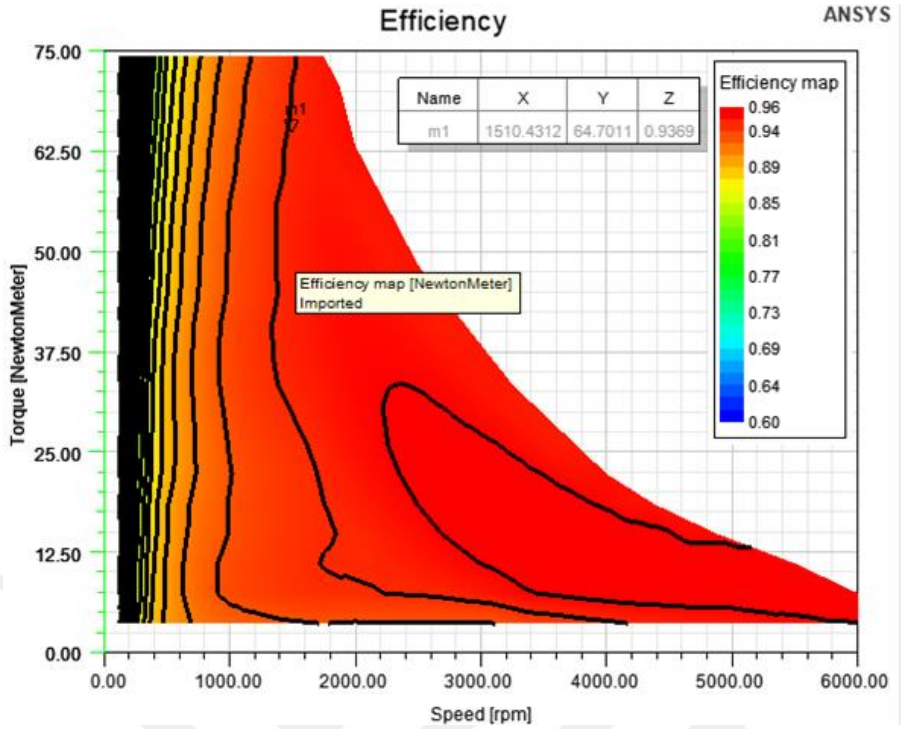

Figure 7.14: Efficiency map of the machine

tion, a comparison of 10 kW prototype machine and IM machine which is produced by the same manufacturer. For comparison, machines are driven as output power is $7.5\ kW$ since this is one of the standard power ratings in the industry. Results for SynRM and IM are given in Table 7.6. As expected, the efficiency of SynRM is better than IM. However, the power factor of SynRM is lower than IM's since PMS are not inserted into SynRM. As can be shown in previous sections, if PM is inserted into SynRM, efficiency is not affected significantly, but the power factor increases and gets close to IM's power factor. Moreover, power factor of SynRM given in Table 7.6 is lower than common power factor of SynRMS since this SynRM is designed for $10\ kW$ and machine is not enough saturated for $7.5\ kW$. Thus, machine is operating at lower current angle and power factor is low. Furthermore, it can be corrected by arranging turn number of the machine and this value may rise over 0.7. This value is accaptable value for SynRM without PMs.

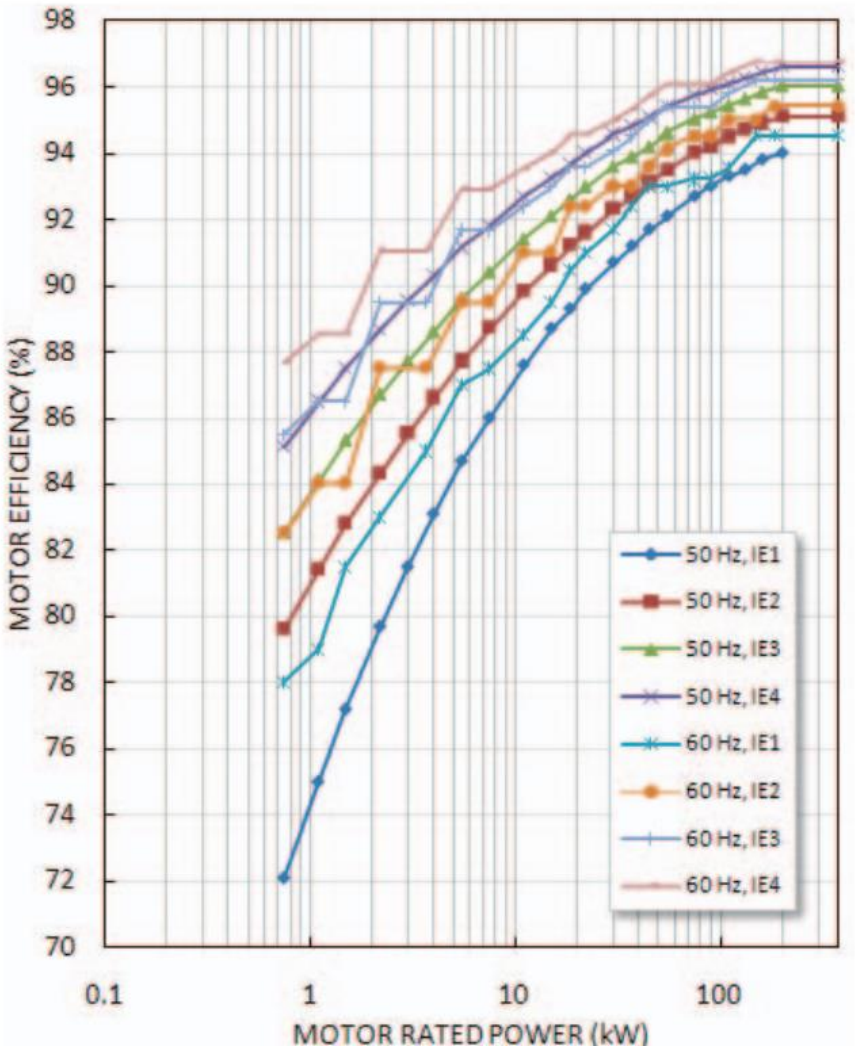

Figure 7.15: IEC efficiency standarts for 4-pole machine for 50 Hz. and 60 Hz. [60]

Table 7.6: Comparison of SynRM and IM

	SynRM	IM
Output power (W)	7587	7502
Input power (W)	8022	8301
Efficiency ($\%$)	94.57	90.4
Average current (A_{rms})	17.86	14.74
Power factor	0.67	0.81

CHAPTER 8

CONCLUSIONS AND FUTURE WORKS

The influence of the rotor design on the high speed performance of SynRMs that is their power-speed characteristics beyond the base speed is analysed in this thesis. A systematical design procedure that includes multi-level evaluations and eliminations with the help of a reduced number FEA simulations is developed for this purposes.

One of the most crucial design steps is the design and parametrization of the rotor geometry. The rotor model must give enough flexibilty to get good designs but have a minimum number or parameters so that the design process can be conducted with less computational effort. Firstly, flux barrier shape is selected as a U-shaped flux barrier. This shape has advantages such as ease of parameterization and having a chance to add rectangular PMs. Secondly, a parametrized rotor geometry model that is defined with four variables for any number flux barriers is constructed. These variables can be summurized as follows:

- Constant rotor slot pitch except for the outer most iron bridge is assumed, and each flux barrier is separated by α_m. β is used to determine the position of the outer iron bridge, and α_m is determined with respect to β, pole numbers, and flux barrier numbers.

- In order to determine total iron and air amount in the d- and q-axises, two parameters are used: k_{wq} and k_{wd}.

- Moreover, distribution of the iron bridge thickness is performed by using k_i, and distribution of flux barrier thickness by using k_b. To create a rotor geometry only one of these parameters can be used.

Moreover, rotor geometry creation is realized in three different ways: by distributing irons to the iron bridges, by distributing airs to the flux barriers, and by fixing the width of the outer iron bridge and distributing airs to the flux barriers. When the outer bridge is fixed to a value, its width can be decreased. Thus, leakage flux through this iron bridge is decreased, and machine performance increases. Finally, ribs are added to the rotor since the rotor should be mechanical roboust at high speeds. Mechanical stress on the rotor increases with the mechanical speed of the machine. Ribs give mechanical strength to the rotor, and they should be designed with respect to the highest speed value of the machine. However, they decrease the machine performance, so they should not be over-designed.

A $100\ kW$ SynRM with $12000\ rpm$ maximum speed is designed. Firstly, machine parameters such as pole number, flux barrier number, and DC-link voltage of the driver are selected. Then, machine sizing for stator and rotor is performed. MMF for each slot is determined by considering the average torque per current of the machine. This value is linear at first, but it saturates as the MMF value increase. MMF selection is made after saturation occurs since the machine is wanted to be a little saturated such that the machine generates maximum torque at $60 - 65$ degrees of current angle. For the application, fill factor, and current density are determined. By using these values, a slot design is made. Slot area, height, and width are calculated. The next step is to determine the turn number of the machine. This is performed by iterating turn numbers and comparing their effects on the high-speed performance of the machine. By using driver properties and MMF limitation, the current limitation is determined. Then, candidate designs that have the same stator but different rotor are created by parametric sweep. These designs are eliminated with respect to geometric restrictions and torque ripple results when the current angle is 60 and 75 degrees. For the remaining designs, power-speed, torque-speed, current-speed, and current angle-speed characteristics are obtained. The characteristic line of each candidate design is estimated by using the d- and q axis flux linkage maps that are obtained by applying cure fitting of only 12 FEA simulations. Curve fitting is performed by using 'fit' function of MATLAB. Then, all results are obtained. When they are examined, it is observed that the maximum power of the machine at maximum speed varies between 22.5 and $37.5\ kW$. This proves that the high-speed performance of the machine can

be improved by designing the rotor well.

Since none of the SynRM design could reach a high enough power at the maximum speed, PMaSynRM versions of two selected SynRMS, from which one has a better high-speed performance, are designed. The design process is performed by using two types of PM: ferrite PM and NdFeB PM. The effects of adding different amount and type of PMs on the high-speed performance and cost of machines are compared. The designs could reach more than $80\ kW$ output power at maximum speed when 50% of the straight parts of flux barriers is filled by NdFeB magnets or the whole available space including the sides of the flux barriers is be filled by ferrite magnets. Both designs have better high-speed performance, but NdFeB assited SynRMs are found to have a much higher cost than ferrite assisted SynRMs. Moreover, it is observed that the PM assisted versions of the SynRM with the better high speed performance could reach higher outputs power values with the same amount of PMs. So, it can be concluded that it is a valid approach to first design SynRM and then determine the required PM amount.

Optimization is performed for the parameterized rotor in Chapter 6. As discussed before, the rotor is designed by using four parameters. As a first step, sensitivity analysis for these four parameters is conducted. After that, upper and lower limits are gathered for three parameters which are k_{wd}, k_b, and β. However, it is observed that there is no need to optimize k_{wq}. Thus, optimization is performed for three parameters, and k_{wq} is fixed to 0.9. As an optimization algorithm, a genetic algorithm is used. Objective functions are selected as the power of the machine at maximum speed and torque ripple of the machine. Thus, it is multi-objective optimization problem. For optimization, 'gamultobj' toolbox of MATLAB is used. It takes about seven days. By improving methodology, it can be decreased to 2.22 days. Parametric sweep takes 3.54 days. Computational time of optimization is less and by doing some improvements, results can be better as well. Thus, using optimization method is a good choice due to less computational time and better results.

Finally, the design procedure is validated by experimental tests. A prototype SynRM with a power rating between 7.5 and 10 kW is designed and tested. For this purpose, a stator of an existing IM is used, and only the rotor is designed by using the parametric

sweep based method. The machine is tested at 7.5, 8.5, and 10 kW, where power factor, phase current, and efficiency measurements are conducted. These results are compared to analysis results, and it is observed that both results are close to each other. This shows the validity of the proposed design method and also the analysis models used in this study.

8.1 Future Work

In this thesis, PM assisted SynRM with a wide speed range is designed. The rotor of the machine is parameterized. Then, by using parametric sweep, a 100 kW machine is designed. Moreover, optimization is performed for these parameters. The following improvements can be made in the design and optimization processes:

- The stator can be parametric. Slot width, height, and area can be parameterized. Moreover, slot opening angle and height have an effect on torque ripple. These values can be parametric as well. Thus, the number of candidate designs is increased, but the simulation number can be decreased by arranging torque ripple limitations.
- In this thesis, integer slot number per phase per pole is selected. Instead of this, a fractional slot per phase per pole can be selected in order to minimize torque ripple. This winding diagram can be integrated into the design process, which is presented in this paper.
- In this thesis, a genetic algorithm is used. As future work, another optimization algorithm such as particular swarm and differential evolution can be adapted.
- Driver side of the machine can be designed and the torque ripple of the machine can be decreased by using drive methodologies.
- In this thesis, mechanical and electromagnetic design is performed. The efficiency of the machine can be increased by considering thermal analysis. Thus, the efficiency class of the machine can be improved.
- In this thesis, SynRM is designed with 6 poles. As future work, SynRM with

higher pole numbers can be designed by observing mechanical and electromagnetic concerns.

REFERENCES

[1] N. Bianchi, E. Fornasiero, and W. Soong, "Selection of pm flux linkage for maximum low-speed torque rating in a pm-assisted synchronous reluctance machine," *IEEE Transactions on Industry Applications*, vol. 51, no. 5, pp. 3600–3608, 2015.

[2] J. K. Kostko, "Polyphase reaction synchronous motors," *Journal of the American Institute of Electrical Engineers*, vol. 42, no. 11, pp. 1162–1168, 1923.

[3] N. Ozcelik, U. Dogru, M. Imeryuz, and L. Ergene, "Synchronous reluctance motor vs. induction motor at low-power industrial applications: Design and comparison," *Energies*, vol. 12, p. 2190, 06 2019.

[4] I. Boldea, *Reluctance Synchronous Machines and Drives*. Oxford: Oxford, 1996.

[5] Stratfor, "The geopolitics of rare earth elements," *Stratfor*, 2019.

[6] S. Taghavi and P. Pillay, "A sizing methodology of the synchronous reluctance motor for traction applications," *IEEE Journal of Emerging and Selected Topics in Power Electronics*, vol. 2, no. 2, pp. 329–340, 2014.

[7] R. Rouhani, S. E. Abdollahi, and S. A. Gholamian, "Torque ripple reduction of a synchronous reluctance motor for electric vehicle applications," in *2018 9th Annual Power Electronics, Drives Systems and Technologies Conference (PEDSTC)*, pp. 386–391, 2018.

[8] A. Shrestha, M. Chowdhury, M. Islam, and C. Ross, "Design of pm-assist synchronous reluctance machine for high performance applications," in *2020 IEEE Energy Conversion Congress and Exposition (ECCE)*, pp. 1727–1734, 2020.

[9] S. Tahi, R. Ibtiouen, and M. Bounekhla, "Design optimization of two synchronous reluctance machine structures with maximized torque and power factor," *Progress In Electromagnetics Research B*, vol. 35, pp. 369–387, 01 2011.

[10] S. Dwivedi, S. M. Tripathi, and S. K. Sinha, "Review on control strategies of permanent magnet-assisted synchronous reluctance motor drive," in *2020 International Conference on Power Electronics IoT Applications in Renewable Energy and its Control (PARC)*, pp. 124–128, 2020.

[11] Y. B. Yilmaz and E. Bostanci, "Effects of rotor flux barrier design on torque ripple and high speed performance of synchronous reluctance machines," in *2020 International Conference on Electrical Machines (ICEM)*, vol. 1, pp. 448–454, 2020.

[12] A. Vagati, M. Pastorelli, G. Francheschini, and S. Petrache, "Design of low-torque-ripple synchronous reluctance motors," *IEEE Transactions on Industry Applications*, vol. 34, no. 4, pp. 758–765, 1998.

[13] R.-R. Moghaddam, F. Magnussen, and C. Sadarangani, "Novel rotor design optimization of synchronous reluctance machine for low torque ripple," in *2012 XXth International Conference on Electrical Machines*, pp. 720–724, 2012.

[14] N. Bianchi, S. Bolognani, D. Bon, and M. D. Pre, "Rotor flux-barrier design for torque ripple reduction in synchronous reluctance motors," in *Conference Record of the 2006 IEEE Industry Applications Conference Forty-First IAS Annual Meeting*, vol. 3, pp. 1193–1200, 2006.

[15] T. Mohanarajah, J. Rizk, A. Hellany, M. Nagrial, and A. Klyavlin, "Torque ripple improvement in synchronous reluctance machines," in *2018 2nd International Conference On Electrical Engineering (EECon)*, pp. 44–50, 2018.

[16] C.-H. Hong, H.-c. Liu, H.-S. Seol, H.-W. Jun, and J. Lee, "Decrease torque ripple for synrm using barrier arrangement design," in *2014 17th International Conference on Electrical Machines and Systems (ICEMS)*, pp. 1834–1837, 2014.

[17] N. Bianchi, M. Degano, and E. Fornasiero, "Sensitivity analysis of torque ripple reduction of synchronous reluctance and interior pm motors," in *2013 IEEE Energy Conversion Congress and Exposition*, pp. 1842–1849, 2013.

[18] H. Heidari, A. Rassõlkin, A. Kallaste, T. Vaimann, and E. Andriushchenko, "Vector control of synchronous reluctance motor with reduced torque rip-

ples," in *2020 XI International Conference on Electrical Power Drive Systems (ICEPDS)*, pp. 1–5, 2020.

[19] T. A. Huynh, N.-D. Le, M.-F. Hsieh, and D.-K. Ngo, "A modified of dtc control applied to novel fi- pma-synrm for torque ripple reduction," in *2019 IEEE 4th International Future Energy Electronics Conference (IFEEC)*, pp. 1–7, 2019.

[20] C. Li, G. Wang, G. Zhang, N. Zhao, Y. Gao, and D. Xu, "Torque ripples minimization of sensorless synrm drives for low-speed operation using bi-hfsi scheme," *IEEE Transactions on Industrial Electronics*, vol. 68, no. 7, pp. 5559–5570, 2021.

[21] D. Yan, C. Xia, L. Guo, H. Wang, and T. Shi, "Design and analysis for torque ripple reduction in synchronous reluctance machine," *IEEE Transactions on Magnetics*, vol. 54, no. 11, pp. 1–5, 2018.

[22] G. Bacco and N. Bianchi, "Asymmetric synchronous reluctance rotor geometry design: A practical approach," in *2018 IEEE Energy Conversion Congress and Exposition (ECCE)*, pp. 5414–5421, 2018.

[23] M. Degano, H. Mahmoud, N. Bianchi, and C. Gerada, "Synchronous reluctance machine analytical model optimization and validation through finite element analysis," in *2016 XXII International Conference on Electrical Machines (ICEM)*, pp. 585–591, 2016.

[24] Y. Yamamoto, S. Morimoto, M. Sanada, and Y. Inoue, "Torque ripple reduction using asymmetric flux barriers in synchronous reluctance motor," in *2018 International Power Electronics Conference (IPEC-Niigata 2018 -ECCE Asia)*, pp. 3197–3202, 2018.

[25] T. Hubert, M. Reinlein, A. Kremser, and H.-G. Herzog, "Torque ripple minimization of reluctance synchronous machines by continuous and discrete rotor skewing," in *2015 5th International Electric Drives Production Conference (EDPC)*, pp. 1–7, 2015.

[26] G. Pellegrino and F. Cupertino, "Fea-based multi-objective optimization of ipm motor design including rotor losses," in *2010 IEEE Energy Conversion Congress and Exposition*, pp. 3659–3666, 2010.

[27] L. N. Langue, G. Friedrich, S. Vivier, and K. El Kadri Benkara, "Optimization of synchronous reluctance machines for high power factor," in *2016 XXII International Conference on Electrical Machines (ICEM)*, pp. 1976–1982, 2016.

[28] M. Chowdhury, A. Tesfamicael, M. Islam, and I. Husain, "Design optimization of a synchronous reluctance machine for high-performance applications," *IEEE Transactions on Industry Applications*, vol. 57, no. 5, pp. 4720–4732, 2021.

[29] F. Cupertino, G. Pellegrino, and C. Gerada, "Design of synchronous reluctance motors with multiobjective optimization algorithms," *IEEE Transactions on Industry Applications*, vol. 50, no. 6, pp. 3617–3627, 2014.

[30] F. Cupertino, G. Pellegrino, E. Armando, and C. Gerada, "A syr and ipm machine design methodology assisted by optimization algorithms," in *2012 IEEE Energy Conversion Congress and Exposition (ECCE)*, pp. 3686–3691, 2012.

[31] G. Pellegrino, F. Cupertino, and C. Gerada, "Automatic design of synchronous reluctance motors focusing on barrier shape optimization," *IEEE Transactions on Industry Applications*, vol. 51, no. 2, pp. 1465–1474, 2015.

[32] K. Chen, W. Yu, and C. Wen, "Rotor optimization for synchronous reluctance motors," *CES Transactions on Electrical Machines and Systems*, vol. 3, no. 3, pp. 279–284, 2019.

[33] D. Prieto, A. Fernandez, P. Dessante, J.-C. Vannier, X. Jannot, and J. Saint-Michel, "Optimization methodology for synchronous reluctance motor by finite element method," in *2014 16th European Conference on Power Electronics and Applications*, pp. 1–9, 2014.

[34] M. Šebest, V. Hrabovcová, and P. Makyš, "Optimization of the reluctance synchronous motor with barriers rotor," in *2016 ELEKTRO*, pp. 374–378, 2016.

[35] M. Degano, M. Di Nardo, M. Galea, C. Gerada, and D. Gerada, "Global design optimization strategy of a synchronous reluctance machine for light electric vehicles," in *8th IET International Conference on Power Electronics, Machines and Drives (PEMD 2016)*, pp. 1–5, 2016.

[36] M. Tursini, M. Villani, G. Fabri, A. Credo, F. Parasiliti, and A. Abdelli, "Synchronous reluctance motor: Design, optimization and validation," in *2018 International Symposium on Power Electronics, Electrical Drives, Automation and Motion (SPEEDAM)*, pp. 1297–1302, 2018.

[37] A. Credo, G. Fabri, M. Villani, and M. Popescu, "High speed synchronous reluctance motors for electric vehicles: a focus on rotor mechanical design," in *2019 IEEE International Electric Machines Drives Conference (IEMDC)*, pp. 165–171, 2019.

[38] M. Di Nardo, G. L. Calzo, M. Galea, and C. Gerada, "Structural design optimization of a high speed synchronous reluctance machine," in *2016 XXII International Conference on Electrical Machines (ICEM)*, pp. 2073–2079, 2016.

[39] F. Cupertino, M. Palmieri, and G. Pellegrino, "Design of high-speed synchronous reluctance machines," in *2015 IEEE Energy Conversion Congress and Exposition (ECCE)*, pp. 4828–4834, 2015.

[40] C. Babetto, G. Bacco, and N. Bianchi, "Analytical power limits curves of high-speed synchronous reluctance machines," *IEEE Transactions on Industry Applications*, vol. 55, no. 2, pp. 1342–1350, 2019.

[41] G. Gallicchio, M. Di Nardo, M. Palmieri, A. Marfoli, M. Degano, C. Gerada, and F. Cupertino, "High speed synchronous reluctance machines: Modeling, design and limits," *IEEE Transactions on Energy Conversion*, pp. 1–1, 2021.

[42] E. Castagnaro and N. Bianchi, "High-speed synchronous reluctance motor for electric-spindle application," in *2020 International Conference on Electrical Machines (ICEM)*, vol. 1, pp. 2419–2425, 2020.

[43] C. Babetto, G. Bacco, G. Berardi, and N. Bianchi, "High speed motors: A comparison between synchronous pm and reluctance machines," in *2017 IEEE Energy Conversion Congress and Exposition (ECCE)*, pp. 3927–3934, 2017.

[44] "Low voltage ie5 synchronous reluctance motors." `https://library.e.abb.com/public/5c6f165165214e9197fde91d98108d0b/IE5%20SynRM%20motors_9AKK107743%20EN%2012-2019.pdf`. Accessed: 2021-10-08.

[45] R. Moghaddam, *Synchronous Reluctance Machine (SynRM) Design*. PhD thesis, 01 2007.

[46] G. Pellegrino, T. Jahns, N. Bianchi, W. Soong, and F. Cupertino, *The Rediscovery of Synchronous Reluctance and Ferrite Permanent Magnet Motors Tutorial Course Notes*. New York: Springer, 2016.

[47] S. Baka, S. Sashidhar, and B. G. Fernandes, "Effect of flux barrier shape on the performance of a two-pole line-start synchronous reluctance motor," in *2018 IEEE International Conference on Power Electronics, Drives and Energy Systems (PEDES)*, pp. 1–6, 2018.

[48] S. Neusüs and A. Binder, "Shaping and dimensioning of the flux barriers in synchronous reluctance machines," in *2017 International Conference on Optimization of Electrical and Electronic Equipment (OPTIM) 2017 Intl Aegean Conference on Electrical Machines and Power Electronics (ACEMP)*, pp. 509–516, 2017.

[49] M. Pohl and D. Gerling, "Analytical model of synchronous reluctance machines with zhukovski barriers," in *2018 XIII International Conference on Electrical Machines (ICEM)*, pp. 91–96, 2018.

[50] A. Dziechciarz and C. Martis, "New shape of rotor flux barriers in synchronous reluctance machines based on zhukovski curves," in *2015 9th International Symposium on Advanced Topics in Electrical Engineering (ATEE)*, pp. 221–224, 2015.

[51] S. Yammine, C. Henaux, M. Fadel, S. Desharnais, and L. Calégari, "Synchronous reluctance machine flux barrier design based on the flux line patterns in a solid rotor," in *2014 International Conference on Electrical Machines (ICEM)*, pp. 297–302, 2014.

[52] I. Husain, B. Ozpineci, M. S. Islam, E. Gurpinar, G.-J. Su, W. Yu, S. Chowdhury, L. Xue, D. Rahman, and R. Sahu, "Electric drive technology trends, challenges, and opportunities for future electric vehicles," *Proceedings of the IEEE*, vol. 109, no. 6, pp. 1039–1059, 2021.

[53] A. Krings and C. Monissen, "Review and trends in electric traction motors for battery electric and hybrid vehicles," in *2020 International Conference on Electrical Machines (ICEM)*, vol. 1, pp. 1807–1813, 2020.

[54] "Electrical steel sheets." `https://www.jfe-steel.co.jp/en/products/electrical/catalog/f1e-001.pdf`. Accessed: 2021-09-06.

[55] J. Pyrhonen, T. Jokinen, and V. Hrabovcova, *Design of Rotating Electrical Machines*. Wiley, 2008.

[56] I. Husain, B. Ozpineci, M. S. Islam, E. Gurpinar, G.-J. Su, W. Yu, S. Chowdhury, L. Xue, D. Rahman, and R. Sahu, "Electric drive technology trends, challenges, and opportunities for future electric vehicles," *Proceedings of the IEEE*, vol. 109, no. 6, pp. 1039–1059, 2021.

[57] C. Babetto, N. Bianchi, and G. Benedetti, "Design and optimization of a pmasr motor for low-voltage e-scooter applications," in *2019 IEEE International Electric Machines Drives Conference (IEMDC)*, pp. 1016–1023, 2019.

[58] H. Yetiş, E. Meşe, and M. Biyikli, "Design and comparison of ferrite based ipm and ndfeb based spm synchronous motors for gearless elevator systems," in *2018 XIII International Conference on Electrical Machines (ICEM)*, pp. 635–641, 2018.

[59] M. Gamba, G. Pellegrino, E. Armando, and S. Ferrari, "Synchronous reluctance motor with concentrated windings for ie4 efficiency," in *2017 IEEE Energy Conversion Congress and Exposition (ECCE)*, pp. 3905–3912, 2017.

[60] A. T. de Almeida, F. J. T. E. Ferreira, and J. A. C. Fong, "Standards for superpremium efficiency class for electric motors," in *Conference Record 2009 IEEE Industrial Commercial Power Systems Technical Conference*, pp. 1–8, 2009.

APPENDIX A

SUPPLEMENTARY DOCUMENTS

AEMOT ELECTRIC MOTORS

ÜÇ FAZLI MOTORLAR İÇİN TİP DENEYLERİ SONUÇ FORMU

1.DENEY MOTORUNUN TANIMI			132M4Q_10kW_1500rpm_senkron_7.5kW_deneme					TARİH/NO	21.12.2020/648			
Güç [kW]	Tip	Paket Boyu	Verim Sınıfı	Sac Kodu	Sarım Sayısı	Tel Çapı	Bobin Bağlantısı	Hava Aralığı [mm]	Rotor Açısı [°]	Anma Gerilimi [V]	Y/Δ	f [Hz]
7.5	132/4									400	Δ	50

2. DENEYE BAŞLAMADAN ÖNCE (motor soğukken) ÖLÇÜLEN DİRENÇLER

U1-V1 [Ω]	0.522	V1-W1 [Ω]	0.522	U1-W1 [Ω]	0.524	t_1 [°C]	16.5

3. TAM YÜK TEST SONUCU (motor nominal gücüne yüklenir.)

Gerilim [V]	I_1 [A]	I_2 [A]	I_3 [A]	I_{ort} [A]	Moment [Nm]	Devir Sayısı [rpm]	P_2 [W]	P_1 [W]	Cosφ	Verim [%]
385	18	17.8	17.9	17.86	48.30	1500	7587	8022	0.67	94.6

4. KİLİTLİ ROTOR TESTİ SONUÇLARI

Moment [Nm]		Akım [A]		Gerilim [V]	Giriş Gücü [W]
#DIV/0!		#DIV/0!		400	0
Ma/Mn	#DIV/0!	Ia/In	####		

5. DEVRİLME MOMENTİ TESTİ SONUÇLARI

Devir Sayısı [rpm]	Moment [Nm]		Akım [A]	Gerilim [V]	Giriş Gücü [W]
0	#DIV/0!		#DIV/0!	400	0
	Mk/Mn	#DIV/0!			

6. ISI TESTİ (Motor 3 saat boyunca tam yük mil gücünde ısınmaya bırakılır.)

7. ISI SONU MOTOR TAM YÜK DEĞERLERİ (motor nominal gücüne yüklenir.)

Gerilim [V]	I_1 [A]	I_2 [A]	I_3 [A]	I_{ort} [A]	Moment [Nm]	Devir Sayısı [rpm]	P_2 [W]	P_1 [W]	Cosφ	Verim [%]
401	17.74	17.72	17.9	17.79	47.90	1500	7524	8004	0.65	94.0

8. ISI SONUCU ÖLÇÜLEN DİRENÇLER (Isınma testi bitince enerji kesilerek hemen ölçme yapılır.)

U1-V1 [Ω]	0.648	V1-W1 [Ω]	0.648	U1-W1 [Ω]	0.648	t_2 [°C]	26.6

9. ISI SONU MOTOR TAM YÜK DEĞİŞİK GERİLİMLER

Gerilim [V]	I_1 [A]	I_2 [A]	I_3 [A]	I_{ort} [A]	Yük Oranı	P_2 [W]	P_1 [W]	Devir Sayısı [rpm]	Moment [Nm]	Cos φ	Verim [%]
428	18.68	18.63	18.87	18.73	100%	7571	8111	1500	48.20	0.58	93.3
420	18.31	18.24	18.42	18.32	100%	7556	8055	1500	48.10	0.60	93.8
380	17.93	17.87	18.00	17.93	100%	7571	8047	1500	48.20	0.68	94.1
361	18.25	18.20	18.35	18.27	100%	7556	8009	1500	48.10	0.70	94.3

10. ISI SONU MOTOR DEĞİŞİK YÜK DEĞERLERİ :

401	21.26	21.18	21.37	21.27	125%	9456	10082	1500	60.20	0.68	93.8
401	19.75	19.65	19.87	19.76	115%	8655	9212	1500	55.10	0.67	94.0
402	17.82	17.72	17.87	17.80	100%	7540	8011	1500	48.00	0.65	94.1
398	14.77	14.75	14.89	14.80	75%	5686	6039	1500	36.20	0.59	94.2
394	12.29	12.24	12.38	12.30	50%	3801	4075	1500	24.20	0.49	93.3
396	11.14	11.07	11.22	11.14	25%	1948	2189	1500	12.40	0.29	89.0

11. DİRENÇ ÖLÇÜMÜ (Değişik yükler testi bitince enerji kesilerek hemen ölçme yapılır.)

U1-V1 [Ω]	0.648	V1-W1 [Ω]	0.648	U1-W1 [Ω]	0.648	t_2 [°C]	26.6

12. BOŞ ÇALIŞMA TESTİ SONUÇLARI (Motor dinamofrenden ayrılır ve fanı üzerinde iken yapılır.)

Gerilim [V]	I_1 [A]	I_2 [A]	I_3 [A]	I_{ort} [A]	P_0 (W)	Devir Sayısı [rpm]	Cosφ
454	16.82	16.69	16.89	16.80	585		0.044
440	14.54	16.67	16.88	16.03	613		0.050
420	16.84	16.66	16.91	16.80	588		0.048
400	16.85	16.65	16.88	16.79	611		0.052
390	16.85	16.68	16.86	16.80	584		0.051
379	16.84	16.69	16.86	16.80	605		0.055
360	16.86	16.70	16.90	16.82	588		0.056

14. MOTOR KAYIPLARI VE VERİM

P_{fw} [W]	
P_{fe} [W]	
P_{cu} [W]	
P_r [W]	
P_{LL} [W]	
P_{total} [W]	
Verim [%]	94.12
Δt	#DIV/0!

13. DİRENÇ ÖLÇÜMÜ (Boşta testi bitince enerji kesilerek hemen ölçme yapılır.)

U1-V1 [Ω]		V1-W1 [Ω]		U1-W1 [Ω]		t_4 [°C]	

15. MOTOR FANI SÖKÜLEREK YAPILAN BOŞ ÇALIŞMA TESTİ SONUÇLARI :

Gerilim [V]	I_1 [A]	I_2 [A]	I_3 [A]	I_{ort} [A]	P_0 (W)	Devir Sayısı [rpm]	Cosφ
				0.00			#DIV/0!
				0.00			#DIV/0!
				0.00			#DIV/0!
				0.00			#DIV/0!
				0.00			#DIV/0!
				0.00			#DIV/0!
				0.00			#DIV/0!
				0.00			#DIV/0!
				0.00			#DIV/0!
				0.00			#DIV/0!

17.NOTLAR

Rotor Çapı Ölçüleri	
Stator Çapı Ölçüleri	
Isı Testi Başlangıç :	
Bitiş :	
Kullanılan Fan :	
Bakır Ağırlığı :	

18. SONUÇ

16. SÜRÜCÜ YARDIMI İLE GÜVENLİ ÇALIŞMA VE AŞIRI HIZ TESTİ YAPILIR:

DENEYİ YAPAN	R.Ferhat TÜLEK	DEĞERLENDİRME VE KONTROL	ONAYLAYAN

AEM Elektrik Motorları San.veTic A.Ş. Taşçınar Kasubası Yıldızeffen Mah. Sanayi Sokak No: 61/1 - 38201 MERKEZ / AKSARAY/TÜRKİYE Tic.Sic.No: 8937 - Mersis No: 0008084798800013

Figure A.1: Datasheet for 7.5 kW test

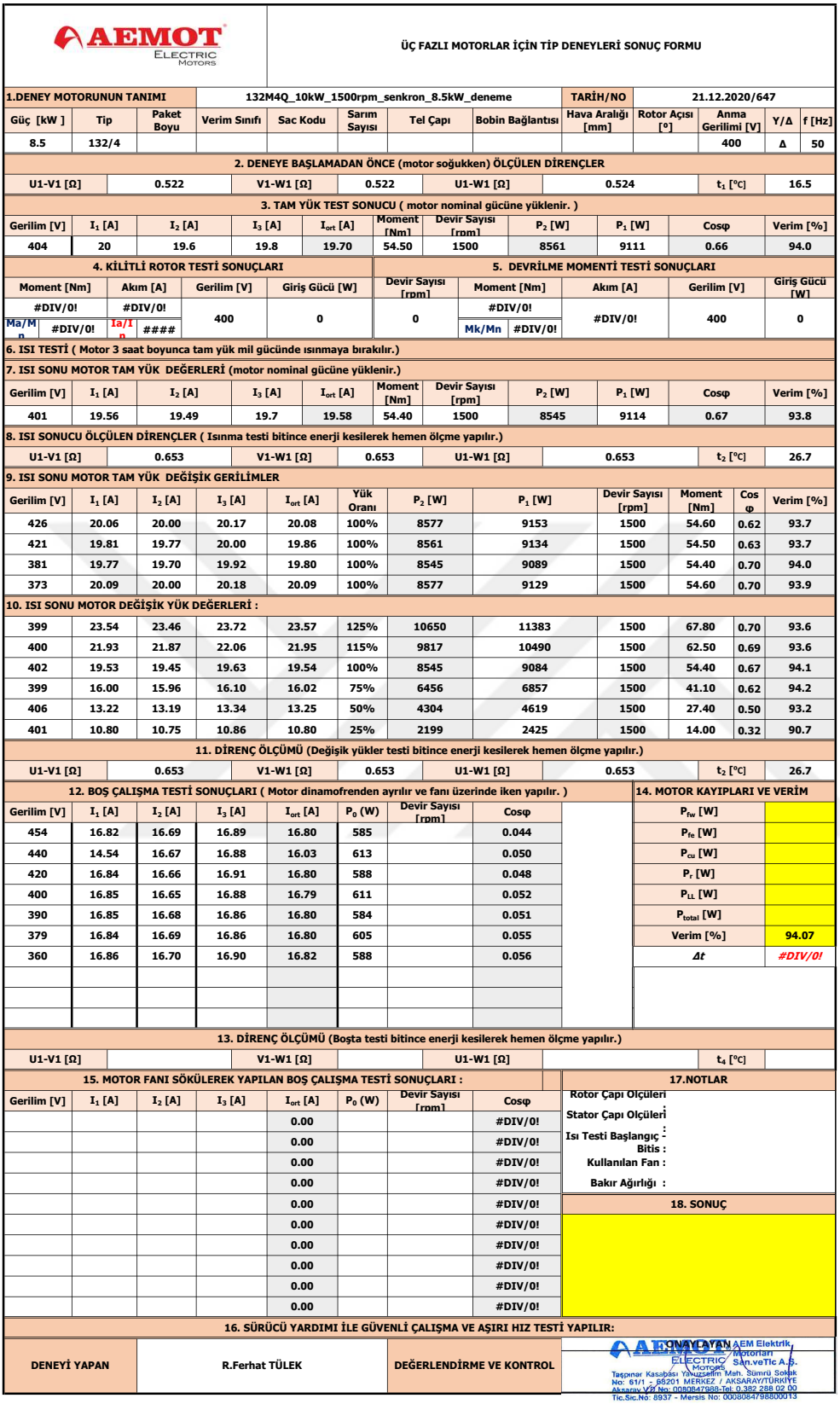

AEMOT ELECTRIC MOTORS

ÜÇ FAZLI MOTORLAR İÇİN TİP DENEYLERİ SONUÇ FORMU

1.DENEY MOTORUNUN TANIMI	132M4Q_10kW_1500rpm_senkron_8.5kW_deneme	TARİH/NO	21.12.2020/647

Güç [kW]	Tip	Paket Boyu	Verim Sınıfı	Sac Kodu	Sarım Sayısı	Tel Çapı	Bobin Bağlantısı	Hava Aralığı [mm]	Rotor Açısı [°]	Anma Gerilimi [V]	Y/Δ	f [Hz]
8.5	132/4									400	Δ	50

2. DENEYE BAŞLAMADAN ÖNCE (motor soğukken) ÖLÇÜLEN DİRENÇLER

U1-V1 [Ω]	0.522	V1-W1 [Ω]	0.522	U1-W1 [Ω]	0.524	t_1 [°C]	16.5

3. TAM YÜK TEST SONUCU (motor nominal gücüne yüklenir.)

Gerilim [V]	I_1 [A]	I_2 [A]	I_3 [A]	I_{ort} [A]	Moment [Nm]	Devir Sayısı [rpm]	P_2 [W]	P_1 [W]	Cosφ	Verim [%]
404	20	19.6	19.8	19.70	54.50	1500	8561	9111	0.66	94.0

4. KİLİTLİ ROTOR TESTİ SONUÇLARI

Moment [Nm]		Akım [A]		Gerilim [V]	Giriş Gücü [W]
#DIV/0!		#DIV/0!		400	0
Ma/Mn	#DIV/0!	Ia/In	####		

5. DEVRİLME MOMENTİ TESTİ SONUÇLARI

Devir Sayısı [rpm]	Moment [Nm]		Akım [A]	Gerilim [V]	Giriş Gücü [W]
0	#DIV/0!		#DIV/0!	400	0
	Mk/Mn	#DIV/0!			

6. ISI TESTİ (Motor 3 saat boyunca tam yük mil gücünde ısınmaya bırakılır.)

7. ISI SONU MOTOR TAM YÜK DEĞERLERİ (motor nominal gücüne yüklenir.)

Gerilim [V]	I_1 [A]	I_2 [A]	I_3 [A]	I_{ort} [A]	Moment [Nm]	Devir Sayısı [rpm]	P_2 [W]	P_1 [W]	Cosφ	Verim [%]
401	19.56	19.49	19.7	19.58	54.40	1500	8545	9114	0.67	93.8

8. ISI SONUCU ÖLÇÜLEN DİRENÇLER (Isınma testi bitince enerji kesilerek hemen ölçme yapılır.)

U1-V1 [Ω]	0.653	V1-W1 [Ω]	0.653	U1-W1 [Ω]	0.653	t_2 [°C]	26.7

9. ISI SONU MOTOR TAM YÜK DEĞİŞİK GERİLİMLER

Gerilim [V]	I_1 [A]	I_2 [A]	I_3 [A]	I_{ort} [A]	Yük Oranı	P_2 [W]	P_1 [W]	Devir Sayısı [rpm]	Moment [Nm]	Cos φ	Verim [%]
426	20.06	20.00	20.17	20.08	100%	8577	9153	1500	54.60	0.62	93.7
421	19.81	19.77	20.00	19.86	100%	8561	9134	1500	54.50	0.63	93.7
381	19.77	19.70	19.92	19.80	100%	8545	9089	1500	54.40	0.70	94.0
373	20.09	20.00	20.18	20.09	100%	8577	9129	1500	54.60	0.70	93.9

10. ISI SONU MOTOR DEĞİŞİK YÜK DEĞERLERİ :

399	23.54	23.46	23.72	23.57	125%	10650	11383	1500	67.80	0.70	93.6
400	21.93	21.87	22.06	21.95	115%	9817	10490	1500	62.50	0.69	93.6
402	19.53	19.45	19.63	19.54	100%	8545	9084	1500	54.40	0.67	94.1
399	16.00	15.96	16.10	16.02	75%	6456	6857	1500	41.10	0.62	94.2
406	13.22	13.19	13.34	13.25	50%	4304	4619	1500	27.40	0.50	93.2
401	10.80	10.75	10.86	10.80	25%	2199	2425	1500	14.00	0.32	90.7

11. DİRENÇ ÖLÇÜMÜ (Değişik yükler testi bitince enerji kesilerek hemen ölçme yapılır.)

U1-V1 [Ω]	0.653	V1-W1 [Ω]	0.653	U1-W1 [Ω]	0.653	t_2 [°C]	26.7

12. BOŞ ÇALIŞMA TESTİ SONUÇLARI (Motor dinamofrenden ayrılır ve fanı üzerinde iken yapılır.)

Gerilim [V]	I_1 [A]	I_2 [A]	I_3 [A]	I_{ort} [A]	P_0 (W)	Devir Sayısı [rpm]	Cosφ
454	16.82	16.69	16.89	16.80	585		0.044
440	14.54	16.67	16.88	16.03	613		0.050
420	16.84	16.66	16.91	16.80	588		0.048
400	16.85	16.65	16.88	16.79	611		0.052
390	16.85	16.68	16.86	16.80	584		0.051
379	16.84	16.69	16.86	16.80	605		0.055
360	16.86	16.70	16.90	16.82	588		0.056

14. MOTOR KAYIPLARI VE VERİM

P_{fw} [W]	
P_{fe} [W]	
P_{cu} [W]	
P_r [W]	
P_{LL} [W]	
P_{total} [W]	
Verim [%]	94.07
Δt	*#DIV/0!*

13. DİRENÇ ÖLÇÜMÜ (Boşta testi bitince enerji kesilerek hemen ölçme yapılır.)

U1-V1 [Ω]		V1-W1 [Ω]		U1-W1 [Ω]		t_4 [°C]	

15. MOTOR FANI SÖKÜLEREK YAPILAN BOŞ ÇALIŞMA TESTİ SONUÇLARI :

Gerilim [V]	I_1 [A]	I_2 [A]	I_3 [A]	I_{ort} [A]	P_0 (W)	Devir Sayısı [rpm]	Cosφ
				0.00			#DIV/0!
				0.00			#DIV/0!
				0.00			#DIV/0!
				0.00			#DIV/0!
				0.00			#DIV/0!
				0.00			#DIV/0!
				0.00			#DIV/0!
				0.00			#DIV/0!
				0.00			#DIV/0!
				0.00			#DIV/0!

17.NOTLAR

Rotor Çapı Ölçüleri :
Stator Çapı Ölçüleri :
Isı Testi Başlangıç :
Bitis :
Kullanılan Fan :
Bakır Ağırlığı :

18. SONUÇ

16. SÜRÜCÜ YARDIMI İLE GÜVENLİ ÇALIŞMA VE AŞIRI HIZ TESTİ YAPILIR:

DENEYİ YAPAN	R.Ferhat TÜLEK	DEĞERLENDİRME VE KONTROL	ONAYLAYAN

AEMOT Elektrik Motorları San.veTic A.Ş.
Taşpınar Kasabası Yenuzelim Mah. Sümrü Sokak No: 61/1 - 68201 MERKEZ / AKSARAY/TÜRKİYE
Aksaray VD No: 0080847888-Tel: 0 382 288 02 00
Tic.Sic.No: 8937 - Mersis No: 0008084798800013

Figure A.2: Datasheet for 8.5 kW test

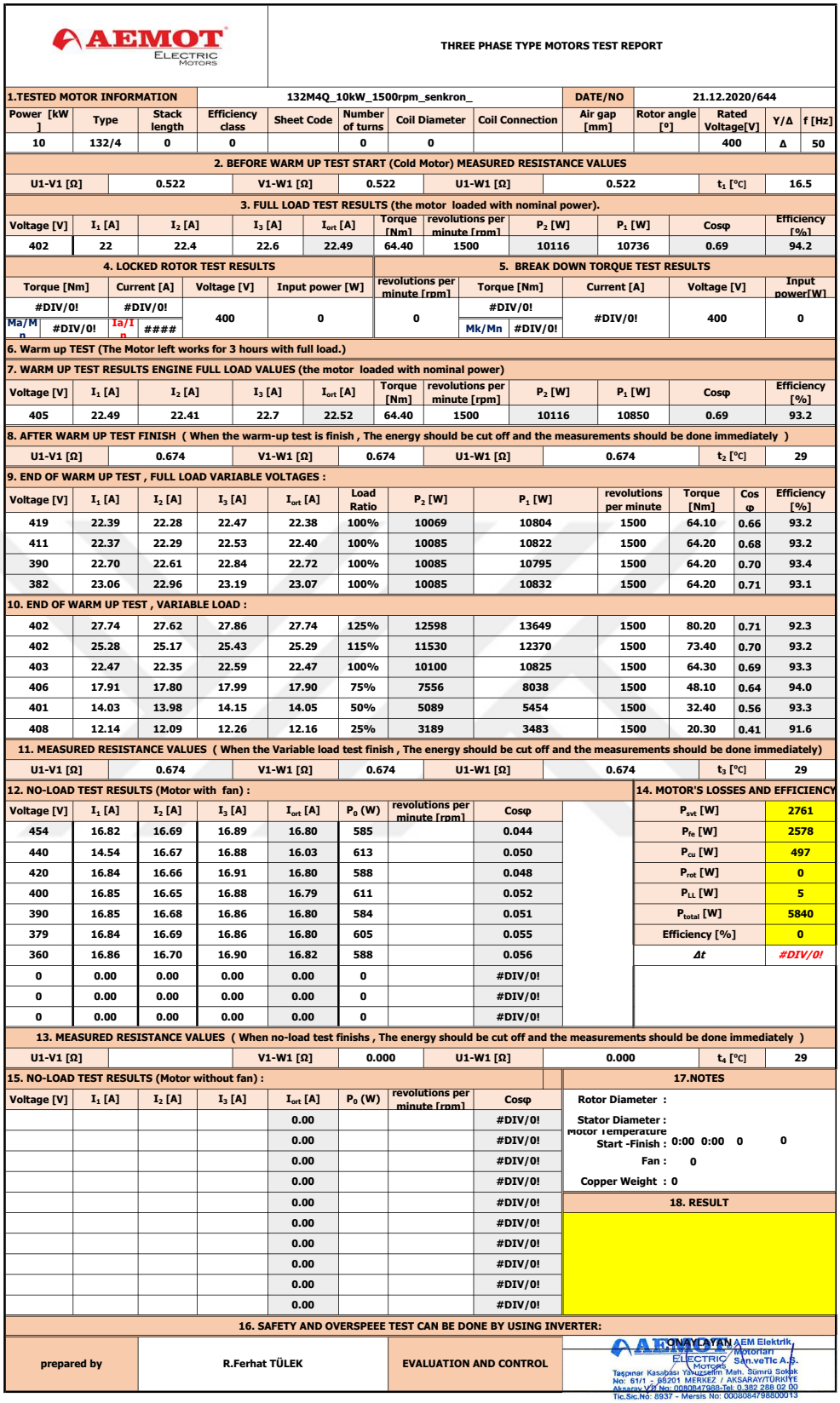

AEMOT ELECTRIC MOTORS

THREE PHASE TYPE MOTORS TEST REPORT

1.TESTED MOTOR INFORMATION			132M4Q_10kW_1500rpm_senkron_				DATE/NO		21.12.2020/644		
Power [kW]	Type	Stack length	Efficiency class	Sheet Code	Number of turns	Coil Diameter	Coil Connection	Air gap [mm]	Rotor angle [°]	Rated Voltage[V]	Y/Δ	f [Hz]
10	132/4	0	0		0	0				400	Δ	50

2. BEFORE WARM UP TEST START (Cold Motor) MEASURED RESISTANCE VALUES									
U1-V1 [Ω]	0.522	V1-W1 [Ω]	0.522	U1-W1 [Ω]	0.522	t_1 [°C]	16.5		

3. FULL LOAD TEST RESULTS (the motor loaded with nominal power).										
Voltage [V]	I_1 [A]	I_2 [A]	I_3 [A]	I_{ort} [A]	Torque [Nm]	revolutions per minute [rpm]	P_2 [W]	P_1 [W]	Cosφ	Efficiency [%]
402	22	22.4	22.6	22.49	64.40	1500	10116	10736	0.69	94.2

4. LOCKED ROTOR TEST RESULTS						5. BREAK DOWN TORQUE TEST RESULTS				
Torque [Nm]		Current [A]		Voltage [V]	Input power [W]	revolutions per minute [rpm]	Torque [Nm]		Current [A]	Voltage [V]	Input power[W]
#DIV/0!		#DIV/0!		400	0	0	#DIV/0!		#DIV/0!	400	0
Ma/Mn	#DIV/0!	Ia/In	####				Mk/Mn	#DIV/0!			

6. Warm up TEST (The Motor left works for 3 hours with full load.)

7. WARM UP TEST RESULTS ENGINE FULL LOAD VALUES (the motor loaded with nominal power)									
Voltage [V]	I_1 [A]	I_2 [A]	I_3 [A]	I_{ort} [A]	Torque [Nm]	revolutions per minute [rpm]	P_2 [W]	P_1 [W]	Cosφ	Efficiency [%]
405	22.49	22.41	22.7	22.52	64.40	1500	10116	10850	0.69	93.2

8. AFTER WARM UP TEST FINISH (When the warm-up test is finish , The energy should be cut off and the measurements should be done immediately)							
U1-V1 [Ω]	0.674	V1-W1 [Ω]	0.674	U1-W1 [Ω]	0.674	t_2 [°C]	29

9. END OF WARM UP TEST , FULL LOAD VARIABLE VOLTAGES :										
Voltage [V]	I_1 [A]	I_2 [A]	I_3 [A]	I_{ort} [A]	Load Ratio	P_2 [W]	P_1 [W]	revolutions per minute	Torque [Nm]	Cos φ	Efficiency [%]
419	22.39	22.28	22.47	22.38	100%	10069	10804	1500	64.10	0.66	93.2
411	22.37	22.29	22.53	22.40	100%	10085	10822	1500	64.20	0.68	93.2
390	22.70	22.61	22.84	22.72	100%	10085	10795	1500	64.20	0.70	93.4
382	23.06	22.96	23.19	23.07	100%	10085	10832	1500	64.20	0.71	93.1
10. END OF WARM UP TEST , VARIABLE LOAD :										
402	27.74	27.62	27.86	27.74	125%	12598	13649	1500	80.20	0.71	92.3
402	25.28	25.17	25.43	25.29	115%	11530	12370	1500	73.40	0.70	93.2
403	22.47	22.35	22.59	22.47	100%	10100	10825	1500	64.30	0.69	93.3
406	17.91	17.80	17.99	17.90	75%	7556	8038	1500	48.10	0.64	94.0
401	14.03	13.98	14.15	14.05	50%	5089	5454	1500	32.40	0.56	93.3
408	12.14	12.09	12.26	12.16	25%	3189	3483	1500	20.30	0.41	91.6

11. MEASURED RESISTANCE VALUES (When the Variable load test finish , The energy should be cut off and the measurements should be done immediately)							
U1-V1 [Ω]	0.674	V1-W1 [Ω]	0.674	U1-W1 [Ω]	0.674	t_3 [°C]	29

12. NO-LOAD TEST RESULTS (Motor with fan) :							
Voltage [V]	I_1 [A]	I_2 [A]	I_3 [A]	I_{ort} [A]	P_0 (W)	revolutions per minute [rpm]	Cosφ
454	16.82	16.69	16.89	16.80	585		0.044
440	14.54	16.67	16.88	16.03	613		0.050
420	16.84	16.66	16.91	16.80	588		0.048
400	16.85	16.65	16.88	16.79	611		0.052
390	16.85	16.68	16.86	16.80	584		0.051
379	16.84	16.69	16.86	16.80	605		0.055
360	16.86	16.70	16.90	16.82	588		0.056
0	0.00	0.00	0.00	0.00	0		#DIV/0!
0	0.00	0.00	0.00	0.00	0		#DIV/0!
0	0.00	0.00	0.00	0.00	0		#DIV/0!

14. MOTOR'S LOSSES AND EFFICIENCY	
P_{svt} [W]	2761
P_{fe} [W]	2578
P_{cu} [W]	497
P_{rot} [W]	0
P_{LL} [W]	5
P_{total} [W]	5840
Efficiency [%]	0
Δt	#DIV/0!

13. MEASURED RESISTANCE VALUES (When no-load test finishs , The energy should be cut off and the measurements should be done immediately)							
U1-V1 [Ω]		V1-W1 [Ω]	0.000	U1-W1 [Ω]	0.000	t_4 [°C]	29

15. NO-LOAD TEST RESULTS (Motor without fan) :							
Voltage [V]	I_1 [A]	I_2 [A]	I_3 [A]	I_{ort} [A]	P_0 (W)	revolutions per minute [rpm]	Cosφ
				0.00			#DIV/0!
				0.00			#DIV/0!
				0.00			#DIV/0!
				0.00			#DIV/0!
				0.00			#DIV/0!
				0.00			#DIV/0!
				0.00			#DIV/0!
				0.00			#DIV/0!
				0.00			#DIV/0!
				0.00			#DIV/0!

17.NOTES
Rotor Diameter :
Stator Diameter :
Motor Temperature Start -Finish : 0:00 0:00 0 0
Fan : 0
Copper Weight : 0

18. RESULT

16. SAFETY AND OVERSPEEE TEST CAN BE DONE BY USING INVERTER:			
prepared by	R.Ferhat TÜLEK	EVALUATION AND CONTROL	CONFORMITY

AEMOT Elektrik Motorları San.veTic A.Ş.
Taşpınar Kasabası Yavuzselim Mah. Sümrü Sokak No: 51/1 - 68201 MERKEZ / AKSARAY/TÜRKİYE
Aksaray VD.No: 0080847988-Tel: 0.382 288 02 00
Tic.Sic.No: 8937 - Mersis No: 0008084798800013

Figure A.3: Datasheet for 10 kW test